
Electronic Thesis and Dissertation Repository

6-23-2016 12:00 AM

The Effect Of Mesh-Type Bubble Breakers On Two-Phase Vertical Co-Flow

Alan Kalbfleisch
The University of Western Ontario

Supervisor
Kamran Siddiqui
The University of Western Ontario

Graduate Program in Mechanical and Materials Engineering
A thesis submitted in partial fulfillment of the requirements for the degree in Master of
Engineering Science
© Alan Kalbfleisch 2016

Follow this and additional works at: <https://ir.lib.uwo.ca/etd>



Part of the [Energy Systems Commons](#), [Heat Transfer, Combustion Commons](#), and the [Other Mechanical Engineering Commons](#)

Recommended Citation

Kalbfleisch, Alan, "The Effect Of Mesh-Type Bubble Breakers On Two-Phase Vertical Co-Flow" (2016).
Electronic Thesis and Dissertation Repository. 3946.
<https://ir.lib.uwo.ca/etd/3946>

This Dissertation/Thesis is brought to you for free and open access by Scholarship@Western. It has been accepted for inclusion in Electronic Thesis and Dissertation Repository by an authorized administrator of Scholarship@Western. For more information, please contact wlsadmin@uwo.ca.

Abstract

It is proposed that mesh-type bubble breakers can be used in two-phase gas-liquid vertical cocurrent pipe flow to enhance the heat and mass transfer rates. Two experimental studies were performed to investigate the effect of mesh-type bubble breakers with varying geometries on two-phase flow behaviour. The first used highspeed imaging to measure bubble size and observe the resulting flow regime for two-phase vertical co-flow consisting of air and water. A Froude number correlation that can be used to predict the bubble size generated by mesh-type bubble breakers is proposed. Flow regime maps for two-phase flow in the presence of bubble breakers with varying geometry were produced. The second study investigated two-phase flow heat transfer. A correlation to predict the two-phase Nusselt number (limited to superficial liquid and gas Reynolds number of $Re_{SL} < 2000$ and $Re_{SG} < 100$ respectively) was proposed. A thorough investigation of the effect of mesh-type bubble breakers on two-phase heat transfer is discussed.

Keywords

Two-Phase Flow, Cocurrent, Experimental Fluids, Bubble Breakup, Flow Regime, Convective Heat Transfer

Acknowledgments

I would like to acknowledge Dr. Kamran Siddiqui for his continued support and guidance throughout the completion of my degree.

Table of Contents

Abstract.....	i
Acknowledgments.....	ii
Table of Contents.....	iii
List of Tables.....	vi
Chapter 3.....	vi
List of Figures.....	vii
Chapter 1.....	vii
Chapter 2.....	viii
Chapter 3.....	x
Chapter 1.....	1
1 Introduction.....	1
1.1 Global Demand for Air Conditioning.....	1
1.2 Vapor Compression Refrigeration.....	3
1.3 Heat Absorption Refrigeration.....	5
1.4 Challenges with the small-scale implementation of heat absorption cycle.....	8
1.5 Absorber Improvements.....	9
1.6 Bubble Formation Process.....	10
1.7 Two-Phase Flow Regimes.....	17
1.8 Motivation.....	20
1.9 Objectives.....	21
1.10 Research Impact.....	21
1.11 Thesis Outline.....	21
1.12 Co-Authorship Statement.....	22
1.13 References.....	23

Chapter 2.....	26
2 Bubble Size Prediction and Flow Regime Analysis for Two-Phase Vertical Co-flow in the Presence of a Mesh-Type Bubble Breaker.....	26
2.1 Introduction.....	26
2.2 Nomenclature.....	31
2.3 Experimental Setup and Procedure.....	32
2.4 Results and Discussion.....	40
2.4.1 Bubbly Flow Analysis.....	40
2.4.2 Flow Regime Characterization.....	53
2.5 Conclusion.....	69
2.6 References.....	70
Chapter 3.....	75
3 Two-Phase Vertical Co-Flow Heat Transfer in the Presence of a Mesh-Type Bubble Breaker.....	75
3.1 Introduction.....	75
3.2 Nomenclature.....	79
3.3 Experimental Setup and Procedure.....	81
3.4 Results and Analysis.....	91
3.4.1 Two-Phase Convective Heat Transfer Coefficient (no bubble breaker)...	91
3.4.2 Influence of the Bubble Breaker on Heat Transfer.....	97
3.5 Conclusion.....	113
3.6 References.....	113
Chapter 4.....	118
4 Conclusion.....	118
4.1 Overview.....	118
4.2 Contribution.....	121
4.3 Future Recommendations.....	122

Curriculum Vitae 124

List of Tables

Chapter 3

Table 3.1: Two-Phase Flow Regime Characterization with no Bubble Breaker Present 94

Table 3.2: Two-Phase Flow Regime Characterization with Bubble Breakers of Varying Pore
Sizes 102

List of Figures

Chapter 1

Figure 1.1: Schematic of a vapor-compression refrigeration cycle.	5
Figure 1.2: Schematic of a heat absorption refrigeration cycle.	7
Figure 1.3: A schematic of an air-cooled vertical tubular absorber depicted in a study by Fernández et al. [25].	11
Figure 1.4: Two stages of bubble formation (Expansion and Detachment) as proposed by Ramarkrishin et al. [26].	12
Figure 1.5: Force balance of a bubble in stagnant liquid during the expansion phase. For a low gas flowrate, the Viscous Drag force (F_v) and Gas Intertia Force (F_I) would be negligible.....	13
Figure 1.6: Force balance of a bubble in stagnant liquid during the detachment phase.	14
Figure 1.7: Force balance of a bubble during the expansion phase (left) and the detachment phase (right) in an upward flowing liquid.....	15
Figure 1.8: Bubble shapes during bubble formation from a submerged vertical nozzle in upward flowing liquid as predicted by Terasaka et al. [29].....	16
Figure 1.9: Two-phase vertical flow regimes proposed by Hewitt and Roberts [30].....	18
Figure 1.10: Flow regime map for vertical tubular two-phase cocurrent flow proposed by Hewitt and Roberts [30]. The subscripts l and v represent liquid and gas respectively.	19

Chapter 2

Figure 2.1: Schematic of the experimental setup.....	34
Figure 2.2: Bubble Breaker cross section showing various geometric parameters; bubble breaker thickness (t), diameter (D_{bb}) and pore size (S).....	35
Figure 2.3: Schematic of the positioning of the bubble breaker in the center pipe and other related parameters; the distance between the nozzle tip and bubble breaker (H) and the bubble breaker length (L).....	36
Figure 2.4: Illustration of the major and minor axes detection of an individual bubble in an image segment.	37
Figure 2.5: The identified bubbles approxiated as ellipses are shown plotted over an original image.....	38
Figure 2.6: Qualitative comparison of the two-phase flow without a bubble breaker and in the presence of bubble breakers with different pore sizes (shown underneath the respective images). The bubble breaker was located 25 mm downstream of the nozzle tip. The length of each bubble breaker was $L/D_{bb}=1$. The liquid and gas flow rates in all the images were $Q_L=2.5$ LPM and $Q_G=0.5$ LPM, respectively.	41
Figure 2.7: Mean diameters of bubbles generated by bubble breakers of different pore sizes versus the volumetric gas-liquid flow ratios for gas-liquid vertical co-flow.....	42
Figure 2.8: The size distribution of bubbles generated by a bubble breaker with a pore size of $S=2$ mm for three gas-liquid flow ratios.	45
Figure 2.9: Froude number versus the normalized diameter of nozzle-generated bubble. The Froude number correlation proposed by Sada et al. [19] is plotted as the dashed line.....	47
Figure 2.10: Modified shape factors plotted versus the modified Froude for all cases. The best-fit equation and $\pm 20\%$ confidence limits are also plotted.....	50

Figure 2.11: Modified shape factors plotted versus the modified Froude number for different lengths and positions of the bubble breaker of 2 mm pore size. The correlation from Equation (9) is also plotted for comparison. 52

Figure 2.12: Images of Two-Phase flow with no bubble breaker. From left to right the images show bubbly flow ($Q_L=0.63$ LPM, $Q_G=0.2$ LPM, $GLR=0.32$), slug flow ($Q_L=0.63$ LPM, $Q_G=1.0$ LPM, $GLR=1.59$), and churn flow ($Q_L=0.63$ LPM, $Q_G=2.0$ LPM, $GLR=3.17$). 54

Figure 2.13: Images of Two-Phase flow after passing through a bubble breaker ($S=2$ mm, $H=25$ mm, $L/D_{bb}=1$). From left to right the images show bubbly flow ($Q_L=0.63$ LPM, $Q_G=0.5$ LPM, $GLR=0.79$), slug flow ($Q_L=0.63$ LPM, $Q_G=1.5$ LPM, $GLR=2.38$), and churn flow ($Q_L=0.63$ LPM, $Q_G=2.5$ LPM, $GLR=3.97$). 55

Figure 2.14: Flow transition chart for cases without a bubble breaker over a range of air and water flow rates. The coloured symbols depict each flow regime (blue=bubble, green=slug, red=churn)..... 56

Figure 2.15: Flow transition charts for the cases with bubble breakers of different pore sizes (1-4 mm). The length of the bubble breaker and the height above the nozzle tip remain constant at $L/D_{bb}=1$ and $H=25$ mm, respectively..... 58

Figure 2.16: Image sequence showing the slug formation downstream of a bubble breaker with a pore size of $S=1$ mm at a liquid flowrate of $Q_L=3.2$ LPM and a gas flowrate of $Q_G=1.5$ LPM ($GLR=0.47$). The time interval between images is 0.005 seconds. The gas slug regions are highlighted by red outlines. 59

Figure 2.17: An image sequence, illustrating the formation of a tip at the leading edge of a nozzle-generated bubble at liquid and gas flowrates of $Q_L=3.2$ LPM and $Q_G=1.5$ LPM ($GLR=0.47$). The time separation between images is 0.003 seconds..... 61

Figure 2.18: An image showing the flow of a gas region through a bubble breaker that is unable to split the bubble into multiple pores due to the bubble tip formed after detaching from the nozzle. 62

Figure 2.19: Flow transition charts for the cases with bubble breakers at two different positions above the nozzle tip for two different pore sizes..... 64

Figure 2.20: Flow transition charts for bubble breakers with two different lengths..... 66

Figure 2.21: Slug formation of a gas region passing through a bubble breaker with a length of $L/D_{bb}=0.5$. Images are separated by 0.006 seconds. 67

Chapter 3

Figure 3.1: The schematic of the apparatus used to measure the two-phase heat transfer rate. Separate computers were used to record the data from the in-flow thermocouples and the thermal camera. A PID Temperature controller was used to keep the water reservoir at a constant temperature of $T_b=80^\circ\text{C}$. Three fans (not shown in the schematic) were placed in a vertical series beside the stainless steel pipe to provide forced convection cooling. 82

Figure 3.2: Bubble Breaker cross section showing various geometric parameters; bubble breaker thickness (t), diameter (D_{bb}) and pore size (S). 83

Figure 3.3: A schematic showing the placement of three small fans to induce a uniform horizontal airflow across the vertical stainless steel pipe causing forced convection heat transfer to occur between the pipe surface and the surrounding air.. 96

Figure 3.4: A temperature plot of a two-phase flow with a superficial liquid Reynolds number of $Re_{SL}=1150$ and a superficial gas Reynolds number of $Re_{SG}=40$ 87

Figure 3.5: Local convective heat transfer coefficients along the pipe length for a two-phase flow ($Re_{SL}=1150$ and $Re_{SG}=40$). The error bars represent propagated measurement error from the thermocouples and flowmeters. 89

Figure 3.6: The measured Nusselt number for a single phase flow at different Reynolds number compared to the classical Nusselt number for laminar pipe flow with constant surface heat flux, $Nu_L=4.36$ [33]. The error bars represent the root mean square of the propagated errors 90

Figure 3.7: Convective heat transfer coefficients for two-phase vertical pipe flow at various superficial gas and liquid Reynolds numbers. The error bars represent the root mean square of the propagated errors from the local heat transfer coefficient values.....	92
Figure 3.8: Two-phase Nusselt number plotted vs. the liquid-to-gas Reynolds number ratio. The best-fit equation is also plotted.	96
Figure 3.9: Convective heat transfer coefficients for two-phase vertical pipe flow with and without bubble breakers at a superficial liquid Reynolds number of $Re_{SL}=380$ and different superficial gas Reynolds numbers.	99
Figure 3.10: Convective heat transfer coefficients for two-phase vertical pipe flow with and without bubble breakers at a superficial liquid Reynolds number of $Re_{SL}=1150$ and different superficial gas Reynolds numbers.	100
Figure 3.11: Convective heat transfer coefficients for two-phase vertical pipe flow with and without bubble breakers at a superficial liquid Reynolds number of $Re_{SL}=1900$ and different superficial gas Reynolds numbers.	101
Figure 3.12: Highspeed camera images of the flow generated by three bubbles breakers at the same flow conditions ($Re_{SG}=40$ and $Re_{SL}=380$).	104
Figure 3.13: High-speed camera images of the flow generated by three bubbles breakers at the same flow conditions ($Re_{SG}=79$ and $Re_{SL}=380$).	106
Figure 3.14: High-speed camera images of the flow generated by three bubbles breakers at the same flow conditions ($Re_{SG}=40$ and $Re_{SL}=1150$).	108
Figure 3.15: High-speed camera images of the flow generated by three bubbles breakers at the same flow conditions ($Re_{SG}=79$ and $Re_{SL}=1150$).	109
Figure 3.16: Local convective heat transfer coefficients along the length of the pipe for all three bubble breakers and in the absence of a bubble breaker for a two-phase flow with superficial liquid and gas Reynolds numbers of $Re_{SL}=1150$ and $Re_{SG}=79$ respectively.	111

Chapter 1

1 Introduction

1.1 Global Demand for Air Conditioning

Global energy demand for residential air conditioning has increased in recent years. In Canada, energy demand for residential space cooling has increased by 68% from 1990 to 2009 [1]. In the United States, the percentage of homes with air conditioning has increased from 68% in 1993 to 87% in 2009 [2]. Throughout the world, developing countries have seen even larger increases in residential air conditioning demand. In urban China, the number of air conditioning units per household increased from 8 units per 100 households in 1995 to 106 units per 100 households in 2009 [3]. India stands out as another country with the potential for a significant increase in air conditioning demand [4]. In spite of the fact that only a small fraction of India's population can afford air conditioner, its potential demand for cooling is twelve times that of the United States [4].

Air conditioning is used to provide thermal comfort in building interiors. If temperatures inside a building are too high for thermal comfort, an air conditioning system is used to remove heat, reduce the interior temperature, and maintain it in the thermal comfort range. Energy demand for air conditioning can fluctuate due to outdoor temperatures and solar radiation intensity. In Ontario, Canada, this leads to peak energy demands in the Summer months that are too great for its base supply from Nuclear and Hydro [5]. During peak times, natural gas power plants must be turned on to overcome the higher energy demand. Using natural gas to produce electricity is more harmful to the environment than the base energy sources, as it produces greenhouse gases. Electricity produced by natural gas is also more expensive than the base energy sources causing Ontario electricity prices to be higher during times of peak demand [6]. Other issues can arise from peak energy demands from air conditioning units such as blackouts. In 2012, a power outage in India caused by overloading of power stations left an area populated by 670 million people without power [7]. Fluctuations in power demand for air conditioning units can overload power stations, leaving millions of people without power.

Studies have been done to predict the effect of global warming, population growth and economic trends on the demand of residential air conditioning. A study by Petri and Calderia [8] analyzed historical data from weather stations and used current models of global warming to predict the change in cooling degree-days (CDD) throughout regions in the United States. Cooling degree-days are defined as the number of degrees that a day's temperature is above 65°F [8]. For example, if the average daily temperature in a region over a period of 30 days is 70°F, the CDD value for that period is 150. The number of cooling degree-days in a region can be used to estimate the amount of energy required for air conditioning. The median yearly CDD value for the contiguous United States is expected to increase to 2215 by 2080 from a value of 792 in 2010 [8]. Although all regions in the United States are expected to see an increase in CDD values, the largest increases will be seen in southern United States with high historical CDD values. For example, the CDD value for California is expected to increase by 1962 and the CDD value for Southern Texas is expected to increase by 2250 [8]. The increase in CDD values in regions that already have high demand for air conditioning will lead to even larger peak energy demands during periods of high outdoor temperatures.

Sivak [9] presented an estimation for global energy demand for air conditioning. In his study, current populations and CDD values for metropolis regions throughout the world were used to predict the potential global air conditioning energy demand. If ownership of air conditioning systems throughout the world is equal to the current level of ownership in the United States, it is estimated that the global energy demand for air conditioning is 50 times higher than that of the United States [9]. Energy for air conditioners already accounts for 5% of the 3800 TWh of electricity produced yearly in the United States [10, 11]. A study by Isaac and van Vurren [12] projects the increase in global demand for air conditioning as a function of income trends, population growth and increase in global temperature due to global warming. At current ownership of air conditioning units, global energy demand for air conditioning by 2100 is expected to increase by 72% from its 2000 level, due to global warming alone [12]. When population growth and economic trends are added, global demand energy demand for air conditioning is estimated to grow to 10000 TWh by 2100 from 300 TWh in 2000 [12]. A large factor in the estimated increase from the Isaac and van Vurren's [12] study is the predicted acceleration of global

warming due the increase in energy use. Since most of the world's electricity is currently produced by sources that generate greenhouse gases, the increase in energy demand for air conditioning will increase the production of greenhouse gases. This in turn will increase global temperatures leading to a further increase in the demand for air conditioning. This cycle causes the predicted global energy demand for air conditioning to increase exponentially [12].

The studies discussed previously have all assumed that the technology for electricity generation, building design and air conditioning remains unchanged. By producing electricity with renewable resources such as solar, wind or hydro that don't produce greenhouse gases, the acceleration of global warming caused by an increase in air conditioning demand could be curtailed. Change in building design and materials used in residential buildings can reduce the energy needed to cool an interior space. The main goal of the change in building design is to reduce the solar radiation entering the space (directly or indirectly) or the internal heat gains. Use of double skin roofs have been shown to reduce heat gain by solar radiation through a building roof by 50% [13]. Heat gain through windows can be substantially reduced by installing double pane windows with optimal spacing and shading [14]. Planting trees in urban areas has also been suggested to provide shade in summer months that prevents solar radiation from entering residential buildings [15]. Recent technological improvements have also made air conditioning systems more energy efficient leading to a decrease in energy needed for cooling. Residential air conditioning systems on the market today can be up to 40% more efficient than systems sold 10 years ago [16].

1.2 Vapor Compression Refrigeration

Air conditioning and refrigeration systems currently used in residential and commercial/institutional sectors operate on vapor-compression refrigeration cycle. A schematic of the vapor-compression refrigeration cycle is shown in Figure 1.1. Various thermodynamics processes involved in the complete refrigeration cycle are described below [17]. A refrigerant, typically R-104A, flows throughout the cycle. Beginning at state (1) in Figure 1.1, a mixed phase liquid-gas refrigerant at a low pressure and low temperature enters the evaporator. The evaporator is located within the space that requires cooling.

The temperature of the refrigerant must be below the temperature of the cooling environment to allow heat transfer from the air in the cooling environment to the refrigerant in the evaporator (Q_E). As the refrigerant flows through the evaporator, the heat being transferred from the interior air causes the refrigerant to undergo a phase change to a vapor form at a constant temperature. The refrigerant leaves the evaporator as a saturated vapor and enters the compressor at state (2). The compressor adds energy to the refrigerant in the form of work (\dot{W}_{Comp}). The pressure and temperature of the refrigerant are increased and the refrigerant leaves the compressor as a superheated vapor at state (3). After the compressor, the superheated vapor refrigerant enters the condenser. The condenser is located outside of the cooling environment allowing heat to be transferred from the refrigerant to the warm environment, typically outside atmosphere (Q_{Con}). The compressor must add enough energy to the refrigerant to increase its temperature to a higher value than the temperature of the atmospheric air to allow heat transfer from the refrigerant to the atmospheric air to occur. The heat transfer from the refrigerant causes its enthalpy to decrease. The refrigerant undergoes a phase change at constant temperature and exits the condenser as saturated liquid at state (4). The refrigerant then enters the expansion valve. The expansion valve causes a reduction in pressure and temperature at constant enthalpy, bringing the refrigerant back to the mixed phase liquid-gas at state (1).

The energy demand for air conditioning in the form of electricity is the energy required to operate the compressor. Compressing a vapor to increase its temperature and pressure is a very energy intensive process. Typically, the efficiency of a residential air conditioning system is measured as the energy efficiency ratio (EER). The EER is the ratio of the cooling output (Q_E , BTU/h) to the electricity input required for the compressor (\dot{W}_{Comp} , W). In Canada, air conditioning units that receive an ENERGY STAR® rating must have an EER of 10.7 [16].

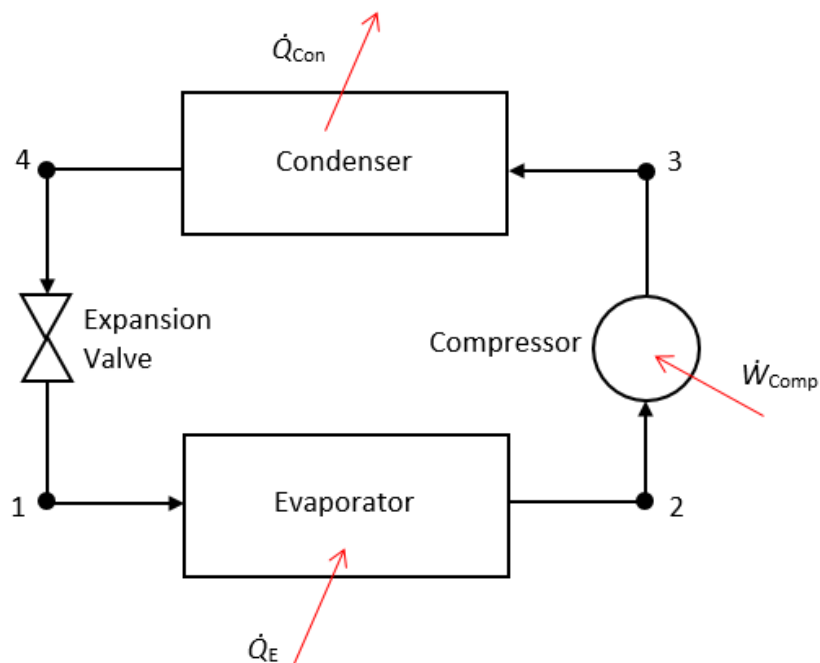


Figure 1.1: Schematic of a vapor-compression refrigeration cycle.

1.3 Heat Absorption Refrigeration

An alternative refrigeration process exists that requires less energy in the form of electricity to operate: the heat absorption refrigeration cycle. A schematic of the heat absorption refrigeration cycle is shown in Figure 1.2. Components such as the evaporator, condenser and expansion valve are common to both the vapor compression refrigeration cycle and the heat absorption refrigeration cycle and operate in the same way. The primary difference between the two cycles is that the heat absorption refrigeration cycle is heat-driven. That is, the heat absorption refrigeration cycle does not have a compressor and instead uses a secondary absorption cycle. Another difference between the two systems is that they both use different types of refrigerants. Various thermodynamics processes involved in the heat absorption refrigeration cycle are described below based on ammonia-water cycle [17].

Starting at state (1) in Figure 1.2, the low temperature and low pressure ammonia enters the evaporator as a mixed phase liquid-gas flow. Similar to the evaporator component in the vapor-compression cycle, heat is removed from the cooling environment space by ammonia which leads to its phase transformation into the vapor form. The ammonia leaves the evaporator as saturated vapor and enters the absorber at state (2). The absorber component is unique to the heat absorption refrigeration cycle. The saturated vapor ammonia is mixed with a high temperature liquid water-ammonia mixture. The saturated vapor ammonia is absorbed into the liquid mixture, increasing the ammonia concentration. During the absorption process, heat must also be transferred from the ammonia-water mixture to the outside atmosphere (Q_A). After the ammonia vapors are fully absorbed, the high concentration mixture enters a pump at state (3). The pump increases the pressure of the mixture by inputting energy in the form of work (\dot{W}_P). After leaving the pump, the high pressure, high concentration ammonia-water mixture enters a heat exchanger at state (4) to recover heat from the low concentration ammonia-water mixture entering the absorber. The high concentration mixture, after recovering the heat, enters the generator at state (5). Heat is added to the mixture (Q_G) causing ammonia to desorb from the liquid mixture in the form of superheated vapor. The remaining low concentration liquid exits the generator at state (6) and enters the heat exchanger allowing heat to be recovered by the high concentration mixture. After the heat exchanger, the low concentration liquid enters an expansion valve at state (7) to reduce its pressure to be equal to the pressure of the ammonia vapor exiting the evaporator at state (2). The low pressure, low concentration ammonia-water mixture is fed back into the absorber at state (8). The pure ammonia superheated vapor that was separated by the heat added to the generator enters the condenser at state (9). Similar to the vapor compression cycle, heat is transferred from the refrigerant in the condenser to the warm environment or outside atmosphere causing the refrigerant (ammonia) to lose enthalpy and undergo phase transformation at a constant temperature. The ammonia exits the condenser as saturated liquid at state (10) and enters an expansion valve to reduce its temperature and pressure at constant enthalpy before entering back into the evaporator as a mixed phase liquid-gas flow at state (1).

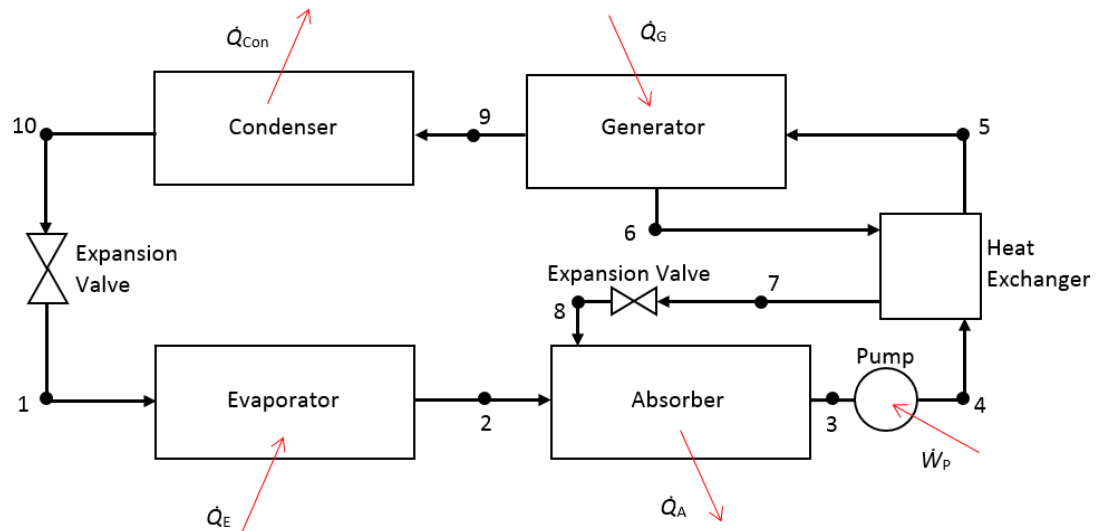


Figure 1.2: Schematic of a heat absorption refrigeration cycle.

The main advantage of a heat absorption refrigeration cycle compared to a vapor-compression cycle is the reduction of electricity needed to operate the system. In the heat absorption refrigeration cycle, the only electrical energy input needed is for operation of the pump. Although both the pump, in the heat absorption refrigeration cycle, and the compressor, in the vapor-compression cycle, are used to increase the pressure of the refrigerant, increasing the pressure of a liquid via a pump requires far less energy than increasing the pressure of a vapor via a compressor (due to the lower specific volume of the former). The primary input energy required for the heat absorption refrigeration cycle is for the generator in the form of thermal energy. For large industrial cooling, the input energy for the generator can be obtained in the form of waste heat from industrial processes. For example, waste heat from natural gas combustion for electricity generation is used as the heat input for absorption refrigeration systems for cooling applications in the oil and gas industry [18]. For smaller applications like residential cooling, it has been proposed that solar thermal heat can be used as the input heat for the heat absorption refrigeration cycle [19].

1.4 Challenges with the small-scale implementation of heat absorption cycle

The number of residential air conditioning units has increased substantially in recent years. It has been estimated that currently 100 million households have an air conditioning system in the United States alone [2]. Demand for air conditioning will rise drastically due to strengthening economies in developing countries and rising global temperatures resulting in a large increase in global energy demand [8-12].

As mentioned earlier, the heat absorption refrigeration system requires a heat source. In large-scale applications in the industrial sector, these systems operate on industrial waste heat which is often of high grade. The waste heat in residential units is not significant and mostly in the form of low grade heat. A potential heat source for the residential applications is solar thermal energy. It is not only an excellent source of high-grade heat but also a clean energy source. It should be noted that regions with high air conditioning demand are typically those with high solar insolation.

Currently, no small-scale solar heat absorption refrigeration systems are commercially available for use as residential air conditioning systems. Many studies have been conducted to investigate the feasibility of such a system for residential or other small scale cooling applications. Aman et al. [20] performed a thermodynamic analysis for a solar heat absorption refrigeration system intended to provide 10kW (34000 BTU/hr) of cooling to a residential building. The analysis found that the system could operate with a generator temperature of $T_G=80^\circ\text{C}$, a temperature easily attainable by a roof mounted solar collector. The input energy required for the pump was found to be $\dot{W}_p=0.89$ mW. For a vapor-compression system with the same cooling requirement and an EER of 10.7, the electrical input required to operate the compressor would be $\dot{W}_{\text{Comp}}=3.2$ kW. The electrical input for the heat absorption refrigeration cycle is almost negligible when compared to the vapor-compression system.

The study by Aman et al. [20] identifies the areas of potential concern when using a heat absorption refrigeration cycle for residential cooling. The study found that the rate of heat transfer required for the generator and absorber units far exceed the rate of heat transfer

required by the evaporator and condenser components. This is especially concerning for the absorber unit. Since the temperature of the fluid in the absorber unit is lower as compared to the condenser, rate of heat transfer from the absorber to the outside atmosphere would be lower than that of the condenser. The absorber unit was also found to have the highest rate of exergy loss, affecting the overall efficiency of the system.

Hourly analysis of a small-scale solar heat absorption refrigeration system was performed by Ozgoren et al [21]. Their study simulated solar conditions of Southern Turkey and used available models of evacuated-tube solar collectors to predict the performance of a system designed to provide 3.5kW (12000 BTU/hr) of cooling to residential and office buildings. Their analysis showed that the coefficient of performance (COP), the ratio of cooling capacity (\dot{Q}_E) to the input energy required for the generator (\dot{Q}_G), increased with increasing generator temperature for $T_G > 110^\circ\text{C}$. The study also showed that the heat transfer rate required for the absorber unit (\dot{Q}_A), increased with increasing generator temperature. The heat transfer rate required for the absorber unit can be up to four times that of the cooling capacity of the system [21]. Boudehenn et al. [22] performed an experimental study on a 5kW (15200 BTU/hr) cooling capacity heat absorption refrigeration cycle. A full scale system was built and tested in a lab using hot water to provide heating for the generator. A comparison between the experimental results and a theoretical thermodynamic model revealed a significant decrease in the performance of the experimental apparatus due to limitations of the mass transfer rate of the absorber unit [22].

1.5 Absorber Improvements

Both in theoretical and experimental studies, the absorber unit of the heat absorption refrigeration cycle appears to limit the performance of the cycle for use as a small-scale residential air conditioning system. Castro et al. [23] compared two types of absorber units for use in a small-scale heat absorption refrigeration cycle. Theoretical and experimental studies were performed on both a falling film absorber (used by Boudehenn et al. [22]) and a cocurrent bubble column absorber. Both the theoretical and experimental results revealed that a bubble column absorber has a higher rate of mass transfer between the ammonia vapor and ammonia-water mixture when compared to the

falling film absorber. Use of bubble column absorbers can allow for more efficient and more compact small-scale heat absorption refrigeration systems.

Despite being more compact than a falling film absorber, a bubble column absorber is quite sizeable when compared to a conventional vapor-compression system. Studies by Fernandez et al. predicted the number of tubes and length of tubes needed for air-cooled [24] and water-cooled [25] vertical tubular absorbers for use in a small-scale heat absorption refrigeration system. Using an air-cooled system, which is more likely to be used in a residential setting, the modelled absorber unit required 60 tubes with a length of 1.1m each, representing a total footprint of 0.9m². Just the absorber unit alone is comparable in size to an entire conventional vapor compression refrigeration unit. If the components of the system are too large when compared to a conventional vapor compression refrigeration system, a small-scale heat absorption refrigeration system may not be desirable for use as a residential air conditioning unit.

The studies by Fernandez et al. [24-25] also showed that in a vertical tubular absorber in which the gas is injected into a vertically flowing liquid from a single nozzle, the flow regime at the entrance of the absorber would be a churn or slug flow rather than a bubbly flow due to the high gas-liquid volumetric flowrates ratio. This flow regime limits mass transfer rate between the gas and liquid phases as the surface area to volume ratio of the gas-liquid interface is reduced. Since the length of the vertical tubular absorber is dependent on the mass transfer rate, it is possible to reduce the length of the absorber tubes if the flow regime can be changed from churn to bubbly, increasing the interfacial area between liquid and vapor phases. This would allow for more compact and efficient vertical tubular absorbers and heat absorption refrigeration systems that are designed for residential use.

1.6 Bubble Formation Process

Vertical tubular absorbers, as seen in Figure 1.3, typically come in the form of a bundle of vertical tubes. In each individual tube, the liquid phase of the absorber enters through an opening at the bottom of the tube causing a vertical upward liquid flow. A small diameter nozzle in the center of the bottom opening of the tube injects the gas phase

cocurrently into the upward flowing liquid. As the gas and liquid travels cocurrently up the tube, the gas phase is absorbed into the liquid phase and exits the tube at the top outlet as a single phase liquid flow. The mass transfer rate between the gas and liquid phase is highly dependent on the surface area to volume ratio of the gas phase. A two-phase flow with a larger interfacial area between the gas and liquid phase will have a higher mass transfer rate. For designers of vertical tubular absorbers, it is important to know the bubble size or flow type generated by the single nozzle.

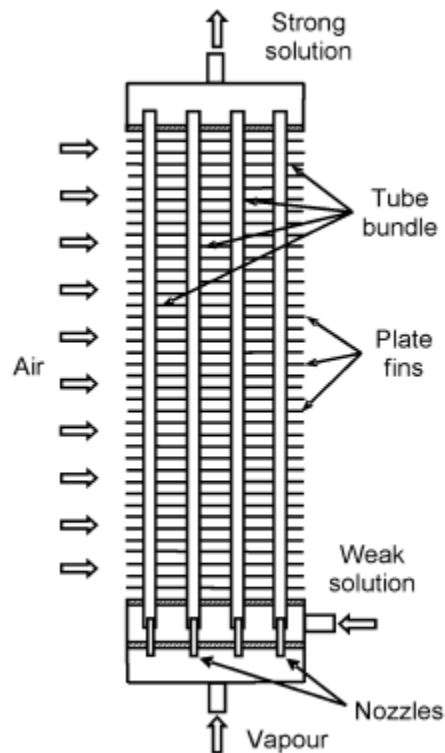


Figure 1.3: A schematic of an air-cooled vertical tubular absorber depicted in a study by Fernández et al. [25].

Bubble formation from a single nozzle in cocurrently upward flowing liquid has been studied extensively by many researchers. The size of the bubble generated by the nozzle depends on many variables. The general mechanism for bubble formation from a submerged nozzle was proposed by Ramakrishin et al. [26]. Bubble formation from a submerged nozzle occurs in two stages: Expansion Stage and Detachment Stage (see Figure 1.4).

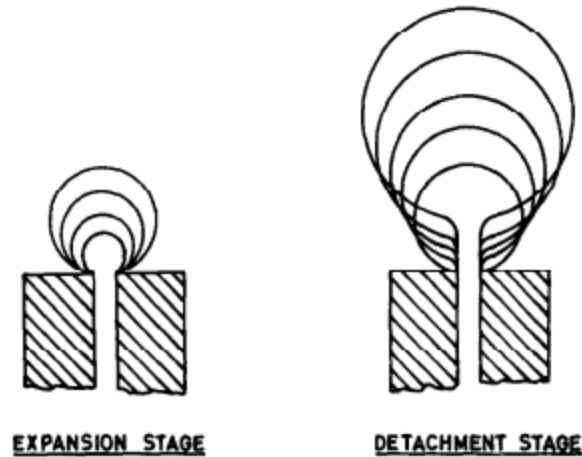


Figure 1.4: Two stages of bubble formation (Expansion and Detachment) as proposed by Ramarkrishin et al. [26].

They proposed a model to predict the size of the bubble at the end of the expansion stage as well as at the detachment stage for a bubble forming from a vertical nozzle in stagnant liquid. During the expansion phase, the bubble grows as a sphere. The volume at a given time in the expansion phase is determined by the gas flowrate and the time since the formation began. The size of the bubble at the end of the expansion stage can be determined from a force balance of the upward and downward forces acting on the bubble, which are depicted in Figure 1.5. At small gas flowrates, the end of the expansion phase occurs when the buoyancy (F_B) of the bubble in the liquid becomes greater than the force of surface tension (F_{ST}) holding the bubble to the nozzle. As the gas flowrate increases, the inertia of the gas flow adds an upward force (F_I) on the bubble. The increased flowrate also increases the rate of expansion of the bubble, which in turn, causes a downward force due to the viscous drag (F_V) from the liquid resisting the movement of the leading surface of the bubble [26].

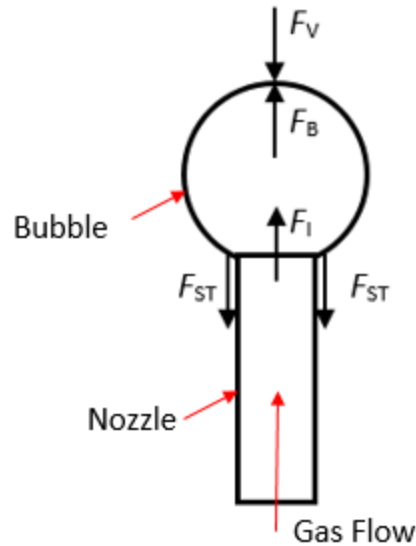


Figure 1.5: Force balance of a bubble in stagnant liquid during the expansion phase.

For a low gas flowrate, the Viscous Drag force (F_v) and Gas Inertia Force (F_I) would be negligible.

During the detachment stage, the upward forces, mainly the buoyancy, is greater than the viscous drag resisting the bubble's upward movement and the surface tension that holds the bubble to the nozzle. This causes the bubble to accelerate upwards. As the bubble accelerates upwards, a thin column of gas keeps the bubble in contact with the nozzle and allows it to continue expanding. Detachment occurs when the buoyancy force becomes greater than the force of the surface tension of the gas column. As the surface tension force decreases with increasing local radius, the surface tension of the gas column decreases as the bubble travels further from the nozzle tip. Once the buoyancy and gas inertia overcomes the surface tension, the gas column breaks in the middle, closing out the spherical bubble at the bottom, and allowing a new bubble formation to begin at the nozzle [26]. Similar to the expansion phase, the upward movement of the expanding bubble is resisted by the viscous drag of liquid. The force balance for the detachment stage of a bubble in a stagnant liquid is shown in Figure 1.6.

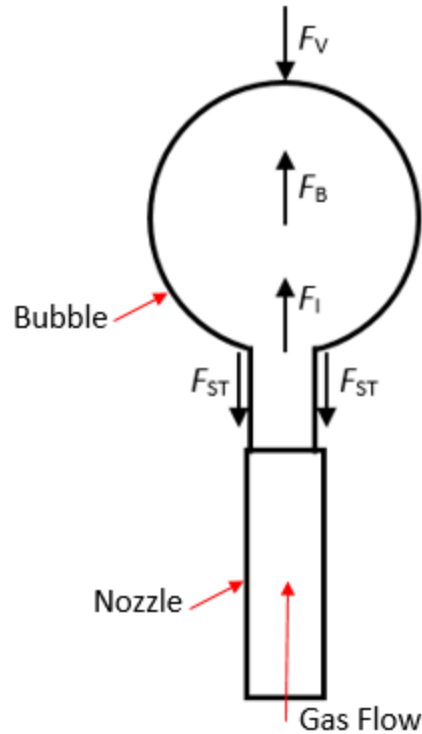


Figure 1.6: Force balance of a bubble in stagnant liquid during the detachment phase.

For tubular absorbers, the upward co-flowing liquid exerts additional drag force on the bubble causing an early bubble detachment that results in smaller bubble size when compared to bubble formation in stagnant liquid. A study by Sada et al. [27] identified the upward forces aiding bubble detachment. Like bubble formation in stagnant liquid, the gas inertia and bubble buoyancy result in an upward force that opposes the surface tension holding the bubble to the nozzle. Since the upward flowing liquid must move around the spherical bubble, the liquid exerts a drag force (F_D) on the bubble in the upward direction. This increases the magnitude of the net the upward force opposing the surface tension, resulting in smaller bubbles due to early detachment. The force balance for a bubble in the expansion and detachment phase in upward co-flowing liquid is shown in Figure 1.7.

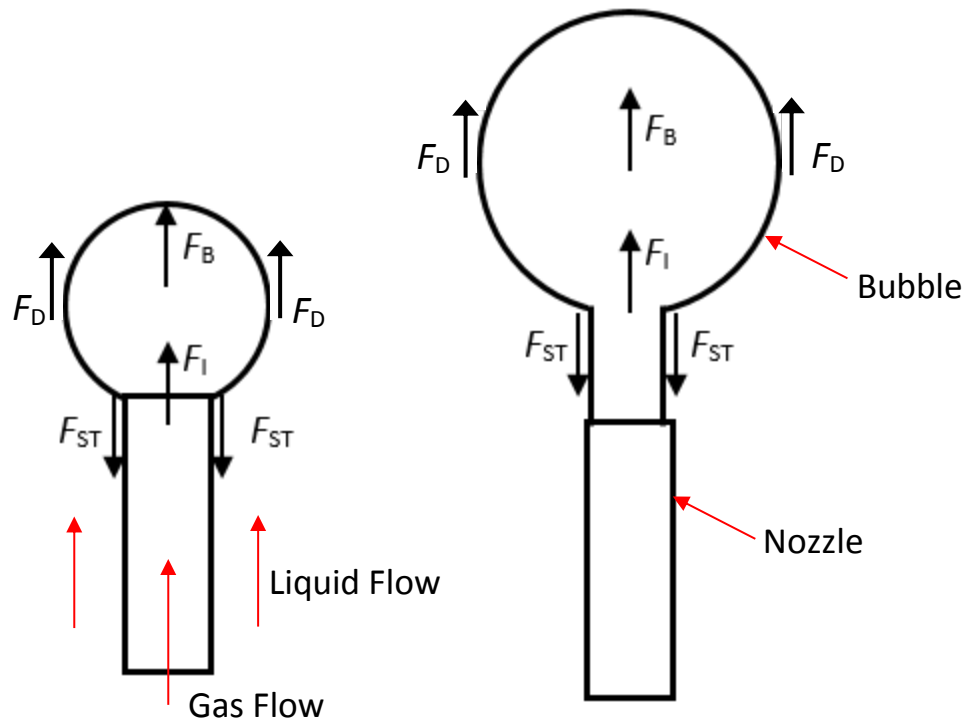


Figure 1.7: Force balance of a bubble during the expansion phase (left) and the detachment phase (right) in an upward flowing liquid.

Ramarkrishin et al. [26] discussed the effects of surface tension on the bubble size at detachment. At low gas flowrates in stagnant fluid, the surface tension and buoyancy equally contribute to the bubble detachment. As the surface tension of the bubble increases, the bubble size at detachment increases. As the flowrate increases, the influence of surface tension on the detached bubble size decreases. Sada et al. [27] also discussed the effect of surface tension on bubble formation in co-flowing liquid. Due to the addition of the upward drag force from the co-flowing liquid, the influence of surface tension decreases further. For inertia (from both the gas and liquid phases) dominated two-phase flow, surface tension has a negligible effect on bubble size [27].

Another variable that effects the detached bubble size is the nozzle diameter. In the study by Sada et al. [27] it was observed that a decrease in nozzle size resulted in a decrease in bubble size at the detachment. If the gas and liquid flowrates remain the same, as the nozzle diameter decreases, the gas velocity in the nozzle increases, resulting in an increase in the inertial force of the gas flow acting upwards on the bubble, causing an

early bubble detachment. For capillary nozzles (diameters $\ll 1\text{mm}$), it has been shown that the liquid flow rate has negligible effect on the bubble size [28].

Terasaka et al. [29] reported that the bubble shape at detachment in a liquid co-flow cannot be spherical. During the expansion stage, the bubble initially has the spherical shape when it is smaller in size. As it grows, the viscous drag of the co-flowing liquid stretches the bubble vertical deforming its shape as shown in Figure 1.8. They proposed a two-dimensional finite element model to predict the bubble shape during formation and the final bubble volume at detachment. The finite element model considered a balance between the pressure of the surrounding liquid and the pressure inside of the bubble. It also considered the force balance between the bubble buoyancy, gas inertia, liquid drag and surface tension (expressed as the equivalent radii of the gas stem attaching the bubble to the nozzle) for prediction of detached bubble volume. They compared their predicted bubble volume from their non-spherical model to the size predicted by spherical bubble models proposed in previous studies like Sada et al. [27]. It was found that the spherical bubble models were still able to accurately predict the bubble volume despite not accurately predicting the bubble shape at the detachment.

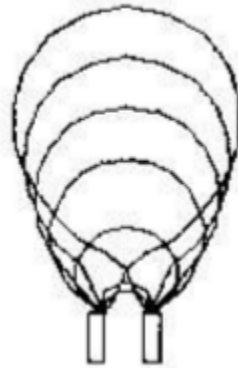


Figure 1.8: Bubble shapes during bubble formation from a submerged vertical nozzle in upward flowing liquid as predicted by Terasaka et al. [29].

The model proposed by Terasaka et al. showed the effect of liquid pressure on the bubble size at detachment [29]. An increase in pressure of the liquid phase generally causes a decrease in bubble size at detachment. During the detachment phase, the increase in

pressure exerts a greater force onto the thin column of gas that attaches the bubble to the nozzle. This increased force causes the gas column to collapse and detach a smaller volume bubble when compared to the bubble volume at a decreased pressure. The pressure effect on bubble size is mainly due to the hydrostatic pressure of the liquid column. An increase in liquid velocity will decrease the static pressure of the liquid, however, the increased inertial force will be more than the decrease in the effect of pressure on the gas column.

1.7 Two-Phase Flow Regimes

The gas flow into a wall-bounded liquid stream could establish a specific structure of the two-phase flow that depends on the gas and liquid flow rates (GLR). At low gas flow rates, the gas injected into the liquid forms individual bubbles that are dispersed into the liquid stream and each bubble remained surrounded by the liquid phase. This flow regime is called the bubbly flow. As the gas flow rate increases, the bubbles begin to form and detach more frequently. Eventually the frequency becomes great enough that the bubbles begin to coalesce after they detach from the nozzle. If the gas flowrate is increased further, the expansion of the bubble at the nozzle will be fast enough that it coalesces with the previously detached bubble while still connected to the nozzle. This leads to flow regimes that can no longer be classified as bubbly flow as there is no clear separation between bubbles. Through observation of two-phase vertical pipe flow using x-ray and flash photography, Hewitt and Roberts [30] identified five different flow regimes namely, Bubble, Slug, Churn, Annular and Wispy (see Figure 1.9). Bubble, or bubbly flow is defined as dispersed spherical gas bubbles evenly dispersed in the liquid phase. As the gas flowrate increases, the bubbles begin to coalesce to form the plug or slug bubbles present in the slug flow regime. Slug bubbles expand to the pipe wall causing an intermittent flow of regions of gas and liquid. Slug flow then transitions to Churn flow as the slug bubbles begin to coalesce and there are limited liquid breaks between gas phases. Eventually, the gas to liquid flow ratio becomes high enough that the gas flow becomes the dominant flow in Annular and Wispy flow where the gas predominantly occupies the core of the tube and the liquid flow is pushed along the tube wall in the form of the film flow [30].

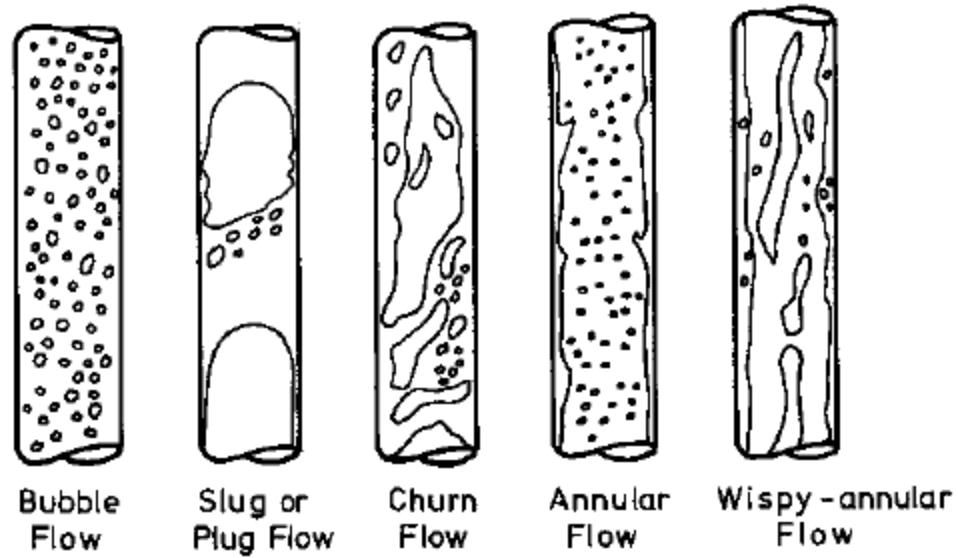


Figure 1.9: Two-phase vertical flow regimes proposed by Hewitt and Roberts [30].

Through observations of the flow regimes at different flow conditions, Hewitt and Roberts [30] also proposed a flow regime map for the two-phase flow in vertical tubes (see Figure 1.10). This map can be used to predict the flow regime present in a vertical tube based on the density (ρ) and superficial velocity (j) of the gas and liquid flows.

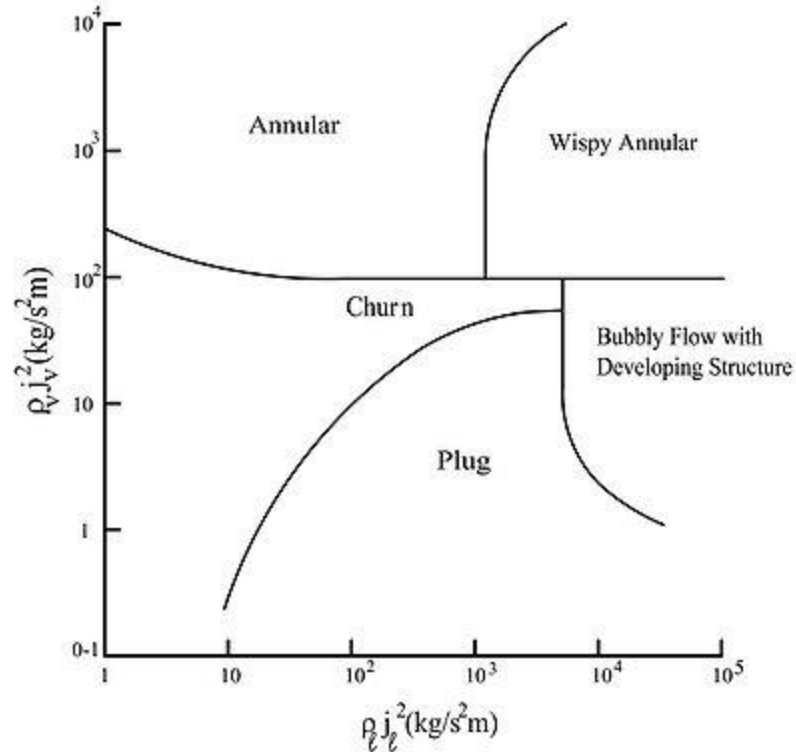


Figure 1.10: Flow regime map for vertical tubular two-phase cocurrent flow proposed by Hewitt and Roberts [30]. The subscripts l and v represent liquid and gas respectively.

A bubbly flow regime is most desirable for a vertical tubular absorber as it has the highest surface area to volume ratio. More surface area of the gas phase will allow for higher mass transfer rates from the gas phase to the liquid phase. Flow regimes such as slug or churn flow is undesirable as the surface area to volume ratio of the gas phase is decreased, reducing the mass transfer rate when compared to a bubbly flow. Vertical tubular absorbers for use in small scale heat absorption refrigeration systems, the required gas and liquid flowrates are expected to produce slug or churn flow in a conventional single nozzle system [24, 25], which affects the mass transfer rate. Hence, it is desirable that the flow regime in the absorber should be bubbly flow to allow for the maximum mass transfer rate.

1.8 Motivation

The need for more efficient air conditioning systems has motivated the current research. Increasing demand for air conditioning will increase global energy demand, resulting in potential blackouts as energy production struggles to accommodate peak demands. It can also accelerate the effects of global warming, causing exponential growth as more energy produced by greenhouse gas emitting sources is needed to provide thermal comfort in homes throughout the world. The development of a more efficient air conditioning system, which reduces energy demand from non-renewable resources, is needed. The heat absorption refrigeration cycle has the potential to greatly reduce energy demand for residential air conditioning if solar thermal energy is used as its driving energy source. Studies have been done to test the feasibility of implementing a small-scale heat absorption refrigeration as a residential air conditioning system and found that the absorber unit limited the systems performance and design. The performance and size of the absorber unit is limited by its need for high rates of mass and heat transfer in a two-phase flow. The present study has been done to improve the understanding of two-phase gas-liquid flow behaviour in vertical circular pipes and to investigate means to improve the efficiency of a vertical tubular absorber. The investigation focuses on the use of passive devices to improve the heat and mass transfer rates in the vertical tubular absorbers. Use of mesh-type bubble breakers in vertical two-phase cocurrent flow has been shown to be able to reduce the size of a bubble produced by a single gas nozzle in a two-phase vertical cocurrent flow, thus being a means to increase the mass transfer rate of a two-phase flow [31]. The previous study on mesh-type bubble breakers [31] is limited to low liquid and gas flowrates and only covers the bubble breaker's effect on the bubbly flow regime. The study also neglects the bubble breaker's effect on heat transfer, an important design variable of vertical tubular absorbers. The current study expands on the previous bubble breaker investigation to investigate the bubble breaker's effect on a larger range of two-phase flow regimes, the effect of varying bubble breaker geometry on flow behaviour, and the effect of mesh-types bubble breakers on heat transfer in two-phase flows.

1.9 Objectives

The specific objectives of this research work are to investigate the effect of various bubble breaker parameters in vertical two-phase cocurrent flow, on,

- The bubble size distribution
- The transitional behaviour of various two-phase flow regimes
- The two-phase convective heat transfer coefficient

1.10 Research Impact

The results of the current investigation can be used in the development of compact vertical tubular absorbers for use in small-scale heat absorption refrigeration systems. By investigating the effect of mesh-type bubble breakers on two-phase flow behaviour, estimations of their effect on the mass transfer rate in a vertical tubular absorber can be made. The study on the bubble breaker's effect on heat transfer in two-phase flow can be used to make estimates on the heat transfer rate of a vertical tubular absorber. By varying the geometry of the bubble breakers in both the flow characterization study and the heat transfer study, the results can be used to optimize the bubble breaker design to maximize the enhancement of heat and mass transfer rates.

1.11 Thesis Outline

The first chapter is intended to provide a broader overview of the problem of increasing energy demand for air conditioning and the challenges of implementing solar thermal heat absorption refrigeration systems as residential air conditioning units. In many studies that review the feasibility of small-scale solar thermal heat absorption refrigeration systems, the absorber unit is shown to limit the system performance. The main cause of the limitation is the reduced mass transfer rates between a gas and liquid phase. It has been proposed that mesh-type bubble breakers can be used to increase the surface area to volume ratio of the gas-liquid interface in a vertical tubular absorber to increase the mass transfer rate between the phases.

The second chapter focuses on the investigation of the effect of various parameters of mesh-type bubble breakers on the bubble size and two-phase flow regime transitions. The parameters considered in this investigation are the pore size, length and position of the bubble breaker. A wide range of gas and liquid flow rates were considered that covered the two-phase flow regimes from bubbly to churn.

The third chapter investigated the effect of mesh-type bubble breakers on heat transfer in two-phase vertical pipe flow. The results of the effectiveness of mesh-type bubble breakers as heat transfer enhancement devices are presented and discussed. The effect of flow regimes on two-phase convective heat transfer is also discussed.

The fourth chapter summarizes the objectives and scope of the present work along with the key findings from this research. Some future recommendations are also provided to extend this work and address some unanswered questions from this research.

1.12 Co-Authorship Statement

This thesis has been written in an integrated article format. The second chapter, titled “Bubble Size Prediction and Flow Regime Analysis for Two-Phase Vertical Co-flow in the Presence of a Mesh-Type Bubble Breaker” has been submitted to the International Journal of Multiphase Flow as a separate paper and is co-authored by Kamran Siddiqui. The third chapter, titled “Two-Phase Vertical Co-Flow in the presence of a Mesh-Type Bubble Breaker” is also co-authored by Kamran Siddiqui and will be submitted to an academic journal relating to fluid mechanics and heat transfer.

1.13 References

- [1] "Energy Efficiency Trends in Canada, 1990 to 2009." *Natural Resources Canada*. September 7, 2012. Accessed April 19, 2016.
<http://oee.rncan.gc.ca/publications/statistics/trends11/chapter3.cfm?attr=0>.
- [2] "Air Conditioning in nearly 100 million U.S. homes." *U.S. Energy Information Administration*. August 19, 2011. Accessed April 19, 2016.
<https://www.eia.gov/consumption/residential/reports/2009/air-conditioning.cfm>.
- [3] Auffhammer, M. 2014, "Cooling China: The Weather Dependence of Air Conditioner Adoption." *Frontiers of Economics in China*, **9**(1), pp. 70-84.
- [4] Davis, Lucas. "Air Conditioning and Global Energy Demand." *Energy Institute at Haas*. April 27, 2015. Accessed April 19, 2016.
<https://energyathaas.wordpress.com/2015/04/27/air-conditioning-and-global-energy-demand/>.
- [5] Hydro One Networks, *Ontario Energy Board*, 2003, "Electricity Demand in Ontario."
- [6] "Electricity Prices." *Ontario Energy Board*. Accessed April 19, 2016.
<http://www.ontarioenergyboard.ca/oeb/Consumers/Electricity/ElectricityPrices>.
- [7] Pidd, Helen. "India Blackouts Leave 700 Million without Power." *The Gaurdian*. July 31, 2012. Accessed April 19, 2016.
<http://www.theguardian.com/world/2012/jul/31/india-blackout-electricity-power-cuts>.
- [8] Petri, Y. and Calderia, K. 2015, "Impacts of global warming on residential heating and cooling degree-days in the United States." *Scientific Reports*, **5**, pp. 12427-12441.
- [9] Sivak, M. 2013, "Will AC Put a Chill on Global Energy Supply?" *American Scientist*, **101**(5), pp. 101-104.
- [10] "Air Conditioning." *Energy.Gov*, Accessed April 19, 2016.
<http://energy.gov/energysaver/air-conditioning>.
- [11] "Electricity Data." *U.S. Energy Information Administration*, Accessed April 19, 2016.
https://www.eia.gov/electricity/monthly/epm_table_grapher.cfm?t=epmt_1_1.

- [12] Isaac, M. and Van Vurren, D.P., 2009, "Modeling global residential sector energy demand for heating and air conditioning in the context of climate change." *Energy Policy*, **37**(2), pp. 507-521.
- [13] Biwole, P.H., Woloszyn, M. and Pompeo, C., 2008, "Heat transfers in a double-skin roof ventilated by natural convection in summer time." *Energy and Buildings*, **40**, pp. 1487-1497.
- [14] Aydin, O., 2006, "Conjugate heat transfer analysis of double pane windows." *Building and Environment*, **41**, pp. 109-116.
- [15] Kuhns, M., "Planting Trees For Energy Conservation: The Right Tree in the Right Place." *Forestry: Utah State University*, Accessed April 19, 2016. <http://forestry.usu.edu/htm/city-and-town/tree-selection/planting-trees-for-energy-conservation-the-right-tree-in-the-right-place>.
- [16] "Air Conditioning Your Home." *Natural Resources Canada*, Accessed April 19, 2016. <http://www.nrcan.gc.ca/energy/publications/efficiency/residential/air-conditioning/6051>.
- [17] Moran, M. J., and Shapiro, H.N., 2007, *Fundamentals of Engineering Thermodynamics*, Hoboken, NJ: John Wiley.
- [18] Kalinowski, P., Hwang, Y., Radermacher, R., Al Hashimi, S, and Rogers, P., 2009, "Application of waste heat powered absorption refrigeration system to the LNG recovery process." *International Journal of Refrigeration*, **32**, pp. 687-694
- [19] Nkwetta, D.N., and Sandercock, J., 2016, "A state-of-the-art review of solar air-conditioning systems." *Renewable and Sustainable Energy Reviews*, **60**, pp. 1351-1366.
- [20] Aman, J., Ting, D.S., and Henshaw, P., 2014, "Residential solar air conditioning: Energy and exergy analyses of an ammonia-water absorption cooling system." *Applied Thermal Engineering*, **62**, pp. 424-432.
- [21] Ozgoren, M., Bilgili, M. and Babayigit, O., 2012, "Hourly performance prediction of ammonia–water solar absorption refrigeration." *Applied Thermal Engineering*, **40**, pp. 80-90.
- [22] Boudenhenn, F., Demasles, H., Wyttenbach, J., Jobard, X., Cheze, D. and Papillon, P., 2012 "Development of a 5 kW Cooling Capacity Ammonia-water

- Absorption Chiller for Solar Cooling Applications.” *Energy Procedia*, **30**, pp. 35-43.
- [23] Castro, J., Oliet, C., Rodriguez, I., and Olivia, A., 2009, “Comparison of the performance of falling film and bubble absorbers for air-cooled absorption systems.” *International Journal of Thermal Sciences*, **48**, pp. 1355-1366.
- [24] Fernandez, J., Uhia, F.J., and Sieres, J., 2007, “Analysis of an air cooled ammonia–water vertical tubular absorber.” *International Journal of Thermal Sciences*, **46**, pp. 93-103.
- [25] Fernandez, J., Sieres, J., Rodriguez, C., and Vazquez, M., 2005, “Ammonia–water absorption in vertical tubular absorbers.” *International Journal of Thermal Sciences*, **44**, pp. 277-288.
- [26] Remakrishnan, S., Kumar, R., and Kuloor, N.R., 1969, “Bubble formation under constant flow conditions.” *Chemical Engineering Science*, **24** pp. 731-747.
- [27] Sada, E., Yasunishi, A., Katoh, S., and Nishioka, M. 1978, “Bubble formation in flowing liquid.” *The Canadian Journal of Chemical Engineering*, **56**, pp. 669-672.
- [28] Chuang, S.C., and Goldschmidt, V.W., 1970 “Bubble Formation Due to a Submerged Capillary Tube in Quiescent and Coflowing Streams.” *Journal of Basic Engineering*, **92**(4), pp. 705-711.
- [29] Terasaka, K., Tsuge, H., and Matsue, H. 1999, “Bubble formation in cocurrently upward flowing liquid.” *The Canadian Journal of Chemical Engineering*, **77**, pp. 458-464.
- [30] Hewitt, G.F, and Roberts, D.N. 1969, “Studies of two-phase flow patterns by simultaneous x-ray and flash photography.” (AERE-M--2159), Technical report, Atomic Energy Research Establishment, Harwell (England)
- [31] Gadallah, A.H. and Siddiqui, K., 2015, “Bubble breakup in co-current upward flowing liquid using honeycomb monolith breaker.” *Chemical Engineering Science*, **131**, pp. 22-40.

Chapter 2

2 Bubble Size Prediction and Flow Regime Analysis for Two-Phase Vertical Co-flow in the Presence of a Mesh-Type Bubble Breaker

2.1 Introduction

Bubble column reactors are essential components in many chemical and mechanical processes involving two-phase flows in which the mixing of gas and liquid phases is required [1-3]. They are widely used due to their capability to allow high rates of heat and mass exchange between gas and liquid phases. The basic structure of a bubble column reactor is a vertical cylinder containing flowing or stationary liquid with gas injected at the bottom of the vessel in the form of bubbles that rise and mix with the liquid phase and facilitate the heat and/or mass exchange. In the biochemical industry, bubble column reactors are used as bioreactors for the production of proteins, enzymes and antibiotics as well as other industrial products [7-12]. Other chemical processes such as wastewater treatment also utilize bubble column reactors [13-14]. For mechanical applications, bubble column reactors are used as absorbers units for heat absorption refrigeration systems [15-17].

In bubble column reactors, the size of the bubble entering the liquid domain is an important design parameter, since it has a direct influence on the two-phase exchange process. A large single bubble will have relatively small surface area to volume ratio compared to numerous small bubbles with the same cumulative volume as the large bubble. The smaller surface area to volume ratio reduces the interfacial area between the two phases, which results in the lower heat and mass exchange rates between the two phases. The growth and detachment of bubbles formed in a two-phase gas liquid vertical cocurrent flow from a conventional single vertical gas nozzle has been well documented in the scientific literature. Sada et al. [18] performed an experimental study to measure the size of single and coalesced bubbles that detached from a single nozzle in an unbounded vertical liquid flow. Their results show that the bubble size for liquid-inertia dominated flow can be predicted by a modified Froude number correlation that relates the

gas inertial forces, bubble buoyancy forces and the liquid drag on the generated bubble, to the bubble size and nozzle diameter. They observed that the bubble size increases with increasing gas flow rate and decreases with increasing liquid flow rate. Teresaka et al. [19] also investigated the bubble formation in upward flowing liquid in a column. Through observation of bubble growth at the nozzle tip, they proposed a non-spherical bubble growth model considering the balance of internal and external pressure forces as well as the inertial forces from both gas and liquid flows exerted onto the bubble interface. The model predicted the growth of the bubble volume at the nozzle and the volume of the bubble after detachment. The bubble size predictions from their model were in good agreement with experimental results over a range of gas-liquid flow rates ratio (GLR). However, the model was not able to accurately capture the shape of the formed bubbles. Chen et al. [20] proposed an interfacial element model to predict the shape and growth of non-spherical bubbles. They compared the bubble size predicted from their model with the experimental results from Teresaka et al. [21] and found the model predictions to be in good agreement with the experimental data. The model also effectively predicted the shape of a single bubble forming at a nozzle in an upward liquid flow.

In some applications of bubble column reactors, the ratio of gas-liquid flow rates (GLR) exceeds the condition at which a single vertical nozzle can produce bubbly flow [15, 16]. Hence, two-phase flow regimes at higher GLRs have been studied in the past. Hewitt [21] and Hewitt and Roberts [22] studied two-phase flow regimes in both vertical and horizontal pipes. Through experimental observation of two-phase vertical co-flow, they identified four regimes: Bubbly, Slug, Churn and Annular. Generally, as the GLR increases, the flow regime transitions from a bubbly flow to slug, to churn and finally to annular flow. It has been found that the flow conditions at which the transition from bubbly to slug flow regime occurs is not very sensitive of the pipe geometry [23]. Flow transition maps were created to predict the flow regime based on the fluid properties and flowrates of both phases [21, 22]. However, these maps are valid for the fully developed region of the flow, downstream of the entrance.

Ujang et al. [24] and Waltrich et al. [25] studied the evolution of two-phase flow from the entrance region to the fully developed region. These studies show that the flow regime is not only dependent on the GLR but also that the flow regime changes along the length of the pipe as the gas regions coalesce. When the gas is injected into the liquid flow, the initial flow regime may not be the same as the predicted regime from the flow transition maps proposed by Hewitt, and Hewitt and Roberts [21, 22]. A two-phase flow with gas and liquid flowrates corresponding with a slug flow regime can begin as a bubbly flow regime at the pipe entrance immediately downstream of the gas nozzle. As the two-phase flow continues through the pipe, the initial nozzle generated bubbles begin to coalesce forming plug and slug bubbles eventually reaching its fully developed flow regime as predicted by Hewitt [21], and Hewitt and Roberts [22].

For bubble column reactors that operate at high GLRs, the regime is not expected to be of the bubbly flow, which constitutes the highest surface area to volume ratio for the gas phase. Hence, to achieve higher mass exchange in the column reactors at high GLRs, a mechanism needs to be used to break large (slug or churn) gas regions and transition the regime back to bubbly flow which otherwise would be in slug or churn flow mode. Several techniques have been reported in literature to generate smaller bubbles or to break large bubbles. Fadavi et al. [26] investigated the use of a sparger and found a reduction in the bubble size by adding a rotational flow with a passive swirl device to the liquid before the gas was released through the sparger. This swirl increased the shearing force from the rotational liquid and caused early bubble detachment that resulted in smaller bubble generation. The effect of rotational flow was also investigated by Sobrino et al. [27]. They used a perforated plate, rotating at a set speed, to release gas into a fluidized bed. It was found that an increase in the rotational speed of the bed decreased the bubble size at detachment due to the increase in shearing forces. Manabu et al. [28] investigated the use of a porous nozzle in a stationary water bath. At low gas flow rates, the porous nozzle was found to reduce the size of the injected bubbles. As the gas flow rate increased, the pores' effectiveness reduced and the gas region similar to the slug regime was formed in the pipe. They concluded that the pore has no effect at the higher gas flow rates and the size of the gas region was only dependent on the nozzle diameter.

The generation of turbulent liquid flow is a common way to control bubble and droplet size in two-phase flows. The study of turbulence in two-phase flow is dated back to the pioneering work of Kolmogorov and Hinze [29, 30]. Their studies showed that the size of a stable liquid droplet in a turbulent liquid flow is dependent on the integral length scale of the turbulent flow and the turbulent intensity. They proposed a critical Weber number to predict the stable droplet size in a two-phase flow that relates the shear stress of a turbulent eddy to the surface tension of the dispersed phase. If the Weber number of a flow is greater than the critical Weber number, the turbulent shear stress would cause the droplet to split until the stable droplet size has reached. The same relation can be used in gas-liquid flows to predict the stable bubble size when the liquid flow is turbulent. In recent years, studies have been performed to estimate the critical Weber number and stable bubble or droplet size for a range of specific flows including gas-liquid flow in tubes [31-34]. By increasing the turbulent intensity in a gas-liquid flow, the chance and frequency of bubble break-up can be increased allowing smaller and more dispersed bubbles to be generated.

Passive devices placed downstream of a single nozzle or bubble dispersion system have also been studied as mechanisms to break up bubbles into smaller daughter bubbles. These devices can be used to add a shearing force to the flow similar to that of a turbulent eddy. Miyahara et al. [35, 36] investigated bubble breakup in a two-phase vertical co-flow by using an orifice plate and a converging-diverging nozzle. Bubbles were formed from a single nozzle in an upward flowing liquid. The two-phase flow continued through an orifice plate or converging-diverging nozzle forcing a turbulent jet to form. The increased turbulence broke the initial bubble into multiple smaller daughter bubbles. A critical Weber number correlation was developed as a function of the Reynolds number of the flow through the orifice [36]. The use of multiple sieve trays has been shown to increase mixing of liquid and gas phases for a variety of flow regimes [37-39]. The positioning of the trays, the pore size and the opening ratio of the sieves can affect the bubble size distribution, liquid mixing and gas holdup in a vertical tube. Wire meshes were studied by Prasser et al. [40] and were found to significantly reduce the size of a single nozzle-generated bubble in a bubbly flow regime. The wire mesh had an

insignificant effect when the flow downstream of the wire mesh was in the slug regime [40].

A honeycomb monolith breaker with elongated pores of uniform size was studied by Gadallah and Siddiqui [41]. Their bubble breaker was able to reduce the size of nozzle-generated bubbles by 60%. They also proposed the existence of an optimal liquid velocity that allows for minimal bubble coalescence downstream of the bubble breaker. Mesh-type bubble breakers are an interesting solution as they combine both a shearing force of wire mesh and the two-phase flow dynamics in microchannels. The study of two-phase flow regimes in microchannels has recently been an active topic of research [42-44]. The flow regime maps for microchannels differ from those of previously mentioned studies that investigated the bubble dynamics and two-phase flow in larger diameter pipes.

The above literature review shows that there are several methods to reduce the size of bubbles in a two-phase vertical co-flow. The studies of break-up techniques are mainly limited to low gas flow rates and were only implemented in a bubbly flow regime. The present study is focused in a detailed investigation of the effect of mesh-type bubble breakers downstream of a single gas nozzle in upward flowing liquid flow. The effect of bubble breaker pore size, length and position are studied for a large range of two-phase flow regimes.

2.2 Nomenclature

Variables

a	Major axis length, m
b	Minor axis length, m
d_b	Bubble/Drop Diameter, m
D_i	Inside tube diameter, m
D_o	Outside tube diameter, m
D_{bb}	Bubble breaker diameter, m
Fr	Froude number, dimensionless
g	Acceleration of gravity, m/s^2
GLR	Gas-liquid flow ratio, dimensionless
H	Height, m
L	Length, m
N	Number of samples
pd	Pore density, pores/ m^2
Q_G	Gas flowrate, LPM
Q_L	Liquid flowrate, LPM
Res	Bubble breaker pore Reynolds number, dimensionless
sf	Bubble breaker shape factor, dimensionless
S	Pore Size, m

U	Superficial liquid velocity, m/s
u	Superficial gas velocity, m/s
V	Turbulent velocity difference, m/s
We	Weber number, dimensionless
ρ_G	Gas density, kg/m ³
ρ_L	Liquid density, kg/m ³
σ	Surface tension, N/m
δ	Nozzle inside diameter, m
ν	Kinematic viscosity,

2.3 Experimental Setup and Procedure

The experimental setup used in this study is shown in Figure 2.1. The setup consisted of a vertical glass pipe with an inside diameter of $D_i=15\text{mm}$ and an outside diameter of $D_o=19\text{mm}$. The glass pipe was placed inside a transparent polycarbonate channel with a square cross section, filled with water. The outer transparent channel was used to offset the image distortion caused by the curvature of the center glass pipe. Tap water at room temperature entered through the inlet on the upper side of the square channel, flowed down through the square channel and entered the glass pipe at the bottom of the channel, inducing an upward vertical flow through the center glass pipe (see Figure 2.1). The outlet of the vertical glass pipe was open to the atmosphere. The hydrostatic pressure of the water at the nozzle tip was 103 kPa. Air from a pressurized supply line at room temperature entered through an inlet at the bottom of the square channel. The air flowed through a glass nozzle with an inside diameter of $D_i=2.5\text{mm}$ and an outside diameter of $D_o=3.2\text{mm}$. To avoid pressure fluctuations from the pressurized supply line for the air flow, the air first entered a settling tank located in the laboratory. From the settling tank, the air flowed through a small diameter tube to the glass nozzle to provide a large

pressure drop, reducing the pressure fluctuations even further. The air pressure was monitored by a pressure gauge at directly upstream of the nozzle and found to be between 150-250 kPa for the range of gas flowrates used in testing. The nozzle tip, where the air was injected into the upward flowing water, was at a height of 30 mm from the entrance of the center glass pipe.

The water and air flowed co-currently up the center pipe and exited the apparatus as a two-phase mixture through the outlet at the top of the square channel (see Figure 2.1). The flowrates of both water and air were controlled and measured by variable area flowmeters. An Omega FL-2012-SS flowmeter was used to measure and control the air flowrate. Two flow meters, Omega FL-2056-SS and Omega FL-2053-SS, were used to measure and control the liquid flowrate. The FL-2056-SS was used for liquid flowrates above 0.63LPM and the FL-2053-SS was used for liquid flowrates below 0.63LPM. During experiments, the liquid and gas flow rates varied from 0.06-3.79 LPM and 0.2-2.5 LPM, respectively. The corresponding GLR ranged from 0.05 to 39.6 allowing the experiment to investigate bubbly, slug and churn flow regimes.

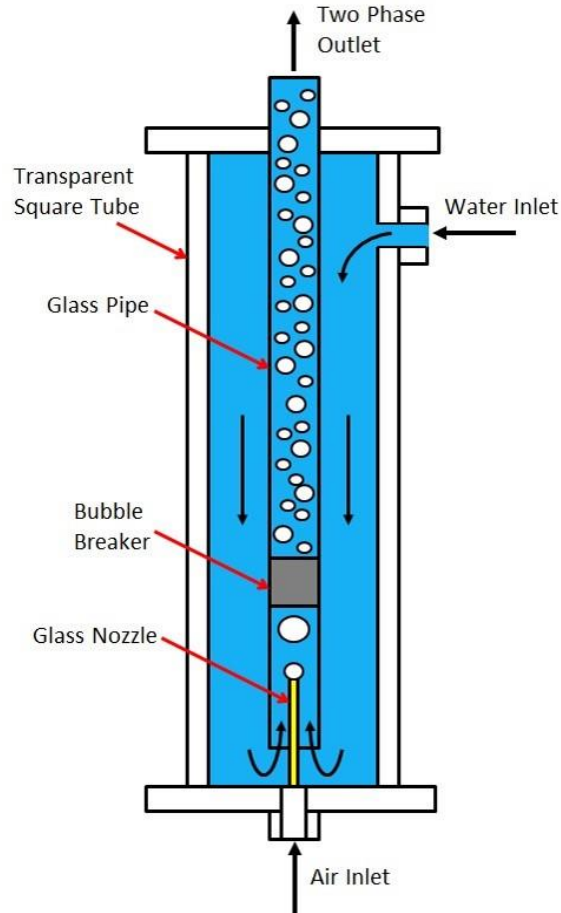


Figure 2.1: Schematic of the experimental setup.

The dimensions of this experimental apparatus were chosen to allow for comparison of the results from this experiment to previous studies of mesh-type bubble breakers [41]. The dimensions are also similar to the component size of absorber units used in small scale heat absorption refrigeration components; the results of the current experiment can be used to provide insights on the design of these components [12, 13].

Mesh-type bubble breakers of different dimensions were made from PLA plastic using a Makerbot Replicator 3D printer. A cross-sectional view of the bubble breaker design is shown in Figure 2.2, which also illustrates the geometric parameters of the breaker design. A bubble breaker was placed in the center glass pipe above (downstream of) the glass nozzle (see Figure 2.3). The key geometric parameters varied in this study to investigate their influence on the bubble breakup and two-phase flow regime were the

length of the bubble breaker (L), the distance of the bubble breaker from the glass nozzle tip (H), and the pore size (S) as shown in Figures 2.2 and 2.3. The effect of pore size was studied using four bubble breakers with pore sizes of $S=1\text{mm}$, $S=2\text{mm}$, $S=3\text{mm}$ and $S=4\text{mm}$ while the bubble breaker position and length remained constant at $H=25\text{mm}$ and $L/D_{\text{BB}}=1$, respectively. The effect of bubble breaker length was studied using bubble breakers with lengths of $L/D_{\text{bb}}=0.5$, $L/D_{\text{bb}}=1$ and $L/D_{\text{bb}}=2$ while the bubble breaker pore size and position remained constant at $S=2\text{mm}$ and $H=25\text{mm}$ respectively. The effect of the bubble breaker position was studied at the bubble breaker positions of $H=13\text{mm}$, $H=25\text{mm}$ and $H=50\text{mm}$ while the length was held constant at $L/D_{\text{bb}}=1$. Pore sizes of $S=1\text{mm}$ and $S=2\text{mm}$ were used at each bubble breaker position. Other parameters such as the mesh wall thickness ($t=0.5\text{mm}$) and the diameter of the bubble breaker ($D_{\text{bb}}=15\text{mm}$) were constant for all bubble breakers used in the study.

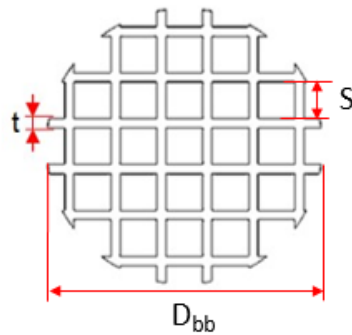


Figure 2.2: Bubble Breaker cross section showing various geometric parameters; bubble breaker thickness (t), diameter (D_{bb}) and pore size (S).

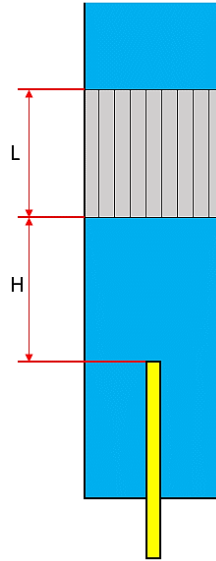


Figure 2.3: Schematic of the positioning of the bubble breaker in the center pipe and other related parameters; the distance between the nozzle tip and bubble breaker (H) and the bubble breaker length (L).

A Photron Fastcam (SA4) high-speed camera was used to capture greyscale images of the two-phase flow. A backlit shadowgraphy technique was implemented using a halogen lamp and diffuser screen to improve the signal to noise ratio of the images and provide a clear contrast between the liquid and gas phases of the flow. For each experimental run, images were captured at a rate of 1000 fps for approximately 5 seconds. The images were used for both qualitative analysis for flow regime characterization and quantitative analysis for bubble size estimation.

For bubble size estimation, an in-house interactive image-processing algorithm in the MATLAB environment was used to determine the mean diameter of the bubbles generated by the nozzle and by the bubble breaker. The size of individual bubbles were approximated from individual images.

In this algorithm, the user interactively identifies the major and minor axis of each individual bubble in a given image (see Figure 2.4). Using the major and minor axis, the bubble was then approximated as an ellipse. The bubble size was calculated for bubbles within 80 mm column height from the breaker exit. The equivalent bubble diameter for

each bubble was calculated using Equation (1) where a and b are the major and minor axes lengths, respectively. Figure 2.5, shows an image and the corresponding bubbles detected and used for bubble size computation.

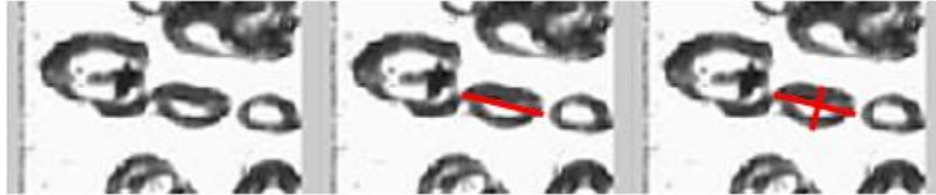


Figure 2.4: Illustration of the major and minor axes detection of an individual bubble in an image segment.



Figure 2.5: The identified bubbles approximated as ellipses are shown plotted over an original image.

$$d_b = \sqrt[3]{a^2b} \quad (1)$$

As seen in Figures 2.4 and 2.5, the backlit shadowgraphy technique allowed for easy manual identification of the bubbles and the accurate approximation of their boundaries. The uncertainty in the bubble size measurement was due to the pixel resolution of the image and the interactive bubble detection algorithm. The pixel resolution for each image was 8 pixels/mm or 0.125pixels/mm. The uncertainty in interactively detecting and recording the bubble boundaries (the major and minor axes) was within ± 2 pixels or ± 0.24 mm. Considering the error propagation from these elemental error sources, the uncertainty in the calculated equivalent diameter for an individual bubble was ± 0.21 mm. The depth of field could also cause error using this method. Depending on the location of the detected bubble in the vertical pipe, it may appear to be of different sizes. The error due to the depth of the field was also computed and for the most extreme cases i.e. at the closest and farthest locations, it was found to be 3%.

In order to determine the mean bubble size at a particular operating condition and bubble breaker geometry, the average equivalent diameter of 120 bubbles was calculated. As seen in Figure 2.5, the size of every bubble could not be determined as some bubbles were partially covered by other bubbles present in the pipe. For each frame used in the analysis, only the bubbles with visible boundaries were measured using the MATLAB algorithm. One frame did not have enough bubbles to collect all 120 measurements. As the bubbles were moving slowly through the image segment, detection of bubbles in consecutive images would result in the duplication of the bubbles, which would bias the statistical estimates. Hence, to ensure no bubble duplication, 250 frames were skipped in between each considered frame allowing for an entirely new set of bubbles to be sized. The uncertainty in the mean equivalent bubble diameter was estimated in the form of the standard error of the mean given as,

$$\Delta \bar{d}_b = \frac{\sqrt{\frac{1}{N} \sum (d_b - \bar{d}_b)^2}}{\sqrt{N}} \quad (2)$$

2.4 Results and Discussion

2.4.1 Bubbly Flow Analysis

The images acquired by the high-speed camera were used to analyze the effect of the bubble breaker when a bubbly flow regime was present downstream of the bubble breaker. All bubble breakers tested in the experiment were observed to reduce the size of the nozzle-generated bubbles by breaking them into multiple small bubbles that are dispersed downstream. The bubble breakers were also observed to breakup some instances of slug and churn flow allowing for bubbly flow at higher GLRs. A qualitative comparison of the two-phase cocurrent pipe flow in the presence and absence of a bubble breaker is provided in Figure 2.6. The figure also shows the relative performances of bubble breakers with different pore sizes. A more detailed analysis of the flow regime transition is discussed in the following section.

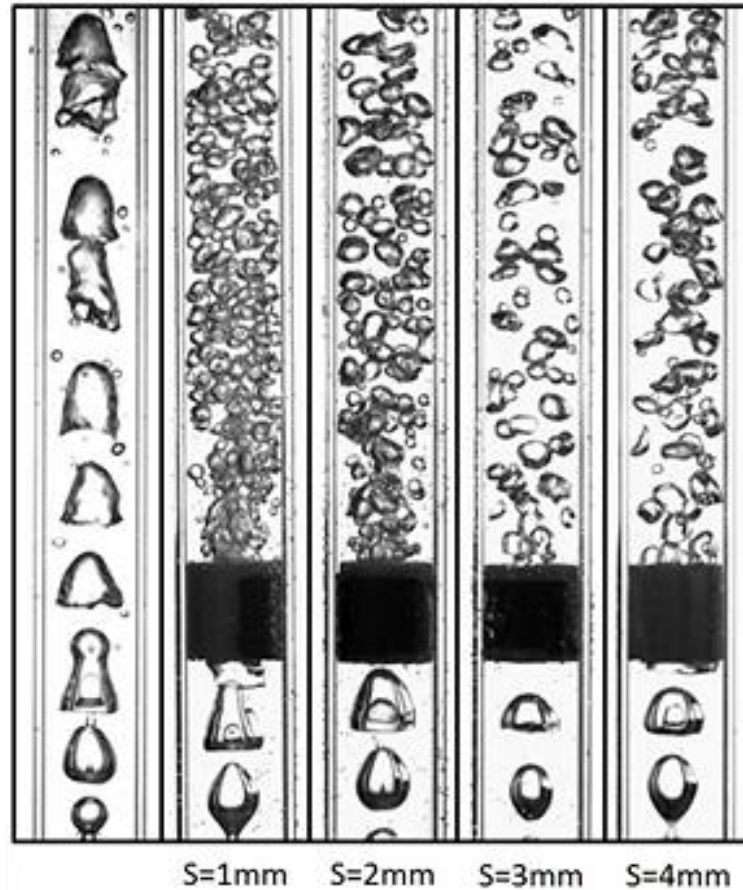


Figure 2.6: Qualitative comparison of the two-phase flow without a bubble breaker and in the presence of bubble breakers with different pore sizes (shown underneath the respective images). The bubble breaker was located 25 mm downstream of the nozzle tip. The length of each bubble breaker was $L/D_{bb}=1$. The liquid and gas flow rates in all the images were $Q_L=2.5$ LPM and $Q_G=0.5$ LPM, respectively.

As seen in Figure 2.6, the large bubbles generated by the nozzle pass through the pores of the bubble breaker to create smaller and more dispersed daughter bubbles. When comparing bubble breaker pore size, it can be seen that the size of the bubbles generated by the bubble breaker increase as the pore size increases. Using the in-house MATLAB code described in the Experimental Setup and Procedure section, the mean diameter of the bubbles generated by the bubble breakers at each set of flow combinations was determined. Figure 2.7 shows a plot comparing the mean bubble size downstream of

bubble breakers of different pore sizes, as a function of the GLR. The error bars on the plot represent the standard error of the mean bubble diameter.

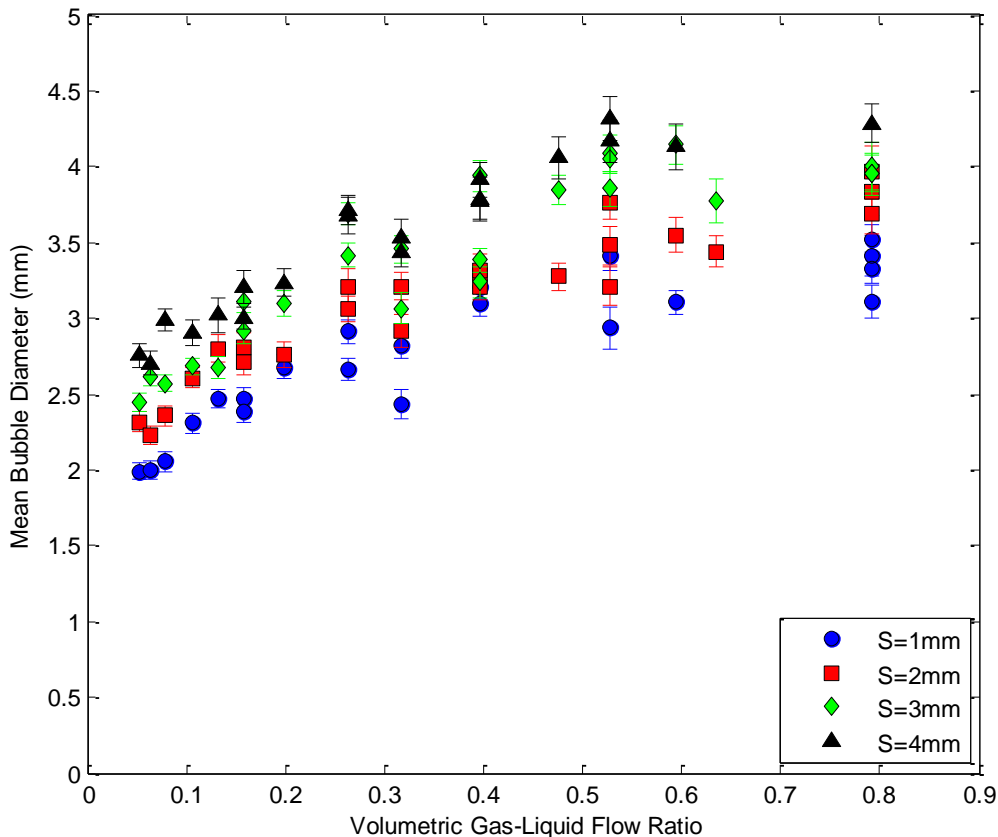


Figure 2.7: Mean diameters of bubbles generated by bubble breakers of different pore sizes versus the volumetric gas-liquid flow ratios for gas-liquid vertical co-flow.

Two trends can be seen in Figure 2.7. Firstly, the plot shows that bubble size increases with increasing pore size. Similar to the slug bubbles moving through a microchannel, the size of the gas phase inside the bubble breaker pore is limited by the pore size. However, as seen in Figure 2.7, the bubble size is not equal to the pore size. The bubbles generated by the smallest pore sizes, $S=1\text{mm}$, are larger than the pore spacing. The bubbles generated by the largest pores, $S=4\text{mm}$, are smaller than pore spacing for most of the GLR range. This can be explained by the flow regime within the pores of the bubble breaker. For smaller pore sizes, the flow is more likely to form an elongated slug flow

and reduce the amount of mixing between the liquid and gas phases within the bubble breaker pores. As shown by Akbar et Al. [45], the flow regime of two-phase flow in a micro channel is highly dependent on the liquid Weber number and gas Weber number defined in Equations 3 and 4, respectively [45].

$$We_L = \frac{U^2 S \rho_L}{\sigma} \quad (3)$$

$$We_G = \frac{u^2 S \rho_G}{\sigma} \quad (4)$$

In a microchannel of $S < 1\text{mm}$, Akbar et al. [45], found that the gas Weber number at which the flow transitions from surface tension dominated flow (bubbly and slug flow) to inertia dominated flow (churn and annular flow), decreased as the liquid Weber number decreased. At a given liquid flow rate, a reduction in the pore size reduces the liquid Weber number and the flow within the bubble breaker pores will more likely be of churn or annular flow type. For a bubble breaker with a pore size of $S=1\text{mm}$, the gas phase passing through the bubble breaker pores will form elongated slugs or annular flow. The gas phase will then exit the pore and begin forming a spherical bubble until the liquid breaks between the gas slug and forces the bubble to detach from the pore. A longer gas phase exiting the breaker pore will form a bubble with a diameter greater than the pore size. For a bubble breaker with a pore size of $S=4\text{mm}$, the gas phase will more likely form a bubbly or weak slug flow regime with more frequent liquid breaks between the gas phases. This would lead to the formation of bubbles that are equal to or smaller than the bubble breaker pore size.

The second trend that can be seen in Figure 2.7 is the increase in bubble size as the GLR increases. The trend, which can be seen for all four sizes of pores that were tested, shows a steeper increase in the bubble size in the lower range of GLR and a levelling off of the bubble size as the flow begins to transition towards slug flow. This trend is similar to the increase in bubble size with an increase in GLR reported previously for a single nozzle generated bubble in two-phase co-current flow [18]. For a single nozzle, the size of the generated bubble is dependent on the inertia of the gas flow, inertia of the liquid flow, the buoyancy of the formed bubble, the nozzle size and the surface tension holding the

bubble to the nozzle tip. As the GLR increases, more gas can enter the bubble before the liquid inertial forces and gas buoyancy causes bubble detachment. For the bubbles generated by the bubble breaker, the initial bubble exiting the pore channel is limited in size by the pore dimension, as discussed previously. Throughout the entire range of GLR, it was observed that the size of the bubbles exiting the bubble breaker were relatively constant and of the same size as the pore spacing. Even at the highest GLR, small bubbles were generated by the bubble breaker. The increase in mean bubble size in the measurement area (up to 80mm downstream of the bubble breaker outlet) is due to the coalescence of the bubbles downstream of the bubble breaker. As the GLR increases, the chance of coalescence between multiple bubbles increases leading to larger bubble formation. The increase in the mean bubble size is caused by the increase in number of large coalesced bubbles rather than the increase in size of each individual bubble leaving the bubble breaker. This effect can be seen from the bubble size distribution at varying GLRs. Figure 2.8 shows the size distribution of bubbles generated by a bubble breaker with a pore size of $S=2\text{mm}$ at three GLRs.

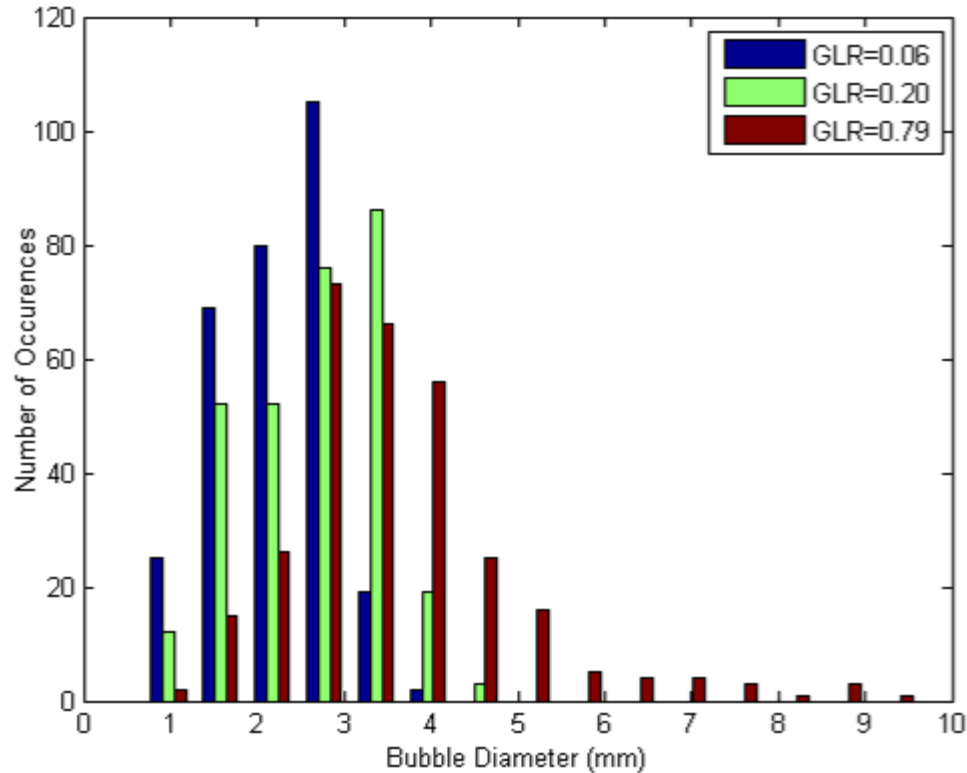


Figure 2.8: The size distribution of bubbles generated by a bubble breaker with a pore size of $S=2\text{mm}$ for three gas-liquid flow ratios.

The size distribution of bubbles generated by the bubble breaker in Figure 2.8 shows the effect of bubble coalescence. As observed in the figure, the bubble size distribution at the lowest GLR is quite narrow with a peak bubble size between 2-3mm. However, as the GLR increases, the bubble size distribution peak shows a slight increasing trend but the distribution tail extends significantly and monotonically with the GLR. This extension of the distribution tail towards the larger bubble size indicates the coalescence of two or more bubbles after the gas phase has exited from the bubble breaker. Although the peak bubble size remains nearly the same, the shift in distribution increases the mean bubble size. While the process is different, the trend of increased bubble size with increased GLR is similar for both nozzle-generated and bubble breaker generated bubbles.

The results in Figures 2.7 and 2.8 show systematic trends of mean bubble diameter with respect to GLR and the bubble breaker pore size. This suggests that a generalized trend can be obtained to represent the bubble diameter in dimensionless form.

Sada et al. [18] proposed that the bubble size in an unbounded two-phase (air and water) cocurrent vertical flow could be predicted by modified Froude number (see Equation 5), that represents the ratio of the gas inertia, and the drag and buoyant forces acting on the spherical bubble.

$$Fr = \frac{u^2}{gd_b + 0.33U^2} \quad (5)$$

where u represents the velocity of the gas in the nozzle and U represents the velocity of the liquid phase. They proposed a correlation to predict the size of single bubbles detaching from the gas nozzle, which is presented below:

$$d_b/\delta = 1.55Fr^{0.2} \quad (6)$$

where δ is the inside diameter of the gas nozzle. The correlation of Sada et al. [18] was compared with the nozzle-generated bubble size in the present study to determine if the same correlation exists for a bounded vertical two-phase co-current flow. The results are presented in Figure 2.9 as Froude number versus d_b/δ . The correlation of Sada et al. [18] (presented in Equation 6 above) is also plotted for comparison.

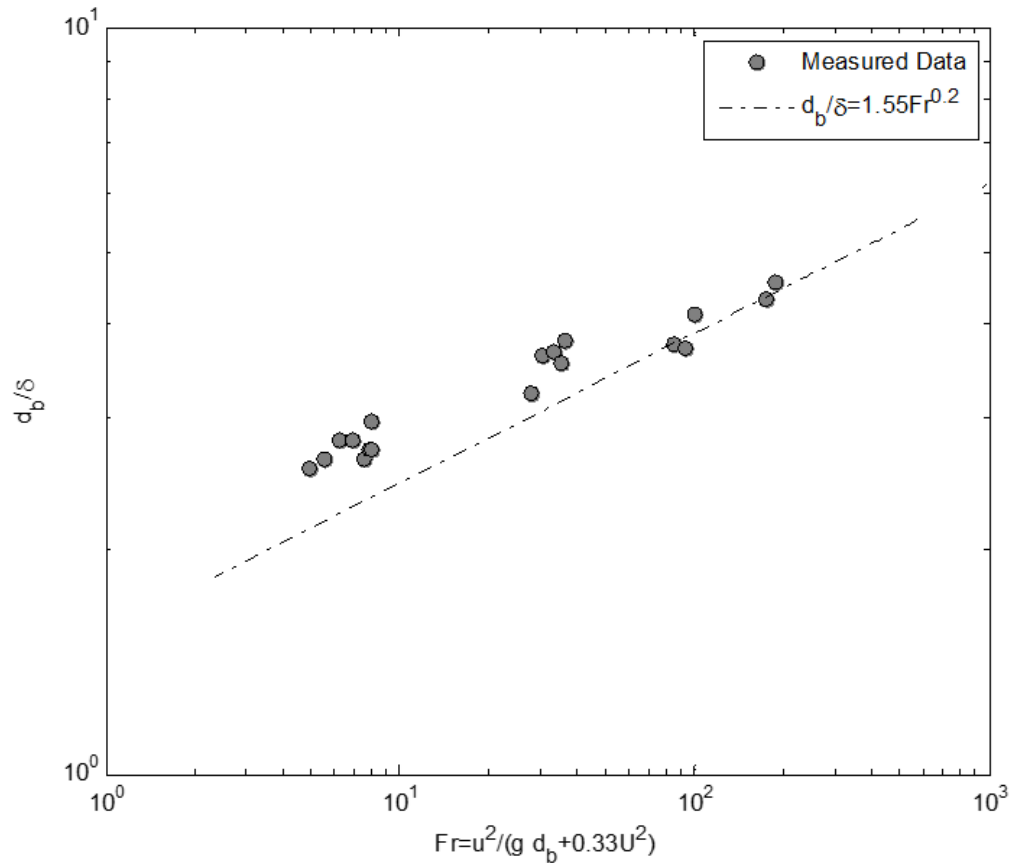


Figure 2.9: Froude number versus the normalized diameter of nozzle-generated bubble. The Froude number correlation proposed by Sada et al. [18] is plotted as the dashed line.

As Figure 2.9 shows, the present results agreed well with the correlation of Sada et al. [18] at higher Froude numbers ($Fr > 100$). However, as the Froude number decreased, the present results started to deviate from the Sada et al. [18] correlation. The plausible explanation for this deviation is that Sada et al. [18] neglected surface tension in their correlation based on the argument that the gas inertia is the dominant factor in bubble detachment. However, the gas inertia decreases with a decrease in the Froude number and hence, the surface tension becomes a significant factor in the bubble formation and detachment and thus, in controlling the bubble size at detachment. The above results indicate that at low Froude numbers, ignoring the effects of surface tension could underestimate the bubble size. Furthermore, another potential cause for the discrepancy is the difference in the experimental setups. Sada et al. [18] used an unbounded vertical

liquid flow whereas the flow in the present study was bounded by a cylindrical pipe. At lower Froude numbers where the liquid inertia was higher relative to the gas inertia, the liquid boundary layer developing on the pipe wall could have affected the detachment of the bubble from the nozzle. Nevertheless, the results in Figure 2.9 indicate that the correlation presented by Sada et al. [18] reasonably well predicts the nozzle-generated bubble size in bounded flow domains for $Fr > 1$.

For a mesh-type bubble breaker, the process of bubble generation is more complicated than that of a single bubble generated by a nozzle. The breakup of the initial nozzle-generated bubble by the bubble breaker is dependent on the gas and liquid inertia, the buoyancy of the bubble, the surface tension at the interface of the two phases, the pore size of the bubble breaker and the radius of curvature of the leading face of the bubble. Once inside the bubble breaker, much like a two-phase flow in a microchannel, the surface tension, local gas and liquid inertia, and the pore spacing determines the flow regime and slug spacing. As the gas phase leaves the bubble breaker pores, much like a bubble forming at a nozzle in a two-phase cocurrent flow, the length of the gas segments within the pores, the local gas and liquid inertia and the surface tension determines the bubble size at the breaker exit. Immediately after and sometimes during the detachment phase from the bubble breaker, the individual bubbles may coalesce and form larger bubbles. The probability of coalescence increases with an increase in GLR, as observed during the current experiment. It is also dependent on the proximity of the bubble breaker pores. The bubble breaker with a pore size of $S=1\text{mm}$ was found to produce more coalescence within the measurement area. It was also observed that for the same pore size ($S=1\text{mm}$), most of the gas phase passed through only a limited number of pores located in the center of the bubble breaker. Since the smaller pore size also causes an elongated gas slug within the pore channel, numerous bubbles that extend beyond the limits of the pores are formed close to each other causing a high probability of coalescence.

To predict the bubble size generated by the mesh bubble breaker, the correlation of Sada et al. [18] cannot be used due to some of the scaling parameters used in the equation. The equation for Froude number presented by Sada et al. [18] (Equation 4 above), used the diameter of the generated bubbles as the length scale. As discussed above and also shown

in Figure 2.8, the characteristic length scale that influences the bubble size generated by the breaker is the pore size (S). Hence, for the bubble breaker, the length scale used in Froude number scaling has been changed to the pore size. The other variables, u and U , representing the gas and liquid inertia are still characterizing parameters for the bubble formation by the breaker and hence necessary in the equation. For the bubble breaker correlation, u and U will represent the superficial gas and liquid velocities respectively. The modified Froude number scaling is given as,

$$Fr = \frac{u^2}{gS + 0.33U^2} \quad (7)$$

The other dimensionless parameter used by Sada et al. [18] as given in Equation (6), is the ratio of the bubble size and the internal nozzle diameter, which characterizes the bubble shape. For a mesh-type bubble breaker, various length scales are involved in the bubble shape factor, which are the bubble diameter, pore size and bounding pipe diameter. The pore size can be used to describe the initial bubble diameter leaving the bubble breaker and the pipe diameter can influence the probability of coalescence. Another important variable is the pore density (number of pores per unit area, pd), which relates the pore proximity to the occurrence of coalescence. As mentioned earlier, the close proximity of pores of the bubble breaker leads to the higher occurrence of bubble coalescence downstream of the bubble breaker when compared to the larger pore sizes. Hence, the shape factor (sf) is defined as,

$$sf = \frac{d_b D_i}{S \sqrt{pd}} \quad (8)$$

Equations (7) and (8) combine the properties of both bounded two-phase co-current flow and two-phase flow through a pore. The bubble size data for all given pore sizes over the range of gas and liquid flow rates, in non-dimensional form using the proposed new scaling in Equations (7) and (8), is plotted in Figure 2.10.

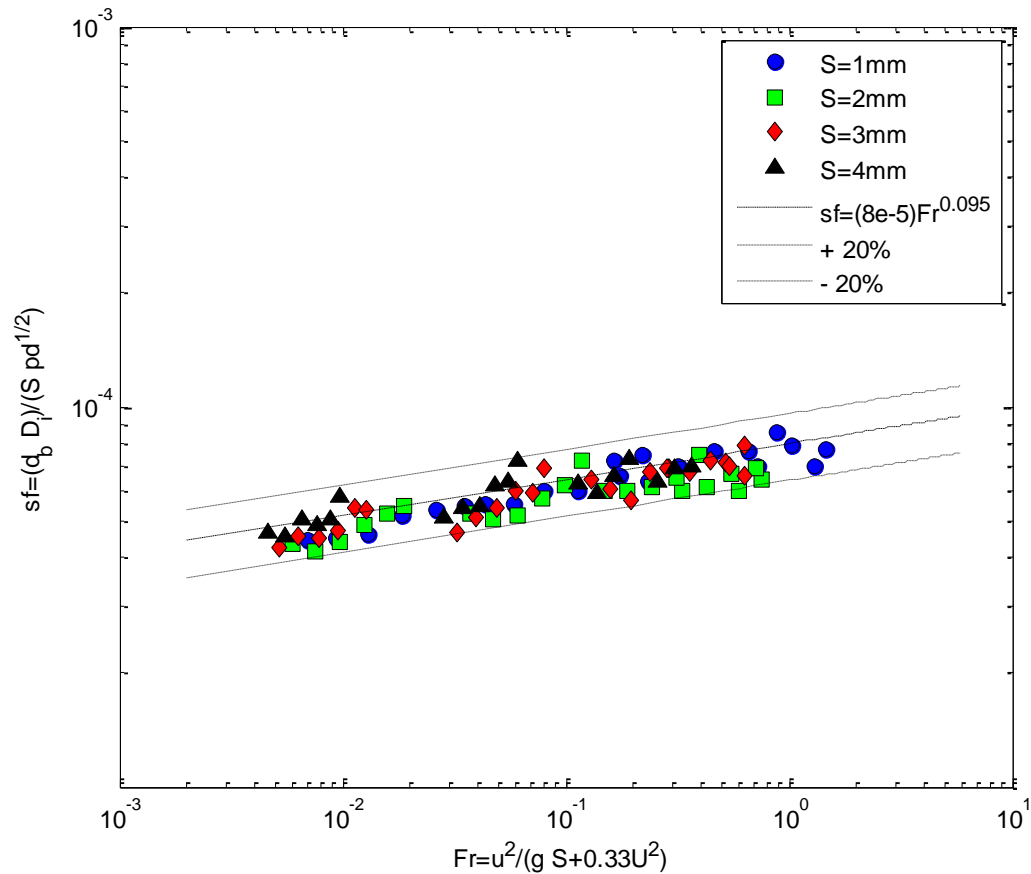


Figure 2.10: Modified shape factors plotted versus the modified Froude for all cases. The best-fit equation and $\pm 20\%$ confidence limits are also plotted.

The results in Figure 2.10 show that the bubble size data for different pore sizes collapsed within a narrow band confirming that the modified dimensionless shape factor and Froude number accurately characterize the size of bubbles formed by the mesh-type bubble breaker independent of the pore size in the given measurement range. The data in Figure 2.10 also shows strong correlation between the shape factor and the Froude number. The correlation is quantified through the best-fit curve expressed as Equation 9. All of the data points fit within $\pm 20\%$ of the values predicted by this correlation as indicated by the confidence limits on Figure 2.10.

$$sf = (8 \times 10^{-5})Fr^{0.095} \quad (9)$$

It is also observed that the bubble size in the present correlation has relatively weaker dependency on the Froude number as compared to the correlation of Sada et al. [18] (Equation 5). This is due to the reason that the initial bubble size leaving the bubble breaker is limited by the pore size and the eventual increase in mean bubble size is due mainly to the bubble coalescence. Hence, the rate of bubble growth is much smaller than that of a single bubble generated by a nozzle. The individual bubbles that coalesce will have larger size compared to the mean bubble size, but as shown in Figure 2.7, the coalesced bubbles are at the tail end of the distribution and have a relatively weak influence on the mean bubble size.

The correlation in Equation 9 is obtained from the bubble data for different pore sizes over a range of gas and liquid flow rates. However, the bubble breaker length (L) as well as its distance from the nozzle (H) were constant. The correlation was further tested for its ability to predict the size of bubbles generated from a bubble breaker with a constant pore size but different length and position. Figure 2.12 shows the data for bubble breakers of pore size $S=2\text{mm}$, lengths of $L/D_{bb}=1$ and 2, and heights of $H=13\text{mm}$ and 25mm. The plot shows that the data collapsed in a narrow band and follow the proposed correlation closely, confirming that the proposed correlation accurately captures the effect of the breaker's length and position. Like the data plotted in Figure 2.10, the data plotted in Figure 2.11 fits within $\pm 20\%$ of the values predicted by the correlation shown as Equation 9.

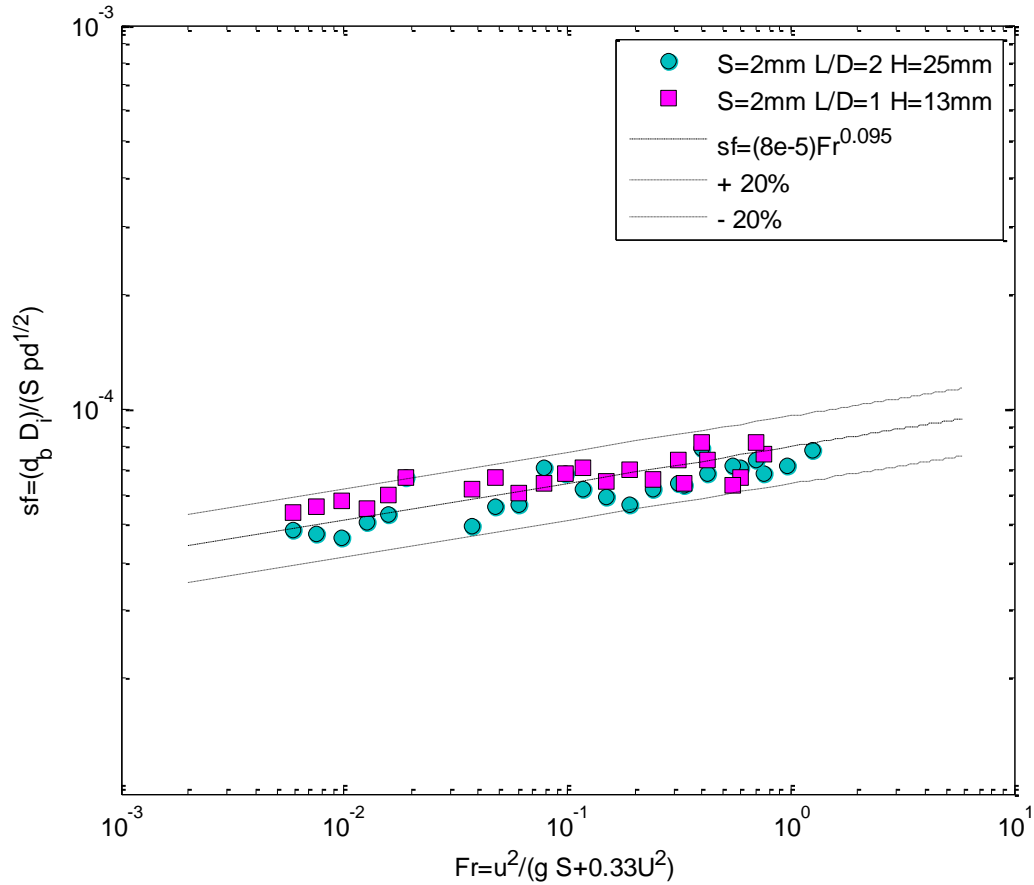


Figure 2.11: Modified shape factors plotted versus the modified Froude number for different lengths and positions of the bubble breaker of 2 mm pore size. The correlation from Equation 9 is also plotted for comparison.

It is important to note that the proposed correlation is valid when bubbly flow is present after the bubble breaker. The range of liquid and gas flowrates that produce bubbly flow may differ when the bubble breaker configuration is changed. The Froude number prediction is also limited to air and water. Similar to Sada et al. [18], the proposed correlation ignores the surface tension effects at the phase interface. Surface tension can affect the flow through the bubble breaker pores, the detachment of the gas phase from the bubble breaker and the probability of coalescence or further bubble breakup downstream of the bubble breaker.

2.4.2 Flow Regime Characterization

The flow regime in a bubble column reactor can have a large impact on both the heat and mass transfer rates. Knowledge of the flow regime under the given operating conditions, will allow designers to properly size reactor columns for their desired applications. As shown in the previous section, the mesh-type bubble breaker is effective in reducing the bubble size in a bubbly flow regime. In the current section, the influence of mesh-type bubble breakers on the flow regime transition over the given range of GLRs is presented and discussed.

The images from the high-speed camera were used to identify a specific flow regime for each combination of flow and bubble breaker geometric variables. These flow regimes varied from bubbly to churn flow. As per Hewitt [21], and Hewitt and Roberts [22], bubbly flow is defined as separate spherical regions of gas dispersed throughout the liquid. Whereas, slug flow is defined as large elongated regions of gas separated by slugs of liquid flow. The gas phase fills the majority of the cross sectional area of the tube and is surrounded by a thin layer of liquid that separates the gas from the tube wall. Churn flow is defined as an unstable and oscillatory flow that occurs when slug regions begin to coalesce and form gas columns [21, 22]. Images illustrating these flow regimes with and without a bubble breaker are shown in Figures 2.12 and 2.13, respectively.

When no bubble breaker was present, as shown in Figure 2.12, the gas phase quickly coalesced and formed slug and churn flow. Even at the highest liquid flow rates, the flow transitioned from bubbly to slug flow at a relatively low gas flow rate. When a bubble breaker was added, as shown in Figure 2.13, the bubbles generated by the nozzle were effectively broken up into smaller and more dispersed bubbles. As the gas flow rate increased, the bubble breaker prevented the gas from transitioning into a slug flow at the same flow conditions at which the bubbly flow transitioned to the slug flow in the absence of a bubble breaker. Eventually, in most cases, the flow with a bubble breaker did reach slug and then churn flow in the upper range of the gas flowrates used in the present study.

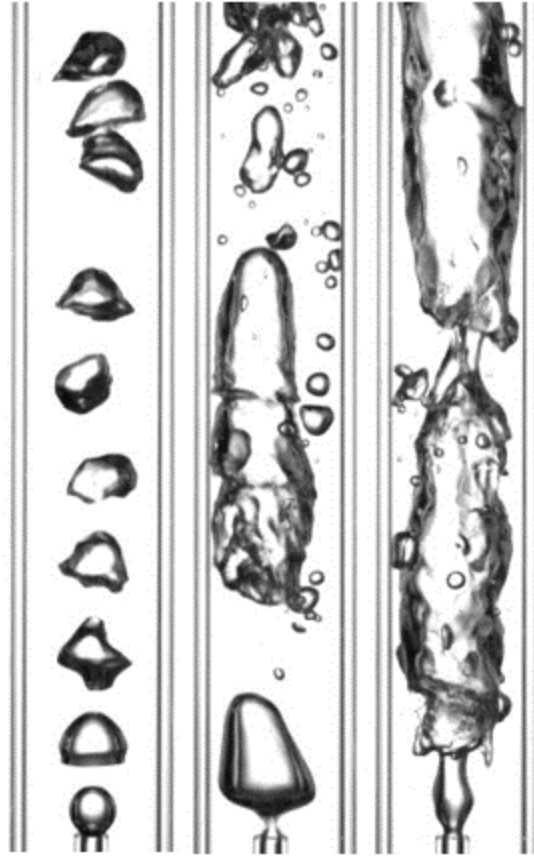


Figure 2.12: Images of Two-Phase flow with no bubble breaker. From left to right the images show bubbly flow ($Q_L=0.63$ LPM, $Q_G=0.2$ LPM, $GLR=0.32$), slug flow ($Q_L=0.63$ LPM, $Q_G=1.0$ LPM, $GLR=1.59$), and churn flow ($Q_L=0.63$ LPM, $Q_G=2.0$ LPM, $GLR=3.17$).

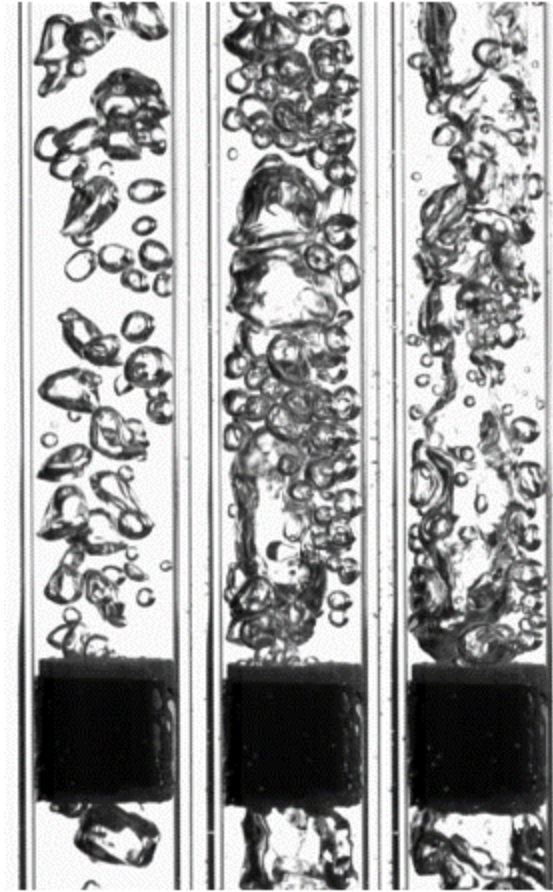


Figure 2.13: Images of Two-Phase flow after passing through a bubble breaker ($S=2\text{mm}$, $H=25\text{mm}$, $L/D_{\text{bb}}=1$). From left to right the images show bubbly flow ($Q_L=0.63$ LPM, $Q_G=0.5$ LPM, $\text{GLR}=0.79$), slug flow ($Q_L=0.63$ LPM, $Q_G=1.5$ LPM, $\text{GLR}=2.38$), and churn flow ($Q_L=0.63$ LPM, $Q_G=2.5$ LPM, $\text{GLR}=3.97$).

When slug and churn flow form in the presence of a bubble breaker, the surface area to volume ratio of the gas phase was higher compared to the slug and churn flow generated by the nozzle. The bubble breaker first breaks the slug and churn flow into individual small bubbles. For slug or churn flow to reform, the small bubbles exiting the bubble breaker pores must coalesce. Although a large number of small bubbles and gas regions coalesce, there remain significant number of detached small gas regions (see Figure 2.13). These small and numerous gas regions increase the surface area to volume ratio of the gas phase compared to that in the absence of a breaker. The images also show that in the presence of a bubble breaker, generally, for slug flow, each gas slug region produced

by the bubble breaker is followed by a liquid section containing small bubbles. Whereas in churn flow, the diameter of the center column of gas is reduced as small bubbles remain close to the pipe wall (see Figure 2.13).

To quantify the effect of various geometric parameters of the mesh-type bubble breaker on the flow transition, the high-speed images were used to generate flow transitional charts that map flow regimes as a function of operating conditions [21]. In the present study, the charts are produced based on the observed flow regimes from the imaging data covering 80 mm height from the bubble breaker or the nozzle (in the absence of a bubble breaker). Figure 2.14 shows the flow transitional chart in the absence of a bubble breaker over the given range of gas and liquid flow rates.

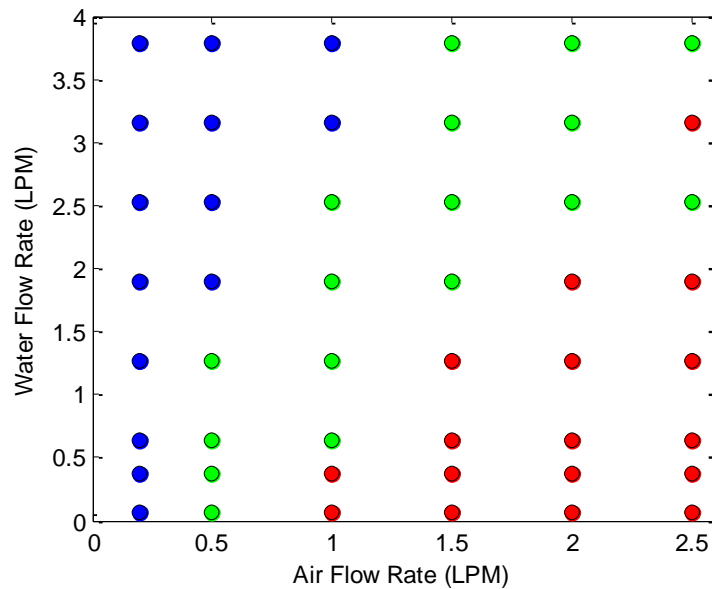


Figure 2.14: Flow transition chart for cases without a bubble breaker over a range of air and water flow rates. The coloured symbols depict each flow regime (blue=bubble, green=slug, red=churn).

As Figure 2.14 shows, the transition from bubbly to slug flow occurs at the lower end of gas flow rates used in this study. For the lower range of liquid flow rates, only a gas flow rate of 0.2 LPM was able to produce bubbly flow. For the two highest liquid flow rates (3.15 LPM and 3.79 LPM), bubbly flow was observed up to a gas flow rate of 1 LPM. For liquid flowrates of 1 LPM and above the observed bubble to slug transition GLR remained constant at $GLR \approx 0.3$. At liquid flowrates lower than 1 LPM, the bubble-to-slug transition GLR increases as the liquid flowrates decrease. The observed transition GLRs for liquid flowrates of 0.63 LPM, 0.38 LPM and 0.06 LPM are ~ 0.55 , ~ 0.92 and ~ 5.0 , respectively. At low liquid flowrates, the bubble formation and breakoff from the nozzle, and eventual coalescence is driven by the buoyancy forces rather than the inertia of the liquid phase. The low liquid flowrate causes the gas phase to behave as if it was in a stagnant bounded water column. The changes in liquid flowrate have negligible effect on the change in flow type. Once the liquid flowrate is high enough, the inertial forces begin to influence the bubble behaviour allowing the GLR to be used as a predictor of the flow transition.

The results in Figure 2.14 for a two-phase vertical co-current flow with no bubble breaker will be used as a baseline to compare the influence of mesh-type bubble breaker geometry on the flow regime transition. The first geometry variable to be discussed is the pore size. The transition charts for bubble breakers with different pore sizes are shown in Figure 2.15. When comparing the transition charts in Figure 2.15 with that in Figure 2.14, it can be seen that a mesh-type bubble breaker, of any pore size, is effective in increasing the GLR range over which bubbly flow is present. For example, at a pore size of $S=2\text{mm}$, the bubble to slug transition GLR is increased to $GLR \approx 0.8$ at a liquid flowrate of $Q_L=2.5\text{LPM}$.

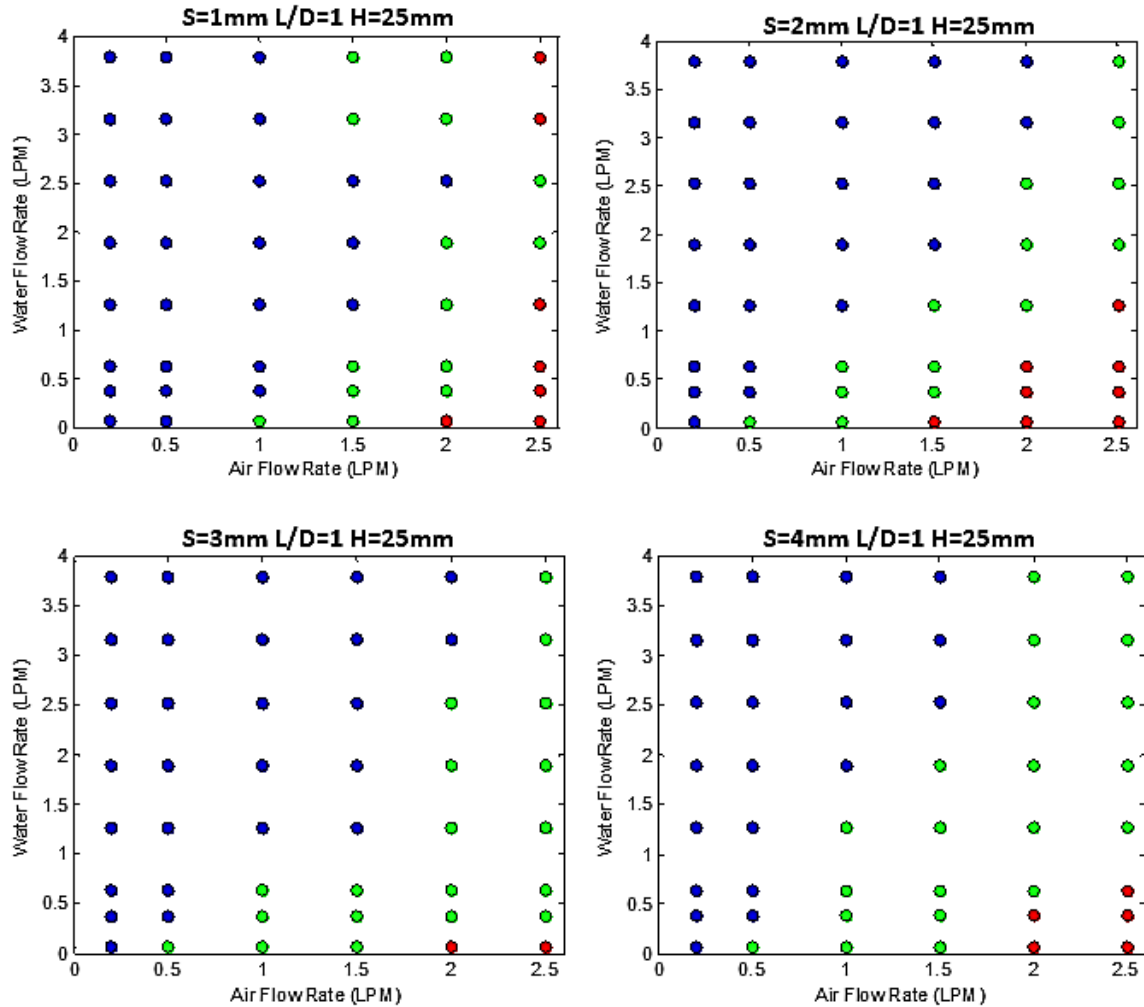


Figure 2.15: Flow transition charts for the cases with bubble breakers of different pore sizes (1-4 mm). The length of the bubble breaker and the height above the nozzle remain constant at $L/D_{bb}=1$ and $H=25\text{mm}$, respectively.

Differences between the flow regime transitions can be seen when comparing the transition charts of four different pore sizes. In general, the GLR at which transition from bubbly flow to slug flow occurs decreases as the pore size increases. This is due to the increased bubble size caused by the pore spacing. The bubbles detaching from the 4mm pore size breaker will be larger than the bubbles from the 1mm pore size breaker. If the bubbles from the larger pore size breaker coalesce, they will be more likely to form a bubble large enough to be considered as a slug region. For the bubbles from a smaller pore size breaker, it will take more interactions of multiple bubbles to form a slug region.

A contrast to the general trend is seen in the flow transition chart of the bubble breaker with a pore size of $S=1\text{mm}$. For liquid flowrates up to $Q_L=2.5\text{LPM}$, the bubble breaker was effective in increasing the GLR at which the flow transitioned from bubbly to slug regime. For these liquid flowrates, the $S=1\text{mm}$ bubble breaker allowed for the highest GLR for transition from bubbly to slug flow. At $Q_L=2.5\text{LPM}$, the transition from bubbly flow to slug flow occurred at $\text{GLR}\approx 1$. However, for the liquid flow rates above 2.5LPM , the bubble breaker was not able to increase the transition GLR when compared to a flow in the absence of a bubble breaker. For instance, at $Q_L=3.8\text{LPM}$ the transition from bubbly flow to slug flow occurred at $\text{GLR}\approx 0.4$, which is lower than the no bubble breaker case. By analyzing the images captured by the high-speed camera, it was observed that at higher liquid flow rates, the $S=1\text{ mm}$ bubble breaker was not able to disperse smaller gas regions throughout the entire cross section and slug regions started to form almost immediately after the gas phase left bubble breaker (see Figure 2.16).

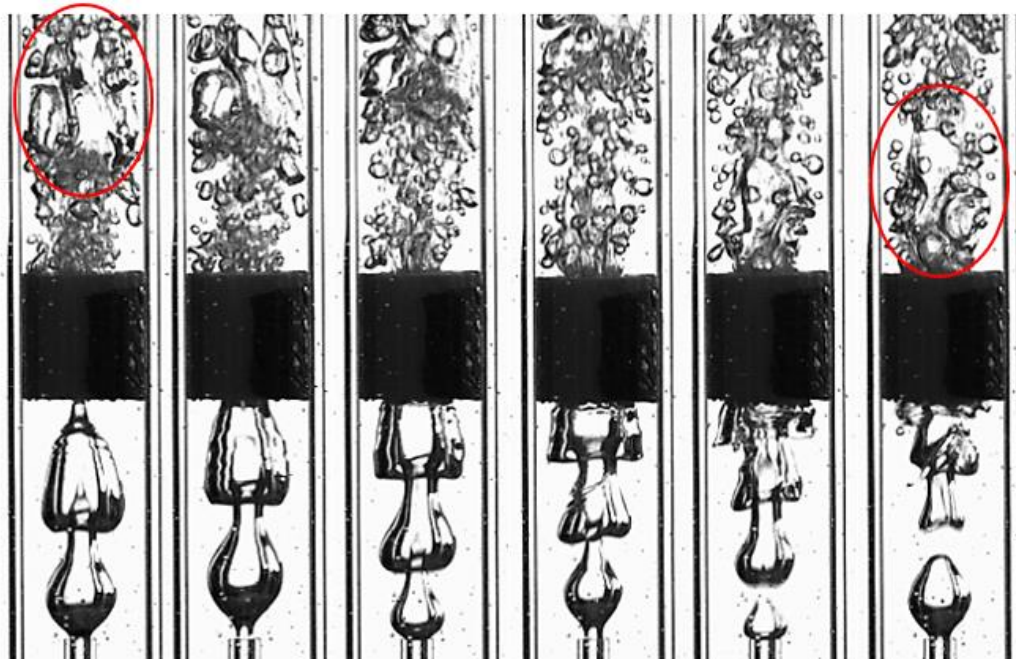


Figure 2.16: Image sequence showing the slug formation downstream of a bubble breaker with a pore size of $S=1\text{mm}$ at a liquid flowrate of $Q_L=3.2\text{LPM}$ and a gas flowrate of $Q_G=1.5\text{LPM}$ ($\text{GLR}=0.47$). The time interval between images is 0.005 seconds. The gas slug regions are highlighted by red outlines.

The process of slug formation downstream of the bubble breaker begins with the entrance of gas into the bubble breaker pores. The pore structure of a bubble breaker can be considered as a mechanism to introduce shearing force on the bubbles passing through the breaker, which may be similar to a shearing force caused by turbulent eddies. For bubble breakup in turbulent flow, the Weber number has been used to determine the critical size of a bubble to trigger breakup [30]. This critical Weber number is expressed as,

$$We = \frac{\overline{V_b^2} d_b \rho_L}{\sigma} \quad (9)$$

where the velocity scale, V_b^2 , of the Weber number is defined as the average value across the flow field of the squares of velocity differences over a distance equal to the bubble diameter, ρ_L is the liquid density and σ is the surface tension of the bubble. The length scale, d_b , is the diameter for a spherical droplet or bubble, and for a non-spherical bubble or droplet, it refers to the local radius of curvature at the phase interface. In order for a bubble to break, the Weber number must be greater than the critical Weber number for the given flow conditions [30].

To increase the probability of bubble breakup in a turbulent flow, the integral length scale of the turbulent structures must be of the same size as the generated bubbles. This ensures that a larger enough shearing velocity difference will be generated across the bubble surface [30]. Even if a large shearing velocity difference is formed by a small eddie, it may not be enough to break the bubble surface. Small eddies tend to cause disturbances on the bubble as the inertia contained in the eddie is not enough to overcome the bubble surface tension. If an eddie is much larger than a bubble, the shearing velocity difference will be small at a distance equal to the bubble diameter. Large eddies cause the entire bubble to be translated rather than causing a break [30]. For break up caused by a bubble breaker, the pore walls cause a shearing stress and the pore spacing can be thought of as the shear spacing, similar to the eddie size. Decreasing the pore size can decrease the Weber number.

A factor that influences the Weber number, when it is used to describe the break up of a bubble caused by a bubble breaker, is the radius of curvature at the leading edge of the nozzle-generated bubble. It has been observed that nozzle-generated bubbles, at high liquid flowrates, undergo stretching near the leading edge as they advect downstream, which reduces the leading edge radius of curvature. The image sequence in Figure 2.16 illustrates this phenomenon. The process of the bubble tip forming in a flow unobstructed by a bubble breaker is illustrated by an image sequence in Figure 2.17. At high liquid flowrates, the liquid inertia elongates the bubble as it is forming at the nozzle tip. Right before the detachment from the nozzle, as the lower portion of the bubble stretches, a neck is formed at the lower end of the bubble that maintains the supply of gas into the bubble from the nozzle. Once the bubble detaches, the neck rebounds and pushes the air mass upwards into the bulk of the bubble. This upward push of mass causes the deformation of the leading edge, which then leads to the tip formation (see Figure 2.17).

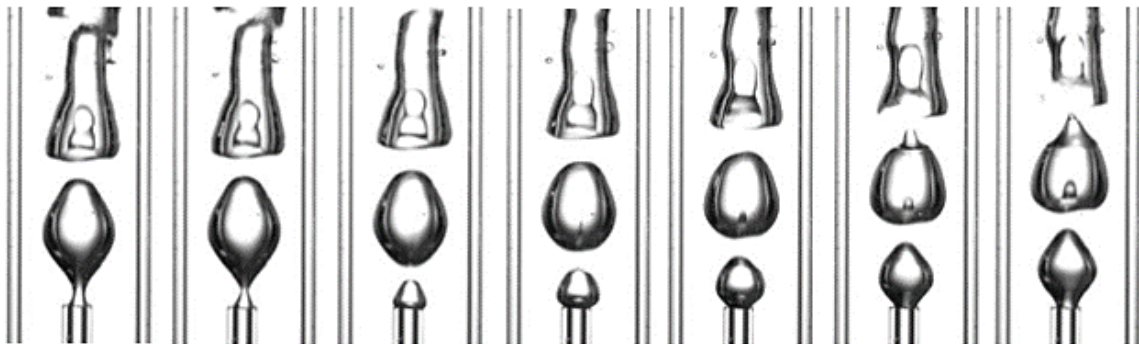


Figure 2.17: An image sequence, illustrating the formation of a tip at the leading edge of a nozzle-generated bubble at liquid and gas flowrates of $Q_L=3.2\text{LPM}$ and $Q_G=1.5\text{LPM}$ ($\text{GLR}=0.47$). The time separation between images is 0.003 seconds.

Since the leading edge tip of the bubble is the first point of contact with the bubble breaker, its curvature plays a crucial role in the bubble breakup and the dispersion of airflow into the bubble breaker pores. Figure 2.18 depicts a conceptual model of the bubble breakup process for smaller pore size at higher GLRs due to the presence of bubble's leading edge.

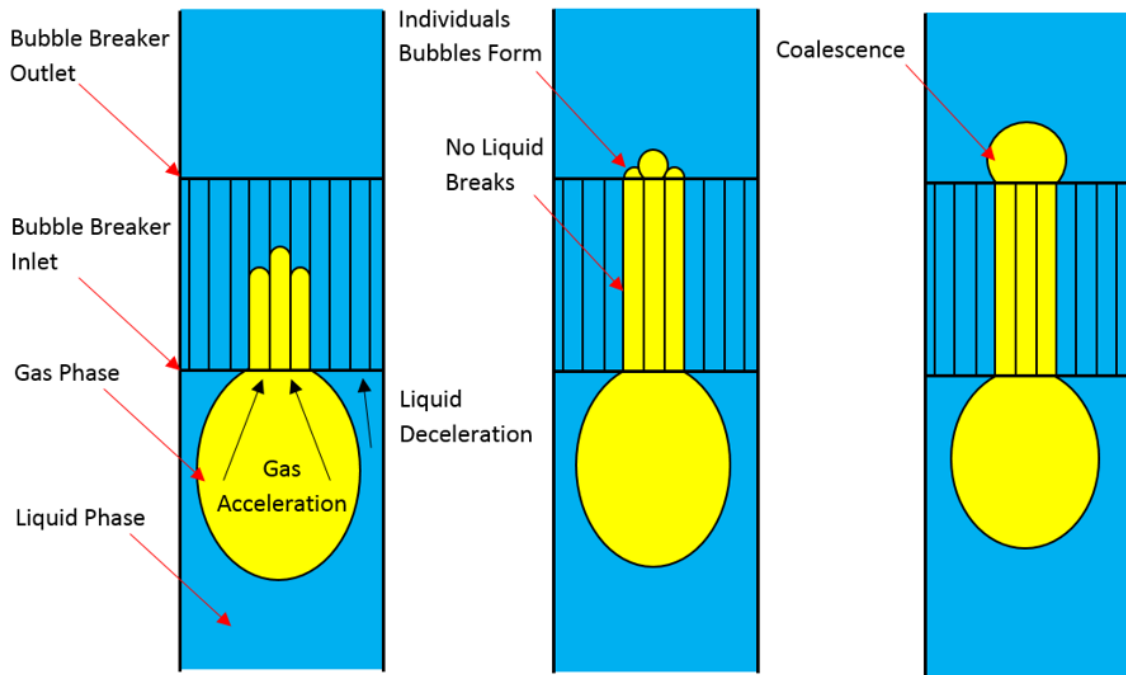


Figure 2.18: An image showing the flow of a gas region through a bubble breaker that is unable to split the bubble into multiple pores due to the bubble tip formed after detaching from the nozzle.

As the radius of curvature of bubble's leading edge becomes smaller, the bubble is exposed to a smaller number of pores in the centre of the breaker. The pores' edge causes the rupture of the interface and the air from the bubble starts to flow through these pores. Since the cross-sectional area of gas flow in the breaker becomes smaller than that of the bubble itself, the gas accelerates as it enters the breaker pores. The liquid passes through the rest of the breaker pores. The reduction in the gas flow area at the bubble breaker entrance results in an increase in the liquid flow area, which leads to the deceleration of the liquid as it enters the breaker pores (see Figure 2.18). At the breaker exit, gas moves faster than the liquid causing a rapid expansion of the gas, which increases the probability of bubble coalescence and the reformation of slug bubbles at smaller pore size (see Figure 2.18). The images in Figure 2.16 confirm this behaviour.

Although the reduction in Weber number due to the reduced radius of curvature occurs for each of the bubble breakers tested, a small pore size provided an additional contribution to the reduction in the Weber number to allow the slug region reforming. It is expected that if the pore size is reduced further, the bubble breaker will not be able to increase the GLR at which the flow transitions from bubbly to slug regime at even lower liquid flowrates than those observed for the $S=1\text{mm}$ bubble breaker. Eventually, the pore size can be reduced enough that it will have no effect on the transition GLR when compared to a flow with no bubble breaker.

The influence of bubble breaker's distance from the nozzle tip on the flow transitional behavior is presented in Figure 2.19 for two different pore sizes. Once again, all bubble breakers were able to increase the GLR at which the flow transitioned from bubbly to slug or churn when compared to the case with no bubble breaker. The placement of the bubble breaker did have an effect on the transition GLR; placing the bubble breaker further downstream from the nozzle tended to decrease the transition GLR.

When comparing the flow transition charts for bubble breakers with a pore size $S=2\text{mm}$ at heights of $H=13\text{mm}$ and $H=50\text{mm}$ above the nozzle, it can be seen that the bubble breaker that is closer to the nozzle tip is more effective in delaying the transition of bubbly flow to slug flow to higher GLRs as well as the transition from slug to churn flow. At a liquid flowrate of $Q_L=2.5\text{LPM}$, transition from bubbly to slug flow occurred at $\text{GLR}=0.8$ at a height of $H=13\text{mm}$, which reduces to $\text{GLR}=0.6$ for a height of $H=50\text{mm}$. At the same liquid flowrate, the bubble breaker at a height of $H=13\text{mm}$ was able to completely prevent churn flow from occurring whereas the transition occurred at a $\text{GLR}=0.8$ when the bubble breaker was at a height of $H=50\text{mm}$. The analysis of the data also shows that the change in transitional GLR is not significant if the bubble breaker is moved to a lesser distance above the nozzle. For example, the difference in transitional GLR is minimal when the bubble breaker moved from a distance of 13 mm to 25 mm away from the nozzle (see Figure 2.15). A height of $H=50\text{mm}$ allows for gas regions that detach from the nozzle as single bubbles to form into slugs before coming into contact with the bubble breaker. Once a slug region has formed, the bubble breaker becomes less effective as there will be less mixing between the gas and liquid phase within the pore

channels. Since a slug region could be longer than the bubble breaker length, the gas region passing through a pore channel may fill the entire length of the pore with gas without letting any liquid in. With no liquid in the pore, the gas region will not break into multiple bubbles and the gas will exit the bubble breaker pores as elongated jets rather than bubbles. The gas jets emerging from bubble breaker pores interact with each other to reform a slug region. By placing the bubble breaker closer to the nozzle, the flow regime between the bubble breaker and nozzle tip remains bubbly at higher GLRs. Once at an optimal height, any further decrease in the height of the bubble breaker will have little to no effect on the flow regime transition.

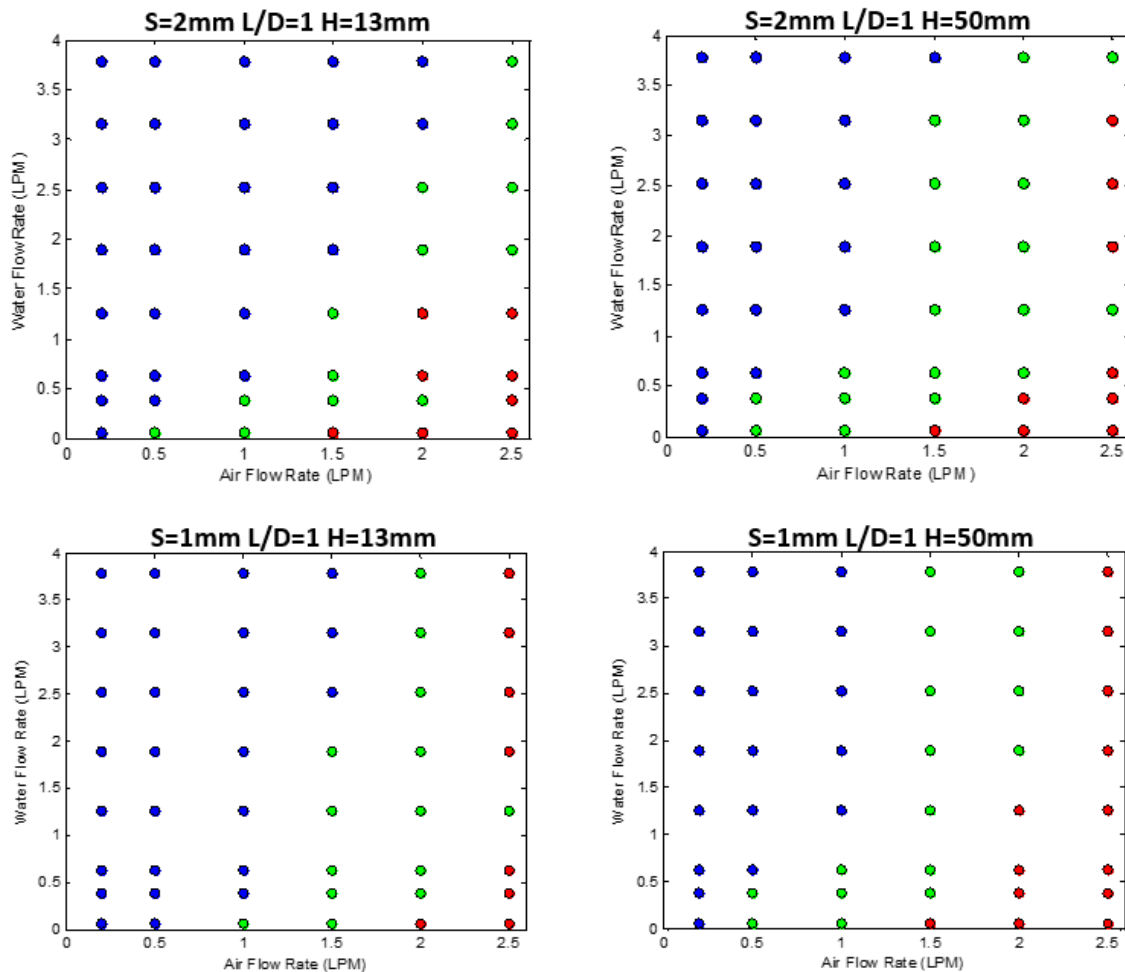


Figure 2.19: Flow transition charts for the cases with bubble breakers at two different positions above the nozzle tip for two different pore sizes.

The flow charts for the bubble breaker with a pore size of $S=1\text{mm}$ and heights of $H=13\text{mm}$ and $H=50\text{mm}$ (see Figure 2.19) can be compared to the flow chart for the bubble breaker with the same pore size and a height of $H=25\text{mm}$ (see Figure 2.15). As discussed earlier, this pore size was very effective at increasing the transition GLR for liquid flowrates up to $Q_L=2.5\text{ LPM}$. Due to a decrease in Weber number, the pore size did not increase the transition GLR for liquid flowrates above $Q_L=2.5\text{ LPM}$ compared to the flow with no bubble breaker. A similar trend can be seen when the bubble breaker was lowered to a height of $H=13\text{mm}$ and raised to a height of $H=50\text{mm}$. At liquid flowrates up to $Q_L=2.5\text{ LPM}$ the transition GLR from a bubbly to slug flow regime was higher than or equal to a bubble breaker at the same height and a pore size of $S=2\text{mm}$ (with the exception of a liquid flowrate $Q_L=2.0\text{ LPM}$). Above the liquid flowrate of $Q_L=2.5\text{ LPM}$, the transition GLR for the bubble breaker with a pore size of $S=1\text{mm}$ and height of $H=13\text{mm}$ becomes less than the transition flowrate of the bubble breaker with a pore size of $S=2\text{mm}$ and the same height. The same trend occurs when the bubble is at a height of $H=50\text{mm}$. The transition GLR is still higher when the bubble breaker is compared to a flow with no bubble breaker case. By moving the bubble breaker closer to the nozzle tip, the bubbles will come in contact with the bubble breaker before the bubble tip, is formed (see Figure 2.18). Moving the bubble breaker further downstream of the nozzle allows the bubbles to reform into a more spherical shape after the tip is formed. The radius of curvature of the leading edge of the bubbles as they come into contact with the bubble breaker is increased allowing the bubbles to break into more pores, reducing the chance of coalescence immediately downstream of the bubble breaker. At the two highest gas flow rates tested in this study, the increase in radius of curvature is still not large enough to overcome the effect of the small pore size and the gas reforms into slug flow after passing through the bubble breaker.

The influence of the bubble breaker length on the flow transition is illustrated in Figure 2.20. The bubble breaker length was found to have a significant influence on the bubble to slug transition GLR. The bubble breaker with a length of $L/D_{bb}=2$ was able to completely eliminated slug and churn flow when the liquid flowrate was $Q_L=3.79\text{ LPM}$.

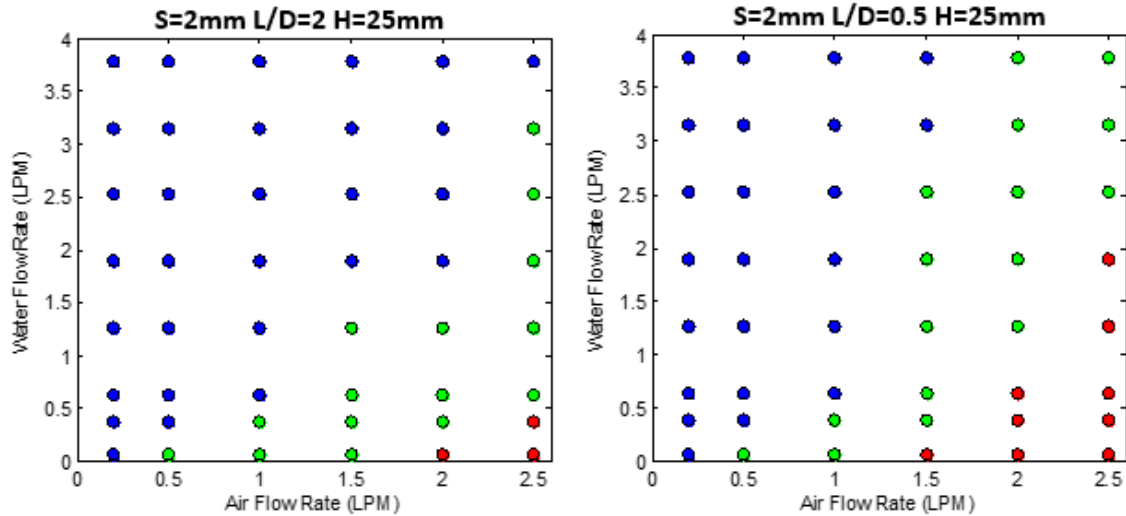


Figure 2.20: Flow transition charts for bubble breakers with two different lengths.

The results in Figure 2.20 indicate that the change in length of the bubble breaker greatly influences the bubble to slug and slug to churn transitions. The results show that by reducing the length of the bubble breaker, the transitional GLR was decreased for each liquid flowrate over the given range of gas flow rates. The inlet Weber number remains the same due to the same pore size and bubble breaker position for these two cases. Hence, it is expected that the gas regions should be broken into the same number of pores for each bubble breaker. The significant difference at the breaker outlet indicates that the length of the bubble breaker pores controls the mixing between the gas and liquid regions occur before the flow exits the bubble breaker.

As the flow through a pore in the bubble breaker is similar to that in a microchannel, the two-phase flow inside the pore can be explained based on the previous investigations of two-phase flows in microchannels. Yue et al. [45], through imaging, found that at the entrance of a T-junction microchannel, a region was formed in which the gas and liquid flowed side by side and created an elongated gas column. At the end of this region, the gas column was broken into a single slug, which filled the entire cross-sectional area of the channel, as it is squeezed by the surrounding liquid flow. Downstream of the entrance region, the gas slugs were evenly separated by regions of pure liquid. They found that the

entrance length of the microchannel could be up to five times the diameter of the channel and that the entrance length increases with increasing GLR.

When the bubble breaker length is reduced, the entrance region described above may extend beyond the physical length of the bubble breaker. If the bubble breaker is not long enough for the separate slug regions of gas to form within the channel, a continuous gas flow will emerge from the breaker exit without liquid separation. That is, the gas can pass through the entire length of the bubble breaker with no breakage and exit as a column. The gas columns from multiple pores expand upon exiting the pores and coalesce to reform a large bubble or slug region, reducing the transitional GLR. Figure 2.21 illustrates this process in the form of an image sequence when a bubble passes through a shorter bubble breaker ($L/D_{bb}=0.5$).

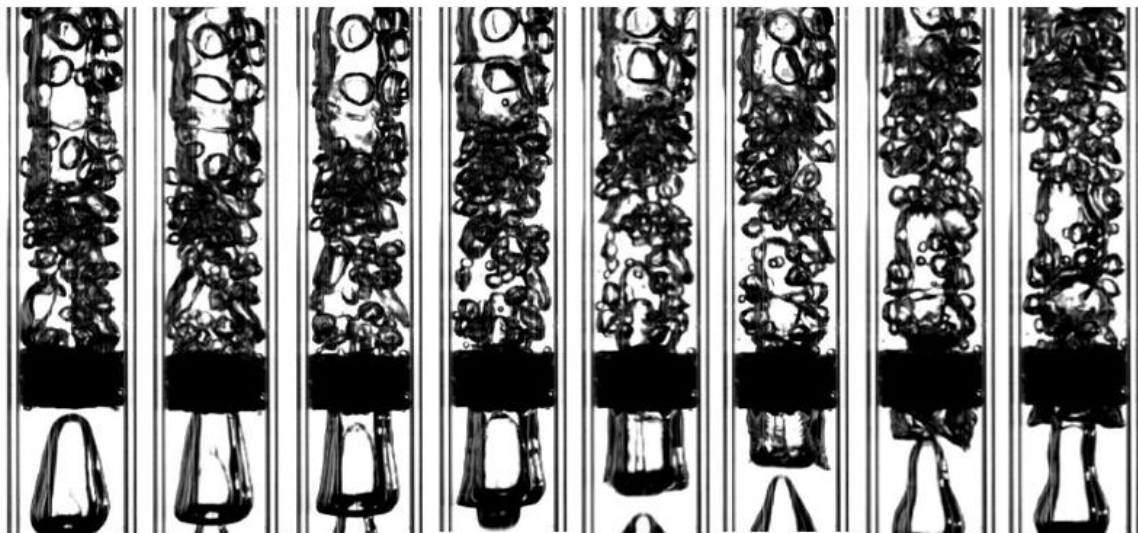


Figure 2.21: Slug formation of a gas region passing through a bubble breaker with a length of $L/D_{bb}=0.5$. Images are separated by 0.006 seconds.

In Figure 2.21, it can be seen that the nozzle generated gas region is almost unaffected by the bubble breaker with a length of $L/D_{bb}=0.5$. No mixing between the gas phase and liquid phase seems to have occurred within the pore channel as the gas region enters the bubble breaker. At the outlet of the bubble breaker, the gas regions expand and coalesce. Since the pore length is too short (pore length to spacing ratio of 3.75) to break up the gas region in the bubble breaker (i.e. the breaker length is smaller than the required entrance

length), a continuous flow of gas through the pore occurred. This is also evident in Figure 2.21, by comparing the shape profile of the bubble at the breaker inlet and the locations in the breaker exit plane where the gas flow emerged. To allow for mixing to occur between the gas and liquid phases, the pore channel must be longer than the microchannel entrance region. In general, it is observed that the bubble breaker should be longer than the gas slug region to effectively break it up. When the channel is longer than the entrance region, the gas regions separated by liquid slugs will leave the pores in the form of individual bubbles and will allow a dispersed bubbly flow to form after the bubble breaker. As seen in Figure 2.20, the bubble breaker with a length of $L/D_{bb}=2$ was the most effective bubble breaker tested in this study in terms of increasing the transition GLR for bubbly to slug flow. This is because even at high GLRs, the mixing between the gas and liquid phases can occur inside the pore channels.

The results presented earlier show that all bubble breakers were effective in delaying the transition from bubble to slug flow in two-phase vertical co-flow, indicating that they can be effective devices in designing efficient bubble column reactors. A design variable that was not tested in this paper was the pressure drop caused by the bubble breaker. The pressure drop could have an effect on the bubble breaker selection. Although smaller pore sizes and longer bubble breakers are found to be most effective at increasing the GLR at which the flow transitions from bubbly to slug flow, these features would also cause the largest pressure drop. For a single phase flow passing through a bubble breaker, the pressure drop can be approximated using Equations 10 and 11 [43],

$$\Delta P = f \frac{L \rho U^2}{S} \quad (10)$$

$$f = \frac{k}{Re_S} \quad (11)$$

where the Reynolds number of the liquid passing through a single pore is defined as,

$$Re_S = \frac{US}{\nu} \quad (12)$$

using the superficial velocity of the liquid in the pipe, U , as the velocity of the liquid passing through the pore. For a square pore, the friction factor, k , is assumed to be 56.92 [43]. For a bubble breaker with a pore size of $S=2\text{mm}$ and a length of $L=15\text{mm}$, the pressure drop of a water flow of $Q_L=3.8\text{LPM}$ ($Re_S=747$) is estimated as $\Delta P=40\text{Pa}$. The pressure loss is double to $\Delta P=80\text{Pa}$ for a bubble breaker with the same length and a pore size of $S=1\text{mm}$. These estimations are most likely low as they do not account for the losses due to the flow needing to split into the individual pores. It also does not account for the increased surface area of multiple pores. When a gas phase is added to the flow, it is expected that the pressure drop across the bubble breaker is increased as more energy is needed to overcome the surface tension of the gas-liquid interface to physically break split the gas phase into the pores. Further studies using bubble breakers in two-phase flows can be done to estimate the resulting pressure drop.

2.5 Conclusion

An experimental study was conducted to investigate the influence of a mesh-type bubble breaker in a two-phase vertical co-flow. The dynamics of the two-phase flow was characterized using high-speed imaging. The results have shown that a mesh-type bubble breaker is effective in reducing the size of a nozzle-generated bubbles in two-phase cocurrent vertical flow as well as delaying the transition from a bubbly to slug flow regime. By reducing the bubble size, the interfacial surface area between the gas and liquid phases of the flow is increased allowing for high rates of mass absorption in bubble column reactors.

For the bubbly flow regime, a Froude number correlation was proposed to predict the mean size of the bubbles downstream of the bubble breaker. The correlation was found to accurately predict the bubble size generated by bubble breakers with a variety of pore sizes, lengths and positions relative to the nozzle.

The geometry of the bubble breaker was shown to have an effect on the regime transition of the two-phase flow. At low liquid flow rates, $Q_L \leq 2.5\text{LPM}$, a bubble breaker with a pore size of $S=1\text{mm}$ was more effective in producing bubbly flow than bubble breakers with larger pore sizes. At higher liquid flow rates, the elongation of the bubbles by the

liquid inertia that causes a reduction in the bubble leading edge curvature reduced the effectiveness of the breaker with smaller pore size compared to the breakers with larger pore sizes. Moving the bubble breaker closer to the gas nozzle also allows bubbly flow to be produced at higher GLRs. A bubble breaker with a smaller height can prevent slug bubbles from being formed after the nozzle and allow more mixing of gas and liquid phases to occur within the bubble breaker pores. Lastly, an increased bubble breaker length was shown to be more effective to produce bubbly flow at high gas-liquid flowrates ratios.

2.6 References

- [1] Kantarci, N., Borak, F., and Ulgen, K.O. 2005, "Bubble column reactors." *Process Biochemistry*, **40**(7), pp. 2263-2283.
- [2] Jakobsen, H.A., Lindborg, H., and Dorao, C.A. 2005, "Modeling of Bubble Column Reactors: Progress and Limitations." *Industrial and Engineering Chemistry Research*, **44**(14), pp. 5107-5151.
- [3] Leonard, C., Ferrasse, J., Boutin, O., Lefevre, S., and Viand, A. 2015 "Bubble column reactors for high pressures and high temperatures operation." *Chemical Engineering Research & Design*, **100**, pp. 391-421.
- [4] Arcuri, E.J., Slaff, G., and Greasham, R. 1986, "Continuous production of thienamycin in immobilized cell systems." *Biotechnology and Bioengineering*, **28**, pp. 842-849.
- [5] Bordonaro, J.L., and Curtis, W.R. 2000 "Inhibitory role of root hairs on transport within root culture bioreactors." *Biotechnology and Bioengineering*, **70**, pp. 176-86.
- [6] Son, S.H., Choi, S.M., Lee, Y.H., Choi, K.B., Yun, S.R., and Kim, J.K. 2000, "Largescale growth and taxane production in cell cultures of *Taxus cuspidate* using a novel bioreactor." *Plant Cell Reports*, **19**(6), pp. 628-633.
- [7] Chang, I.S., Kim, B.H., Lovitt, R.W., and Bang, J.S. 2001, "Effect of partial pressure on cell-recycled continuous co fermentation by *Eubacterium limosium* kist612." *Process Biochemistry*, **37**, pp. 411-421.

- [8] Shiao, T.I., Ellis, M.H., Dolferus, R., Dennis, E.S., and Doran, P.M. 2002, "Overexpression of alcohol dehydrogenase or pyruvate decarboxylase improves growth of hairy roots at reduced oxygen concentrations." *Biotechnology and Bioengineering*, **77**, pp. 455-461.
- [9] Nanou, K., Roukas, T., and Papadakis, E. 2012, "Improved production of carotenoids from synthetic medium by *Blakeslea trispora* in a bubble column reactor." *Biochemical Engineering Journal*, **67** pp. 203-207.
- [10] Matheswaran, M., and Moon, I.S. 2009, "Influence parameters in the ozonation of phenol wastewater treatment using bubble column reactor under continuous circulation." *Journal of Industrial and Engineering Chemistry*, **15**, pp. 287-292.
- [11] Lucas, M.S., Peres, J.A., and Li Puma, G. 2010, "Treatment of winery wastewater by ozone-based advanced oxidation processes (O₃, O₃/UV and O₃/UV/H₂O₂) in a pilot-scale bubble column reactor and process economics." *Separation and Purification Technology*, **72**(3), pp. 235-241.
- [12] Fernandez-Seara, J., Sieres, J., Rodriguez, C., and Vazquez, M. 2005, "Ammonia-water absorption in vertical tubular absorbers." *International Journal of Thermal Sciences*, **44**(3), pp. 277-288.
- [13] Fernandez-Seara, J., Uhiá, F.J. and Sieres, J. 2007, "Analysis of an air cooled ammonia-water vertical tubular absorber." *International Journal of Thermal Sciences*, **46**(1), pp. 93-103.
- [14] Castro, J., Oliet, C., Rodriguez, I., and Oliva, A., 2009, "Comparison of the performance of falling film and bubble absorbers for air-cooled absorption systems." *International Journal of Thermal Sciences*, **48**(7), pp. 1355-1366.
- [15] Sada, E., Yasunishi, A., Kato, S., and Nishioka, M. 1978, "Bubble formation in flowing liquid." *The Canadian Journal of Chemical Engineering*, **56**, pp. 669-672.
- [16] Terasaka, K., Tsuge, H., and Matsue, H. 1999, "Bubble formation in cocurrently upward flowing liquid." *The Canadian Journal of Chemical Engineering*, **77**, pp. 458-464.

- [17] Chen, W.B., and Tan, B.H. 2002, "Theoretical analysis of bubble formation in a co-flowing liquid." *Journal of Chemical Engineering of Japan*, **35**(10), pp. 952-962.
- [18] Hewitt, G.F. 1978, "Measurement of two phase flow parameters," *Academic Press*, New York.
- [19] Hewitt, G.F, and Roberts, D.N. 1969, "Studies of two-phase flow patterns by simultaneous x-ray and flash photography." (AERE-M--2159), Technical report, Atomic Energy Research Establishment, Harwell (England)
- [20] Coleman, J.W., and Garimella, S. 1999, "Characterization of two-phase flow patterns in small diameter round and rectangular tubes." *International Journal of Heat and Mass Transfer*, **42**(15), pp. 2869-2881.
- [21] Ujang, P.M., Lawrence, C.J., Hale, C.P., and Hewitt, G.F. 2006, "Slug initiation and evolution in two-phase horizontal flow." *International Journal of Multiphase Flow*, **32**, pp. 527-552.
- [22] Waltrich, P.J., Falcone, G., and Barbosa, J.R. 2013, "Axial development of annular, churn and slug flows in a long vertical tube." *International Journal of Multiphase Flow*, **57**, pp. 38-48.
- [23] Fadavi, A., Chisti, Y., and Chriastel, L. 2008, "Bubble size in a forced loop circulation reactor." *Journal of Chemical Technology and Biotechnology*, **83**, pp. 105-108.
- [24] Sobrino, C., Acosta-Iborra, A., Santana, D., and de Vega, M. 2009, "Bubble characteristics in a bubbling fluidized bed with a rotating distributor." *International Journal of Multiphase Flow*, **35**(10), pp. 970-976.
- [25] Manabu, I., Masuo, K., and Zen-Ichiro, M. 1998, "Effects of pore diameter, bath surface pressure, and nozzle diameter on the bubble formation from a porous nozzle." *Metallurgical and Materials Transactions*, **29**(6), pp. 1209-1218.
- [26] Tikhomirov, V. M. 1991, "On the breakage of drops in a turbulent flow." *Selected Works of A.N. Kolmogorov Volume I: Mathematics and Mechanics*, Dordrecht: Springer Netherlands.

- [27] Hinze, J.O. 1955, "Fundamentals of hydrodynamic mechanism of splitting in dispersion process." *American Institute of Chemical Engineers Journal*, **1**(3), pp. 289-295.
- [28] Hsiao, M., Lichter, S., and Quintero, L.G. 1988, "The critical Weber number for vortex and jet formation for drops impinging on a liquid pool." *Physics of Fluids*, **31**, pp. 3560-3562.
- [29] Duan, R., Koshizukay, S., and Oka, Y. 2003, "Numerical and Theoretical Investigation of Effect of Density Ratio on the Critical Weber Number of Droplet Breakup." *Journal of Nuclear Science and Technology*, **40**(7), pp. 501-508.
- [30] Galinata, S., Masbernata, O., Guiraudb, P., Dalmazzonec, C., and Noikc, C. 2005 "Drop break-up in turbulent pipe flow downstream of a restriction." *Chemical Engineering Sciences*, **60**, pp. 6511-6528.
- [31] Hasketh, R.P., Fraser Russel, T.W., and Etchells, A.W. 1987 "Bubble size in horizontal pipes." *American Institute of Chemical Engineers Journal*, **33**(4), pp. 663-667.
- [32] Miyahara, T., Hashimoto, S., Matsunaga, H., and Akagi, Y. 1999, "Bubble splitting by turbulent jet emitted from orifice." *Journal of Chemical Engineering of Japan*, **32**(1), pp. 91-96.
- [33] Miyahara, T., Matsunaga, H., and Akagi, Y. 1999, "Bubble splitting by turbulent jet emitted from nozzle." *Journal of Chemical Engineering of Japan*, **32**(5), pp. 704-707.
- [34] Alvare, J., and Al-Dahhan, M.H. 2006, "Liquid mixing in trayed bubble column reactors." *Chemical Engineering Science*, **61**(6), pp. 1819-1835.
- [35] Yang, J.H., Hur, Y.G., Lee, H.T., Yang, J.I., Kim, H.J., Chun, D.H., Park, J.C., Jung, H., and Park, S.B. 2012, "Interaction between partitioning porous plate and rising bubbles in a trayed bubble column." *Chemical Engineering Research and Design*, **90**(10), pp. 1457-1466.
- [36] Kemoun, A., Rados, N., Li, F., Al-Dahhan, M.H., Dudukovic, M.P., Mills, P.L., Leib, T.M., and Lerou, J.J. 2001, "Gas holdup in a trayed cold-flow bubble column." *Chemical Engineering Sciences*, **56**, pp. 1197-1205.

- [37] Prasser, H.M, D. Scholz, D., Zippe, C. 2001, "Bubble size measurement using wire mesh sensors." *Flow Measurement and Instrumentation*, **12**(4), pp. 299-312.
- [38] Gadallah, A.H., and Siddiqui, K. 2015, "Bubble breakup in co-current upward flowing liquid using honeycomb monolith breaker." *Chemical Engineering Science*, **131**, pp, 22-40.
- [39] Serizawa, A., Feng, Z., and Kawara, Z. 2002, "Two-phase flow in microchannels." *Experimental Thermal and Fluid Science*, **26**, pp. 703-714.
- [40] Triplett, K.A., Ghiaasiaan, S.M., Abdel-Khalik, S.I., and Sadowski, D.L. 1999, "Gas-liquid two-phase flow in microchannels Part I: two phase flow patterns." *International Journal of Multiphase Flow*, **25**, 377-394.
- [41] Yue, J., Luob, L., Gonthierb, Y., Chena, G., and Yuan, Q. 2008, "An experimental investigation of gas-liquid two-phase flow in single microchannel contactors." *Chemical Engineering Science*, **63**, pp. 4189-4202.
- [42] Akbar, M.K., Plummer, D.A., and Ghiaasiaan, S.M. 2003, "On gas-liquid flow regimes in microchannels." *International Journal of Multiphase Flow*, **29**, pp. 855-865.
- [43] Munson, B.R., Okiishi, T.H., and Huebsch W.W. 2009, *Fundamentals of Fluid Mechanics*. Hoboken, NJ: J. Wiley & Sons.

Chapter 3

3 Two-Phase Vertical Co-Flow Heat Transfer in the Presence of a Mesh-Type Bubble Breaker

3.1 Introduction

Bubble column reactors are common components in many processes where the gas and liquid phases are primarily engaged in chemical interactions [1-3]. Some common applications include the production of biological industrial products in the biochemical industry [4-9], wastewater treatment [10, 11] and absorber units for heat absorption refrigeration systems [12-14]. In addition to chemical interactions, the gas and liquid phases in a bubble column reactor may also undergo heat exchange among themselves or with the surroundings [15-17]. A good example is the absorber unit in a heat absorption refrigeration system, where the rate of heat transfer from ammonia-water two-phase solution is required to be higher than that of the condenser and evaporator in the system [18].

A common type of bubble column reactor is a vertical tubular reactor. In this design, the gas phase is cocurrently injected from a single nozzle into a vertically upward flowing liquid. To effectively design bubble column reactors, engineers need to be able to accurately predict both the rate of chemical reaction and the rate of heat transfer required for the specific system.

Heat transfer in two-phase flows has been an active area of research for several decades. A comprehensive review work by Butterworth and Hewitt [19] provides a detailed description of key parameters involved in two-phase flow heat transfer in both vertical columns and horizontal channels. They also discussed various methods of measuring two-phase flow heat transfer and presented a general empirical correlation to predict the convective heat transfer coefficient for fully developed two-phase vertical cocurrent flow. The correlation was limited to circular tubes with liquid flowrates of $Re_{SL} > 4000$.

Chu and Jones [20] performed experiments with upward and downward vertical two-phase flows using air and water as working fluids. The study was conducted over a large

range of liquid Reynolds numbers ($16000 < Re_{SL} < 112000$) that allowed for multiple flow regimes to be examined. A correlation for the two-phase Nusselt number was proposed. The correlation was similar to the correlation for the single-phase Nusselt number that was proposed by Seider and Tate [21].

Correlations like the one proposed by Chu and Jones [20] and many others are summarized in a study by Kim et al. [22]. The study compared twenty existing two-phase heat transfer correlations and their ability to predict two-phase convective heat transfer coefficients from seven existing datasets available in the literature. The datasets covered a large range of flow regimes for both vertical and horizontal two-phase flows. Comparisons between the actual results of the datasets and the predicted results from the existing correlations were made with and without considering the author-specified applicable range. It was found that no correlation was able to predict the results for all of the given datasets. Recommendations for each correlation were made to specify the flow patterns and liquid and gas combinations that can be accurately predicted by the specified correlation.

Kim et al. [23], in a continuation of previous work [22], identified the key parameters common to existing heat transfer correlations in an effort to develop a correlation that can be used to predict the two-phase convective heat transfer coefficients for all possible fluid combinations in vertical tubes. They proposed a power law correlation to predict the two-phase convective heat transfer coefficient as a function of the superficial liquid convective heat transfer coefficient, the void fraction, the mass fractions and the liquid and gas Prandtl numbers and dynamic viscosities. Exponent values for the correlation were determined by curve fitting the correlation to data from three existing studies that covered a large range of gas-liquid combinations, flow combinations and flow regimes. The resulting correlation was able to predict all 255 data points from the three data sets within $\pm 30\%$ of the actual value. As per the proposed correlation, the convective heat transfer coefficient increases with increasing gas flowrate. The correlation however, ignores the effects of flow regime transition and was limited to fully-developed two-phase flows with a superficial liquid Reynolds number $Re_{SL} > 4000$. In several applications involving vertical tubular bubble column reactor, the heat transfer in the

entrance region comprises a significant fraction of the overall heat transfer. Similarly, in many applications, the column reactor operates at low liquid flow rates ($Re_{SL} < 4000$). A good example is the vertical tubular absorber for a small-scale heat absorption refrigeration system, where multiple tubes are used and the liquid flowrate in each individual tube has a superficial Reynolds number of $Re_{SL} < 4000$ [12, 13].

Relatively limited work has been reported in the literature on the heat transfer in two-phase flows at low liquid Reynolds numbers. Kaminsky [24] used a method similar to that of Kim et al. [23] to present a general correlation for the laminar convective heat transfer correlation for two-phase vertical pipe flow. Kaminsky's [24] laminar correlation only takes into account the liquid hold-up of the flow and the convective heat transfer coefficient for the liquid at the given superficial liquid flow conditions. Furthermore, the correlation assumed uniform surface temperature of the pipe to consider the constant liquid Nusselt number value for the laminar flow i.e. $Nu_L=3.66$. The proposed correlation was able to predict the majority of the two-phase convective heat transfer coefficients from previous studies within 33% for flows with a liquid hold-up of $H > 0.2$. For flows with smaller gas hold-up values, the correlation overestimated the heat transfer coefficient with an error of up to 70% [24]. In addition, the influence of two-phase flow regime transition on the heat transfer has not been taken into consideration in the reported correlation.

Researchers have conducted similar studies for horizontal two-phase pipe flows. Kim and Ghajar [25] proposed a correlation to predict the two-phase convective heat transfer coefficient for horizontal two-phase flow using the same key parameters found in existing correlations. To determine the exponent values for the correlation, results from an in-house experiment as well as a previous study by Kim and Ghajar [26] were used for data curve fitting. Although the correlation for vertical two-phase flow predicted that the heat transfer rate increases with increasing gas flow rate, the results from the in-house experiment for horizontal flow revealed deviations from this trend. It was found that the heat transfer coefficient increases with increasing gas flowrate in the plug flow regime. Once transitioned to slug and slug-bubbly flow, the heat transfer coefficient was found to decrease with an increase in the gas flow rate. However, as the flow transitioned to the

annular flow regime, the heat transfer coefficient started to increase again. To account for the change in flow regime, a new variable, the flow pattern factor, was added to the correlation [26]. This accounted for the change in wetted pipe surface that was not accurately predicted by the void fraction alone. With the flow pattern factor added to the correlation, the exponent values were determined by curve fitting the correlation to the experimental values allowing the correlation to predict 93% of the experimental values within $\pm 20\%$ deviation [26]. Vaze and Banerjee [27], proposed another power law correlation for the two-phase Nusselt number for horizontal pipe flow using variables that are easy to attain a priori such as the superficial liquid and gas Reynolds numbers, liquid and gas Prandtl numbers and dynamic viscosities, and the Lockhart-Martinelli parameter (non-dimensional pressure drop). To overcome changes in heat transfer due to flow regime change, Vaze and Banerjee [27] proposed that different exponents should be used for different flow regimes. The correlation exponents for eight flow patterns were determined from in-house experimental data as well as data from the literature.

The studies of two-phase heat transfer for horizontal pipe flow highlighted the deficiency in the current scientific knowledge to characterize the influence of flow regime change on the heat transfer in two-phase vertical pipe flow. The current correlations proposed by Kim et al. [23] and Kaminsky [24], do not account for the flow regime change and use variables that are difficult for designers to determine a priori. Further, all of the previous studies for both horizontal and vertical two-phase flow only consider the heat transfer rate from a fully developed flow, limiting their use for predictions for bubble column reactors where the entrance region contributes significantly to the heat transfer.

Bubble column reactors that involve the absorption of the gas into the liquid, higher rate of mass exchange between the two phases is critical for the efficient operation of the reactor. The interfacial exchange of heat and mass or chemical reactivity between the two phases is heavily dependent on the contact area between the two phases. Higher the interfacial surface area, higher will be the specie transport across the interface. It is well known that in a bubble column reactor, the gas-liquid interfacial area increases by generating smaller and more numerous bubbles, since it increases the bubble surface area to volume ratio. Several techniques have been used to generate smaller bubbles or break

large bubbles into smaller ones. These techniques include the generation of turbulence within the liquid phase to split bubbles by the action of shear stress [28-31]. The use of inserted devices with small pores such as perforated plates, wire mesh screens and honeycomb mesh to physically shear and split bubbles as they pass through the pores [32-34]. Previous studies on bubble breakup were mainly focused on bubble size reduction in the two-phase bubbly flow regime. There is a scarcity of studies investigating the effects of bubble breakup techniques on the heat transfer. Since it has been shown by Kim and Ghajar [26] and Vaze and Banerjee [27] that the flow regime in a two-phase pipe flow can affect the heat transfer rate, the use of devices that alter the two-phase flow structure and shift the regime transition will likely affect the heat transfer rate.

The current study investigates the heat transfer in a two-phase gas-liquid cocurrent flow in a vertical pipe under laminar liquid flow conditions ($Re_{SL} < 2000$). Flow types ranging from bubbly to churn are considered to investigate the effect of flow regime on the convective heat transfer coefficient. The study also examines the effect of mesh-type bubble breakers on heat transfer.

This study is a continuation of the work presented in the previous chapter. Although a new experimental apparatus is built for the purpose of heat transfer measurement, results from the flow characterization apparatus presented in the previous chapter will be utilized as necessary.

3.2 Nomenclature

Variables

D	Tube Diameter, m
H	Gas Holdup, dimensionless
H	Convective Heat Transfer Coefficient, W/m ² K
ID	Inside Diameter, m
L	Length, m

N	Number of samples
Nu	Nusselt Number, dimensionless
OD	Outside Diameter, m
Pr	Prandtl Number, dimensionless
Q	Volumetric Flowrate, m ³
\dot{Q}	Rate of Heat Transfer, W
Re	Reynolds Number, dimensionless
S	Pore Size, mm
t	Thickness, mm
T	Temperature, °C
x	Mass Fraction, dimensionless
y	Position, m
α	Void Fraction, dimensionless
μ	Dynamic Viscosity, kg/m s

Subscripts

L	Liquid
G	Gas
r	Room
b	Bulk
SL	Superficial Liquid

SG	Superficial Gas
s	Surface
TP	Two Phase

3.3 Experimental Setup and Procedure

The experimental apparatus used in this study is shown in Figure 3.1. It comprised of a thin-walled stainless steel tube ($OD=16\text{mm}$, $ID=15\text{mm}$) 80cm long placed vertically above a plenum ($5\text{cm} \times 5\text{cm}$ cross section and 10cm high). Air and water were used as test fluids. Water was pumped into the plenum from a reservoir via a pump (Rigid AC11301). A flow meter (Omega FL-2053-SS) was installed downstream of the pump to control the water flow rate. The accuracy of the flowmeter for the volumetric flowrate was $\pm 5\%$. To ensure the same inlet conditions of water into the test apparatus, the water temperature inside the reservoir was maintained via an electric heating element controlled by a PID controller, with an accuracy of $\pm 0.05^\circ\text{C}$, using a feedback control loop (see Figure 3.1). In this study, the temperature of water in the reservoir was maintained at 80°C .

The air was supplied from a compressed air line into the lab. The compressed air first entered a settling tank to dampen any line pressure fluctuations. A flowmeter (Omega FL-2012-SS) was installed downstream of the settling tank to control air flowrate. The accuracy of the flowmeter for the volumetric flowrate was $\pm 5\%$. The air then passed through a brass tube inserted in the water plenum. This allowed the air temperature to rise to approximately the same temperature as the inlet water. A glass nozzle ($OD=3.2\text{mm}$, $ID=2.5\text{mm}$) was inserted into the brass tube through which the air was injected into the upward flowing liquid stream inside the steel tube. The tip of the glass nozzle was located at a height of 30mm from the steel tube inlet. The geometry of the apparatus was chosen to be identical to the flow characterization apparatus from the previous chapter. This will ensure that the flow characteristics at given flow conditions are identical and results from the flow characterization apparatus can be used to describe the flow in the heat transfer apparatus.

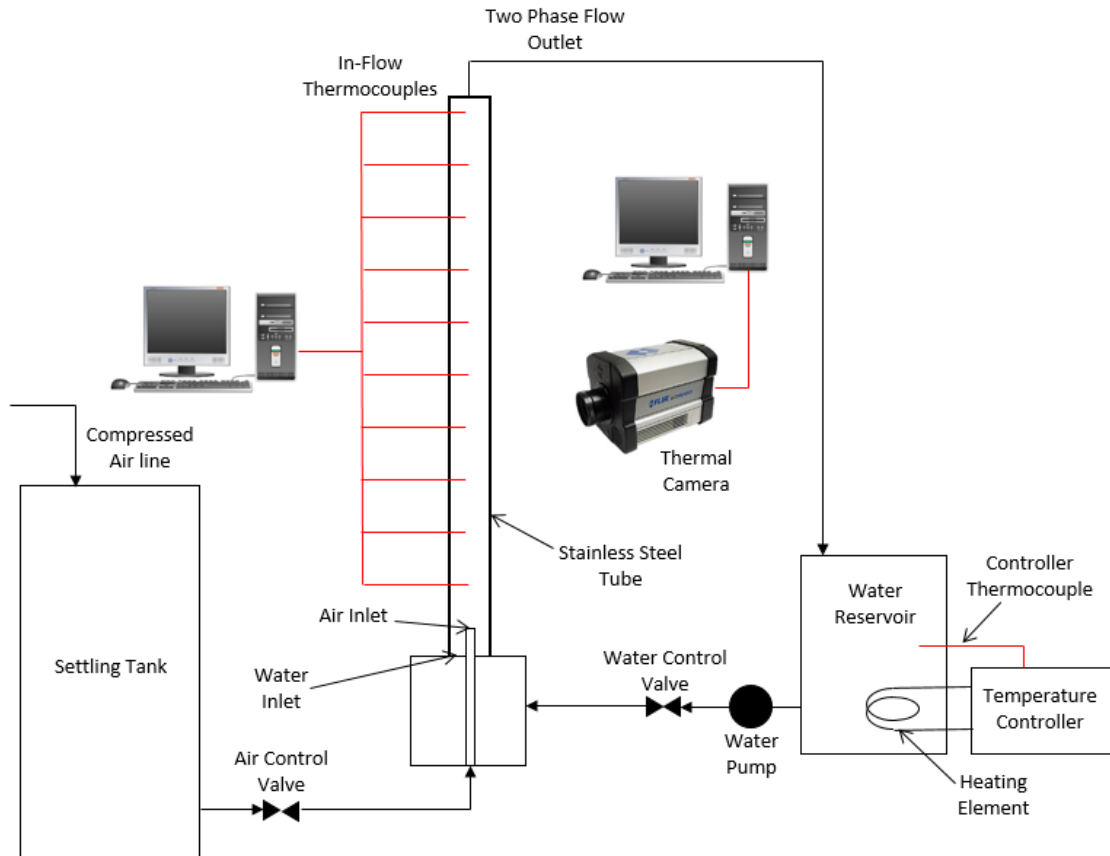


Figure 3.1: The schematic of the apparatus used to measure the two-phase heat transfer rate. Separate computers were used to record the data from the in-flow thermocouples and the thermal camera. A PID Temperature controller was used to keep the water reservoir at a constant temperature of $T_b=80^\circ\text{C}$.

Three mesh-type bubble breakers with square pores were used to investigate their effect on the two-phase convective heat transfer. All three bubble breakers were cylindrical in shape, had lengths of $L=15\text{mm}$, a wall thickness of $t=0.5\text{mm}$ and a diameter of $D_{bb}=15\text{mm}$ allowing for a press fit into the stainless steel tube. The bubble breakers were made using a Makerbot Replicator 3D printer with ABS plastic. Bubble breakers with pore sizes of $S=1\text{mm}$, $S=2\text{mm}$ and $S=4\text{mm}$ were used. The cross section of the bubble breaker with a pore size of $S=2\text{mm}$ is shown in Figure 3.2.

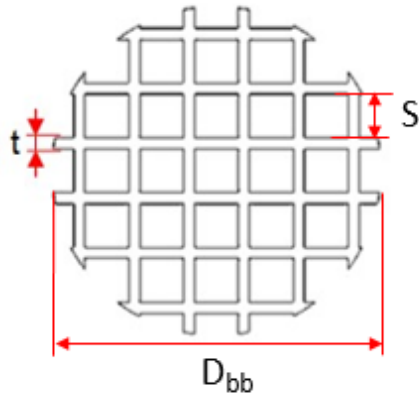


Figure 3.2: Bubble Breaker cross section showing various geometric parameters; bubble breaker thickness (t), diameter (D_{bb}) and pore size (S).

As both hot fluids travelled up the tube as a two-phase flow, heat was lost to the air ($T_r=23^\circ\text{C}$) surrounding the tube. To increase the rate of heat transfer for better characterization, three small fans were placed on a side of the stainless steel tube in a vertical series using a wooded frame (see Figure 3.3). The fans generated a uniform horizontal airflow with a velocity of 2m/s that induced forced convection around the tube over its length.

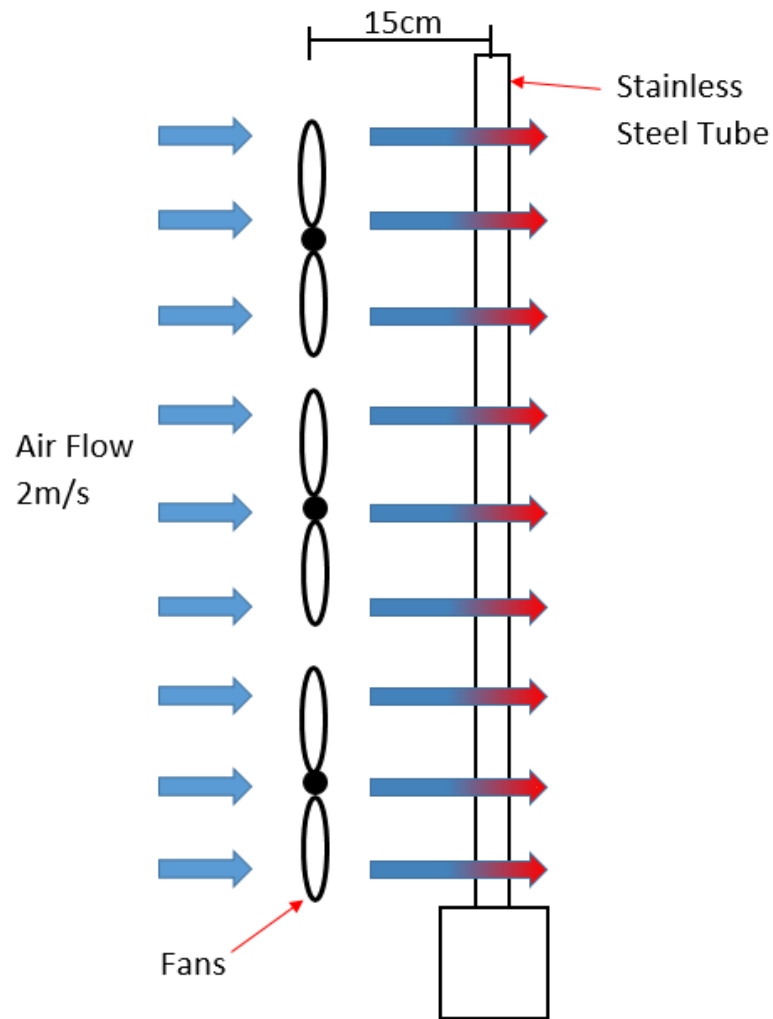


Figure 3.3: A schematic showing the placement of three small fans to induce a uniform horizontal airflow across the vertical stainless steel pipe causing forced convection heat transfer to occur between the pipe surface and the surrounding air.

Ten thermocouples were placed inside the steel tube at different vertical locations. The thermocouples were carefully inserted such that their sensors were positioned in the center of the tube to measure the bulk fluid temperature. The thermocouples were evenly spaced between 5 cm and 50 cm above the tube entrance. The thermocouples were connected to data acquisition cards (thermocouple modules: NI-9214 and NI-9211) installed in a chassis. The cards were connected to a PC via USB port. LabVIEW software was used to acquire temperature data from these thermocouples at a rate of 10 Hz. To measure the

outside surface temperature of the stainless steel tube, a FLIR SC6000 thermal camera was used. The camera was connected to a PC via an Ethernet port. Therma CAM Researcher Pro 2.9 software was used to control the camera and record thermal images.

Experiments were conducted at liquid flowrates of $Q_L = 0.13, 0.38$ and 0.63 LPM and gas flowrates of $Q_G = 0.2, 0.5$ and 1 LPM. These correspond to superficial liquid Reynolds numbers of $Re_{SL} = 380, 1150$ and 1900 and a superficial gas Reynolds numbers of $Re_{SG} = 16, 40$ and 79 . The superficial gas Reynolds numbers were calculated as,

$$Re_{SG} = \frac{4\rho_G Q_G}{\pi\mu_G D} \quad (1)$$

where D represents the inside diameter of the stainless steel tube. The superficial liquid Reynolds number was calculated using the same equation by replacing the values with the liquid flowrate and liquid properties. The volumetric gas-liquid flowrates ratio (GLR) range for the study was $0.3 - 8.1$.

For each experimental run, the measurements were started once the system reached steady state. The thermocouple data were recorded for 60 seconds and one image was recorded from the thermal camera. The time-averaged value of the temperature from each thermocouple was used as the bulk flow temperature at the given location, although the data over the 60 seconds had low statistical variance as the temperatures were at steady state. The surface temperature at nine positions along the length of the tube was obtained by averaging the surface temperature from the thermal image over an area of 45 mm^2 that corresponds to the position halfway between two in-flow thermocouples during the steady state. The temperature of the tube surface was measured over an area rather than a single point to overcome the non-uniform temperature along the surface area of the pipe due to the forced convection heat transfer. In the cross-sectional plane, the leading edge of the pipe that the force airflow comes into contact with, causes a stagnation point that reduces the local heat transfer; this causes a local hot spot to occur on the pipe surface. On the sides that were perpendicular to the direction of the flow, the air velocity was highest, resulting in an increased heat transfer and generated a local cold spot. The trailing surface of the tube remains in the wake of the flow where, like the leading edge,

the heat transfer rate is decreased causing a hot spot to occur. The thermal camera faced the stainless steel tube perpendicular to the forced air flow. The area on the tube used to measure the temperature at a given height spanned the regions of the local hot and cold spots to provide an accurate estimation of the surface temperature for the purposes of estimating the heat transfer rate. Since the stainless steel tube was thin walled and had a high conductivity it was assumed that the outside surface temperature was equal to the inside surface temperature. For the purposes of error analysis, it is assumed that the uncertainty in the temperature measurements is equivalent to the accuracy of the measuring instrument which was $\pm 0.05^\circ\text{C}$ for both thermocouples and the thermal camera. An example of the temperature data obtained during this study at superficial liquid Reynolds number of $Re_{SL}=1150$ and a superficial gas Reynolds number of $Re_{SG}=40$, in the absence of a bubble breaker is shown in Figure 3.4.

The plot in Figure 3.3 shows, as expected, that both the bulk flow and surface temperatures decreased with an increase in the height. The plot also shows that the trends of the temperature decrease are linear. The local heat transfer coefficient at a given height was calculated from the measured temperature data using the energy conservation law (Equation 2), and Newton's law of cooling (Equation 3), and is shown in Equation 4.

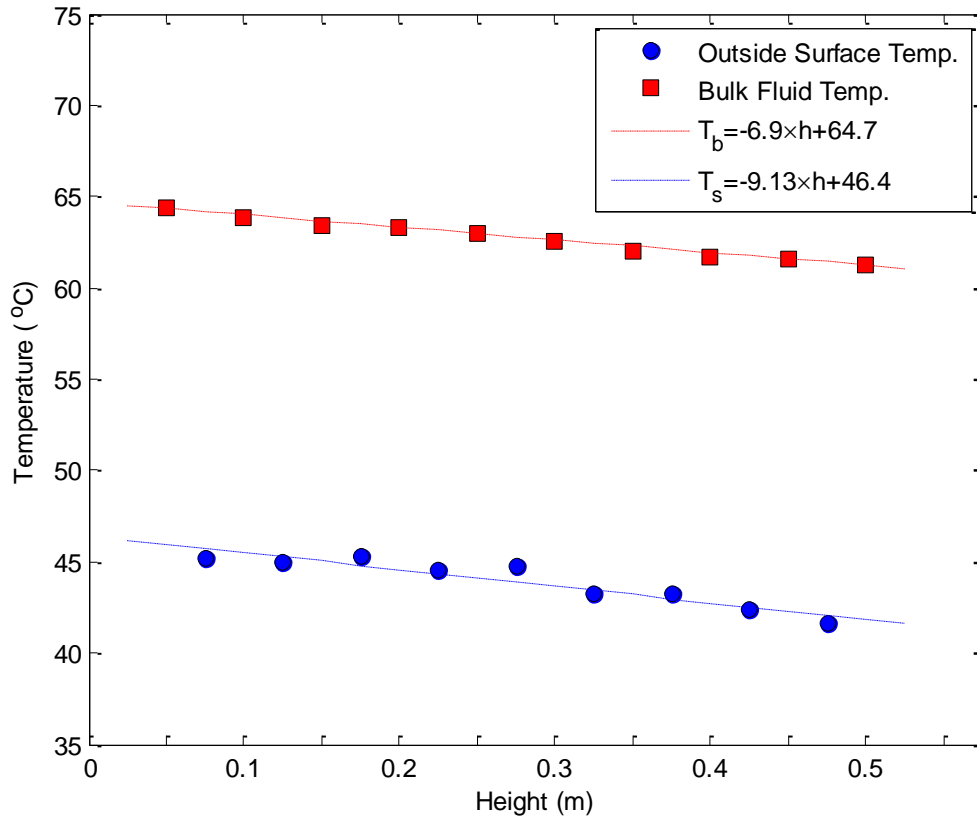


Figure 3.4: A temperature plot of a two-phase flow with a superficial liquid Reynolds number of $Re_{SL}=1150$ and a superficial gas Reynolds number of $Re_{SG}=40$.

$$\dot{Q}'(y) = (\dot{m}_L c_{pL} + \dot{m}_G c_{pG})(\delta T_b / \delta y) \quad (2)$$

$$\dot{Q}'(y) = h_{TP}(y) D \pi (T_s(y) - T_b(y)) \quad (3)$$

$$h_{TP}(y) = \frac{(\dot{m}_L c_{pL} + \dot{m}_G c_{pG})(\delta T_b / \delta y)}{D \pi (T_s(y) - T_b(y))} \quad (4)$$

The value of $\delta T_b / \delta y$ was calculated as the difference in the measured bulk temperature between two adjacent thermocouples. The value of T_b in Equation (4) is the average of the bulk temperatures at two adjacent thermocouples, while the value y represents the height along the length of the tube halfway between those two thermocouples. T_s is the temperature of the tube wall at the position y . The average convective heat transfer

coefficient for the entire tube length was calculated by averaging the local convective heat transfer coefficient values at nine heights along the tube corresponding to the locations halfway between the inserted thermocouples. A plot of the local convective heat transfer coefficient as a function of the position along the tube length for the same flow conditions as Figure 3.4 is shown in Figure 3.5. Error analysis was conducted to estimate the uncertainty in the computed values of the convective heat transfer coefficients, $h_{TP}(y)$ by taking into consideration the measurement error from the flowmeters, thermocouples and thermal camera. These are the error bars seen in Figure 3.5. For the average heat transfer coefficients the uncertainty was estimated as the root mean square of the propagated errors given as,

$$\Delta \overline{h}_{tp} = \sqrt{\frac{\sum(\Delta h_{tp}(y))^2}{N}} \quad (5)$$

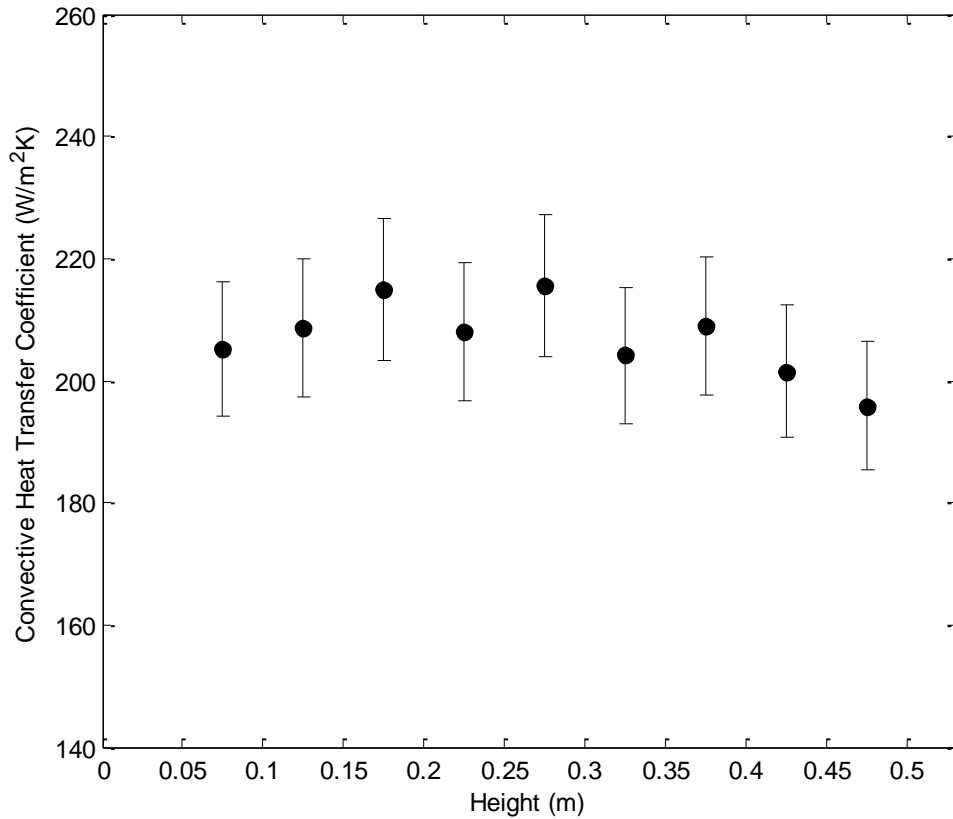


Figure 3.5: Local convective heat transfer coefficients along the tube length for a two-phase flow ($Re_{SL}=1150$ and $Re_{SG}=40$). The error bars represent propagated measurement error from the thermocouples, thermal camera, and flowmeters.

To validate the method, testing was conducted using a single-phase liquid (water) flow and the results were compared with the classical Nusselt number value of $Nu_L=4.36$, for single-phase laminar pipe flow with uniform heat flux at the surface of a pipe [35]. Figure 3.6 shows the single-phase liquid Nusselt numbers obtained in the validation testing at different liquid Reynolds numbers. The error bars shown for the Nusselt number values was calculated as,

$$\Delta Nu = D_i \frac{\overline{\Delta h_{tp}}}{k_L} \quad (6)$$

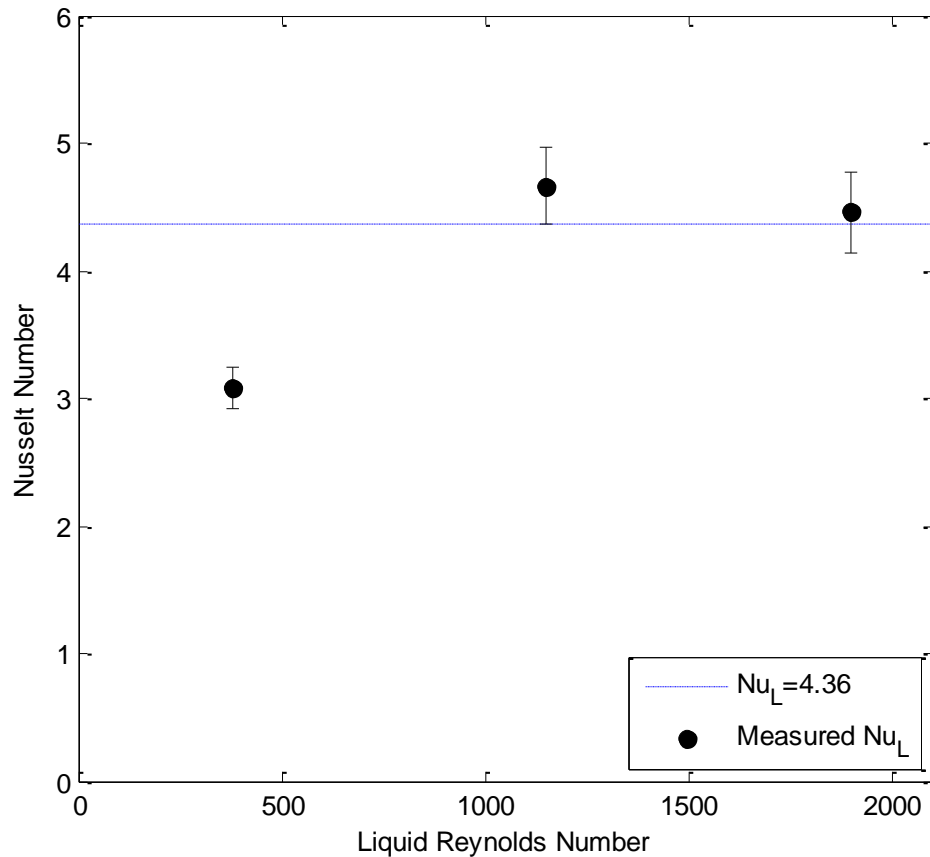


Figure 3.6: The measured Nusselt number for a single phase flow at different Reynolds number compared to the classical Nusselt number for laminar pipe flow with constant surface heat flux, $Nu_L=4.36$ [33]. The error bars represent the root mean square of the propagated measurement errors.

The results presented in Figure 3.6 show that for $1000 < Re_L < 2000$, the measured values of the Nusselt number are very close to 4.36. The average difference was 4.6%. The results however show that the measured Nusselt number value at the lowest Reynolds number was significantly lower than the classical value. At the lowest flowrate, the inertia of the flow is not strong enough to overcome the buoyancy effects of natural convection. At this flowrate the ratio of Grashof Number to the square of the Reynolds number is $Gr/Re_L^2 = 8$, indicating that natural convection was more dominant than forced convection [35]. The value of $Nu_L=4.36$ is only used for inertia dominated (forced convection) laminar flow when $Gr/Re_L^2 \ll 1$. Due to the dominance of natural

convection in this case, the value of the convective heat transfer coefficient is expected to be lower than that for the forced convection case. Nevertheless, the results in Figure 3.6 show that the apparatus is able to provide accurate measurements of the convective heat transfer coefficient.

The classical case of $Nu_L=4.36$ will be used as a comparison case when analyzing the two-phase convective heat transfer coefficient. Two-phase convective heat transfer is inherently more complex than convection in a single-phase flow. This is attributed to the fluid mixing caused by the gas-phase as it passes within the liquid stream as well as the differences in the thermophysical properties of the two fluids.

3.4 Results and Analysis

3.4.1 Two-Phase Convective Heat Transfer Coefficient (no bubble breaker)

The measured two-phase convective heat transfer coefficients over a range of superficial gas and liquid Reynolds numbers are shown in Figure 3.7. At a given condition, the value presented in the figure is the average of the local heat transfer coefficient values computed over the tube length. The figure shows that at a given superficial liquid Reynolds number (Re_{SL}), the convective heat transfer coefficient decreased with an increase in the superficial gas Reynolds number (Re_{SG}). While, at a given Re_{SG} , the convective heat transfer coefficient increased with an increase in Re_{SL} . The classical case of single-phase laminar pipe flow with uniform heat flux ($Nu_L = 4.36$) [35], corresponds to the single-phase convective heat transfer coefficient of $h_L=174 \text{ W/m}^2\text{K}$ in the present setup. Comparison of this classical case with the two-phase convective heat transfer coefficients in Figure 3.7 show that the two-phase flows with the two highest liquid flowrates ($Re_{SL}=1150$ and 1900) have higher convective heat transfer coefficients than the single-phase liquid heat transfer coefficient. While the two-phase flows at the lowest liquid flowrate ($Re_{SL}=360$), have convective heat transfer coefficients lower than that the classical value for single-phase liquids.

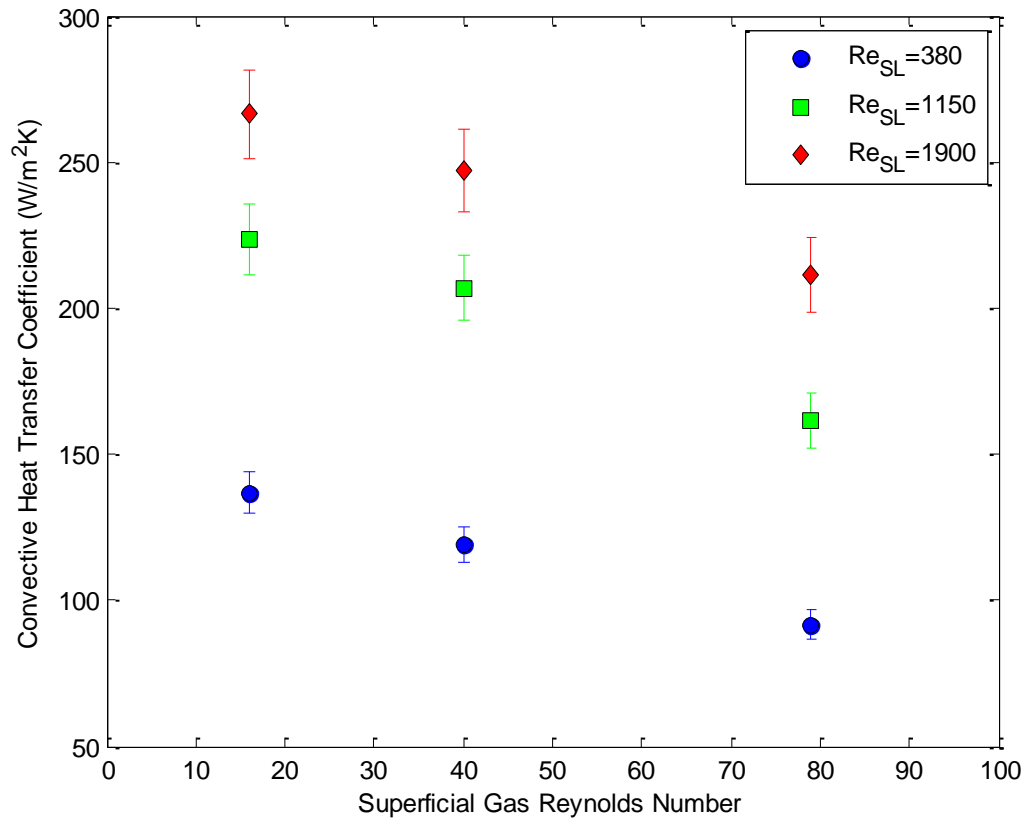


Figure 3.7: Convective heat transfer coefficients for two-phase vertical pipe flow at various superficial gas and liquid Reynolds numbers. The error bars represent the root mean square of the propagated errors from the local heat transfer coefficient values.

At the lowest liquid flowrate, the liquid inertia was weak and hence the buoyancy forces were dominant in the upward movement of the gas volumes exiting from the nozzle, similar to the flow in the stagnant liquid column. As the gas phase was travelling upwards at a faster velocity than the liquid, it was pushing the liquid phase towards the pipe walls resulting in the formation of thin liquid layer along the pipe wall. This liquid layer lost heat quicker due its close proximity to the pipe wall whereas, the heat transfer from the gas phase occupying the bulk of the pipe domain was relatively low, causing an overall reduction in the two-phase heat transfer coefficient compared to that in a single-phase liquid flow.

Figure 3.7 also shows a general trend of decreasing heat transfer coefficient with an increase in the superficial gas Reynolds number. This is likely due to the reason that at a given liquid flow rate, an increase in the gas flow rate reduces the bubble detachment frequency, and hence generates larger gas bubbles. Furthermore, it also reduces the liquid space between each individual bubble, thus suppressing the wakes. When wakes are formed behind the gas phases [36] which induces mixing between the high temperature liquid in the central region of the pipe with the liquid layer at the wall, thus, enhancing the heat transfer at the wall. A suppression or reduction of the wake reduces the heat transfer. Furthermore, at a given liquid flow rate, an increase in the gas flowrate may also lead to the transition of the two phase flow regimes from bubbly to slug to churn. This transition also influences the dynamics and interaction between the gas and liquid phases and hence influences the heat transfer. The trend observed in Figure 3.6 is opposite to the correlation proposed by Kim et al. [22]. Their correlation, as shown in Equation (6), predicts that the two-phase heat transfer coefficient increases with increasing gas flowrate. Their correlation is intended for two-phase flow with a superficial liquid Reynolds number of $Re_{SL} > 4000$.

$$h_{TP} = (1 - \alpha)h_L + 0.27 \left[\left(\frac{x}{1-x} \right)^{-0.04} \left(\frac{\alpha}{1-\alpha} \right)^{1.21} \left(\frac{Pr_G}{Pr_L} \right)^{0.66} \left(\frac{\mu_L}{\mu_G} \right)^{-0.72} \right] \quad (6)$$

The plausible causes of the difference are that the correlation proposed by Kim et al. [22] uses the single-phase liquid convective heat transfer coefficient at the given superficial flow conditions and applies a correction based on the liquid hold-up of the flow and does not account for changes in the two-phase flow regimes. As shown by Kim and Ghajar [26], and Vaze, and Banerjee [27], the heat transfer coefficient of a two-phase flow in a horizontal pipe is dependent on the flow regime. Their studies showed that the heat transfer coefficient reached minima in the slug flow regime. They also observed that in the annular flow regime, where the gas volume occupies almost the entire domain and the liquid phase is transformed into a thin layer at the wall, the heat transfer coefficient increased with increasing gas flowrate.

As mentioned earlier, in the introduction section, in the previous phase of this research work, the characterization of two-phase flow regimes in the absence and presence of a mesh-type bubble breaker was conducted in a vertical pipe. Various two-phase flow regimes that were observed at different superficial gas and liquid Reynolds numbers corresponding to those presented in Figure 3.7 are summarized in Table 1.

Table 3.1: Two-Phase Flow Regime Characterization with no Bubble Breaker Present

Re_{SL}	Re_{SG}	No Breaker
380	16	bubbly
	40	slug
	79	churn
1150	16	bubbly
	40	slug
	79	churn
1900	16	bubbly
	40	slug
	79	slug

The results from Table 1 show that over the given range of gas and liquid Reynolds numbers, various regimes including bubbly, slug and churn flow were observed. At superficial liquid Reynolds numbers of 380 and 1150, the two-phase flow transitioned from bubbly to slug to churn flow regime as the superficial gas Reynolds number increased from 16 to 79, whereas, at $Re_{SL}=1900$, churn flow was not observed over the entire range of gas Reynolds numbers. The transition from bubbly to slug to churn flow regimes, suppresses the wake size and reduces the mixing, hence the heat transfer rate. This is evident in the results shown in Figure 3.7. The trends observed in Figure 3.7 for the vertical two-phase flow are consistent with those of Kim and Ghajar [26] and Vaze

and Banerjee [27] in the horizontal two-phase flow. However, the present results indicate that in vertical two-phase pipe flows, the minima of two-phase heat transfer coefficient extends from slug flow regime to the churn flow regime.

The two-phase convective heat transfer coefficient values are converted into dimensionless form (two-phase Nusselt number, Nu_{TP}) to present results in a generalized form. The two-phase Nusselt number is calculated using Equation 7. In this equation, the conductivity of the liquid phase, k_L , is used as a scaling parameter rather than a combination of the gas phase and liquid phase conductivity. For all of the observed flows, the inner pipe surface was always covered by a thin layer of liquid, even with the added mixing from the gas phase and hence, the liquid phase is the medium in which the conduction heat transfer takes place.

$$Nu_{TP} = D_i \frac{\overline{h_{TP}}}{k_L} \quad (7)$$

The experimental data are plotted in the form of Nu_{TP} versus the ratio of superficial gas to liquid Reynolds numbers in Figure 3.8. The results show a clear linear trend of decreasing Nusselt number with an increase in the Reynolds number ratio. The best-fit line to the data is also plotted in figure, which represents the proposed correlation, presented below in the mathematical form as Equation 8.

$$Nu_{TP} = 1.5 \left(\frac{Re_{SG}}{Re_{SG}} \right)^{-0.33} \quad (8)$$

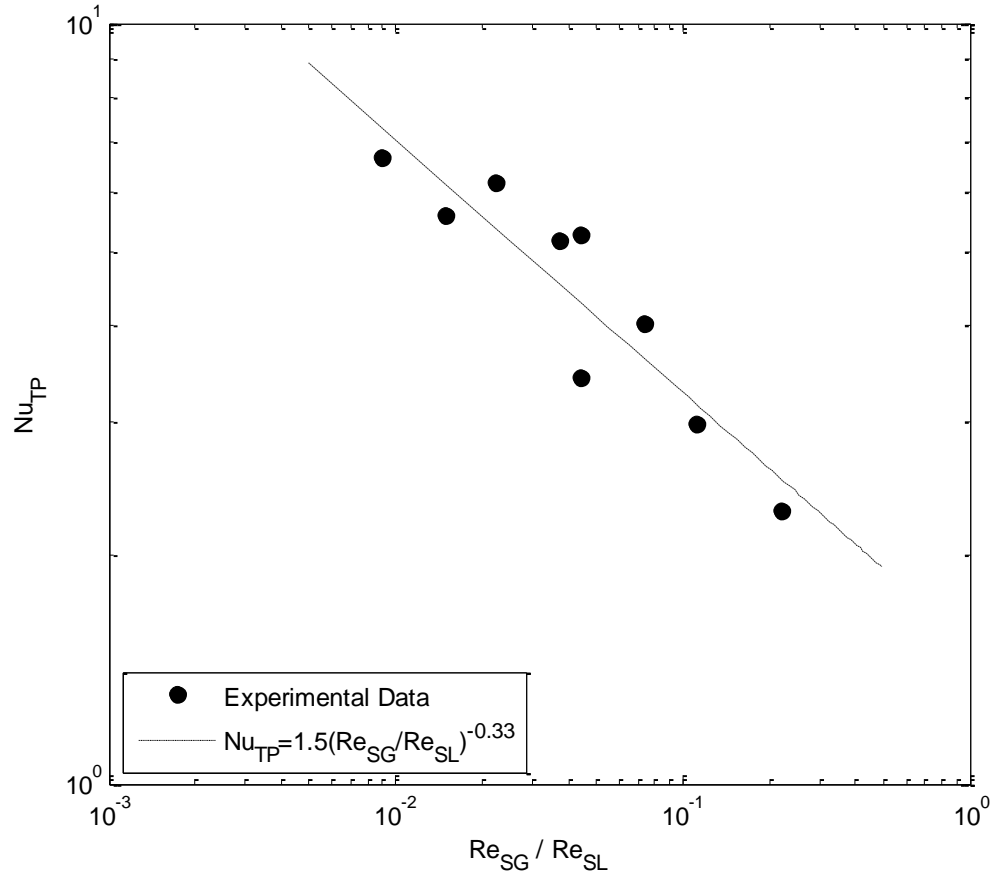


Figure 3.8: Two-phase Nusselt number plotted vs. the gas-to-liquid Reynolds number ratio. The best-fit equation is also plotted.

The correlation proposed in Equation 8 to predict the two-phase heat transfer coefficient is applicable to two-phase vertical co-flows with superficial liquid Reynolds number of $Re_{SL} < 2000$ and a superficial gas Reynolds number of $Re_{SG} < 100$, covering the two-phase flow regimes from bubbly to churn. An important feature of this correlation is its dependency on Reynolds numbers, which are parameters easy to compute. As per Vaze and Banerjee [27], the dependency of a correlation on easy to computer parameters is very critical for the designers of two-phase heat transfer systems. Since the present study used a constant inlet temperature and only varied the gas and liquid flowrates, the effects of gas and liquid Prandtl numbers and viscosities could not be determined. It is assumed that the effect of gas and liquid Prandtl numbers and viscosities will be manifested in the correlation constant. Further studies are needed to account for the liquid and gas Prandtl numbers and viscosities effect.

3.4.2 Influence of the Bubble Breaker on Heat Transfer

Three bubble breakers with pore sizes of $S=1\text{mm}$, $S=2\text{mm}$ and $S=4\text{mm}$ were used to test the effect of a bubble breaker on heat transfer in a vertical two-phase pipe flow. Each bubble breaker was placed in the stainless steel tube (see Figure 3.1), 13 mm above the gas nozzle tip. The two-phase heat transfer coefficient values for bubble breakers of different pore sizes and three superficial gas Reynolds numbers are shown in Figures 3.8, 3.9 and 3.10 for superficial liquid Reynolds numbers of 380, 1150 and 1900, respectively. The two-phase heat transfer coefficient values for the same gas and liquid Reynolds number cases in the absence of a bubble breaker are also plotted in the figures for comparison. The convective heat transfer coefficient values in the presence of bubble breakers, in general, show trends similar to those without a bubble breaker. That is, the heat transfer coefficient decreased with an increase in Re_{SG} and increased with an increase in Re_{SL} . At a given condition, the results in the presence of bubble breakers show variations with respect to the corresponding case without a bubble breaker.

The results in Figure 3.9, at the lowest liquid flow rate ($Re_{SL}=380$), show that the heat transfer coefficient in the presence of a 1 mm pore-size bubble breaker was higher than that without a bubble breaker over the entire range of Re_{SG} . For the 2 mm pore-size bubble breaker, the heat transfer coefficient was lower than that without a bubble breaker at $Re_{SG}=16$ and 40 but became higher than the no bubble breaker case at $Re_{SG}=79$. The heat transfer coefficient values for the 4 mm pore-size bubble breaker were lower than that for the no bubble breaker case over the entire range of Re_{SG} . As the liquid Reynolds number increased to $Re_{SL}=1150$ (Figure 3.10), the results show that the heat transfer coefficient for the 1 mm pore-size bubble breaker was higher than that for the no bubble breaker case at the lowest and highest gas Reynolds number. The 2 mm pore-size bubble breaker has a lower heat transfer coefficient at $Re_{SG}=16$, almost equal value at $Re_{SG}=40$ and higher value at $Re_{SG}=79$, with respect to the no bubble breaker case. The 4 mm pore-size bubble breaker showed lower heat transfer coefficient values relative to no bubble breaker case at $Re_{SG}=16$ and 40 and higher at $Re_{SG}=79$. At the highest liquid Reynolds number, $Re_{SL}=1900$ (Figure 3.11), the results show that except for the 1 mm pore-size bubble breaker case at $Re_{SG}=16$ and 40, the heat transfer coefficients without a bubble

breaker were higher than that in the presence of the bubble breaker. At $Re_{SG}=16$, the heat transfer coefficient for the 1mm pore size is equal to coefficient in the absence of a bubble breaker causing it to be covered by the 1mm pore size result. The uncertainty, not shown in Figures 3.9, 3.10 and 3.11, for heat transfer coefficients shown in all three plots is similar to the uncertainty shown in Figure 3.7. The uncertainty is mainly dependent on the mass flow rate. For the results plotted in Figure 3.9, corresponding to a superficial liquid Reynolds number of $Re_{SL}=380$, the uncertainty for the convective heat transfer coefficient is $\Delta h_{tp} \approx \pm 8 \text{ W/m}^2\text{K}$. For the results plotted in Figure 3.10, corresponding to a superficial liquid Reynolds number of $Re_{SL}=1150$, the uncertainty for the convective heat transfer coefficient is $\Delta h_{tp} \approx \pm 12 \text{ W/m}^2\text{K}$. For the results plotted in Figure 3.11, corresponding to a superficial liquid Reynolds number of $Re_{SL}=1150$, the uncertainty for the convective heat transfer coefficient is $\Delta h_{tp} \approx \pm 15 \text{ W/m}^2\text{K}$. Error bars were left off the plots to ensure the results could be easily read.

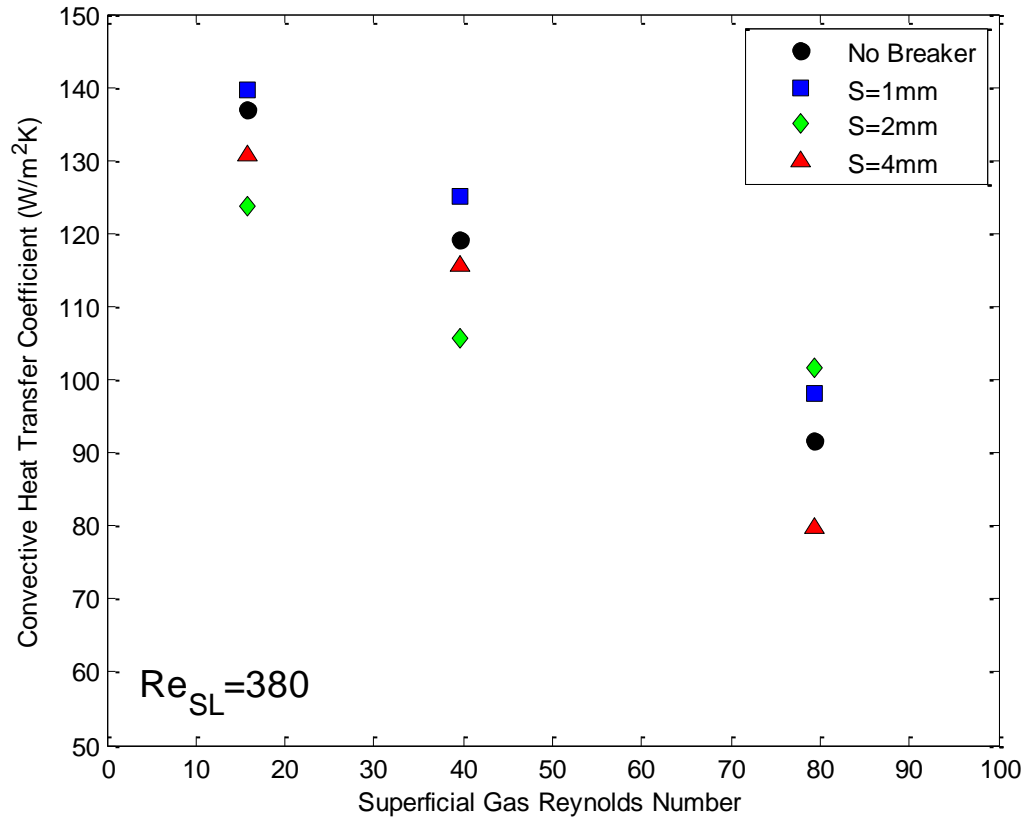


Figure 3.9: Convective heat transfer coefficients for two-phase vertical pipe flow with and without bubble breakers at a superficial liquid Reynolds number of $Re_{SL}=380$ and different superficial gas Reynolds numbers.

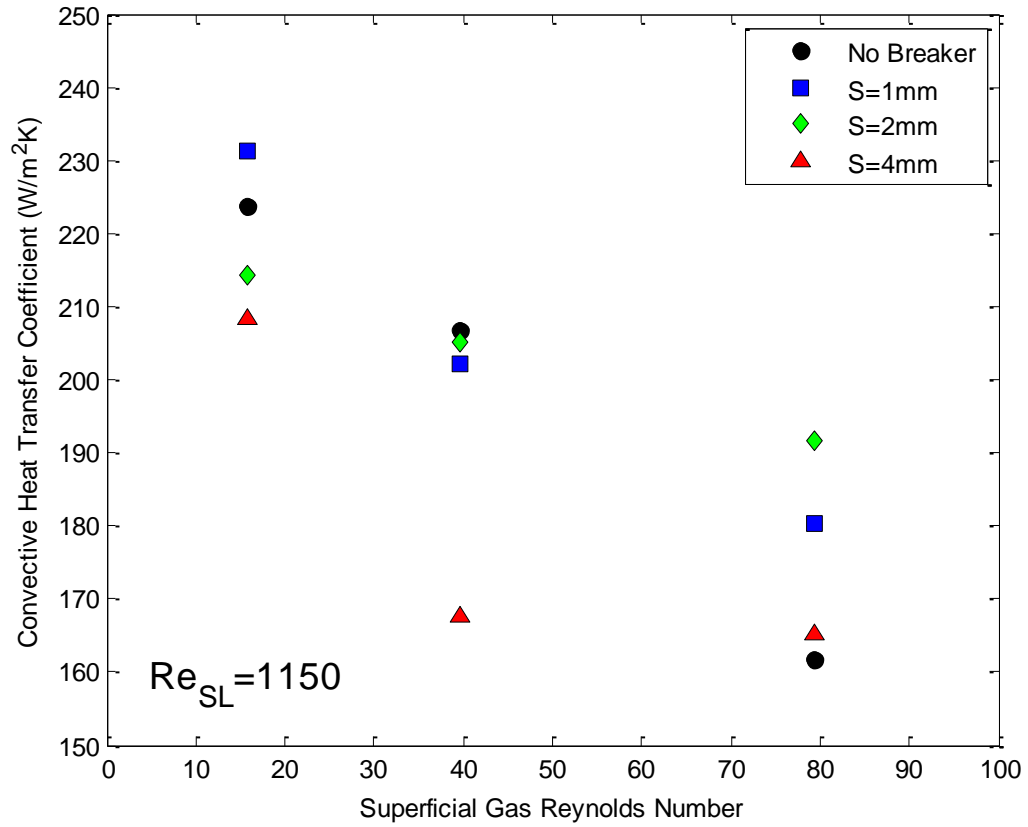


Figure 3.10: Convective heat transfer coefficients for two-phase vertical pipe flow with and without bubble breakers at a superficial liquid Reynolds number of $Re_{SL}=1150$ and different superficial gas Reynolds numbers.

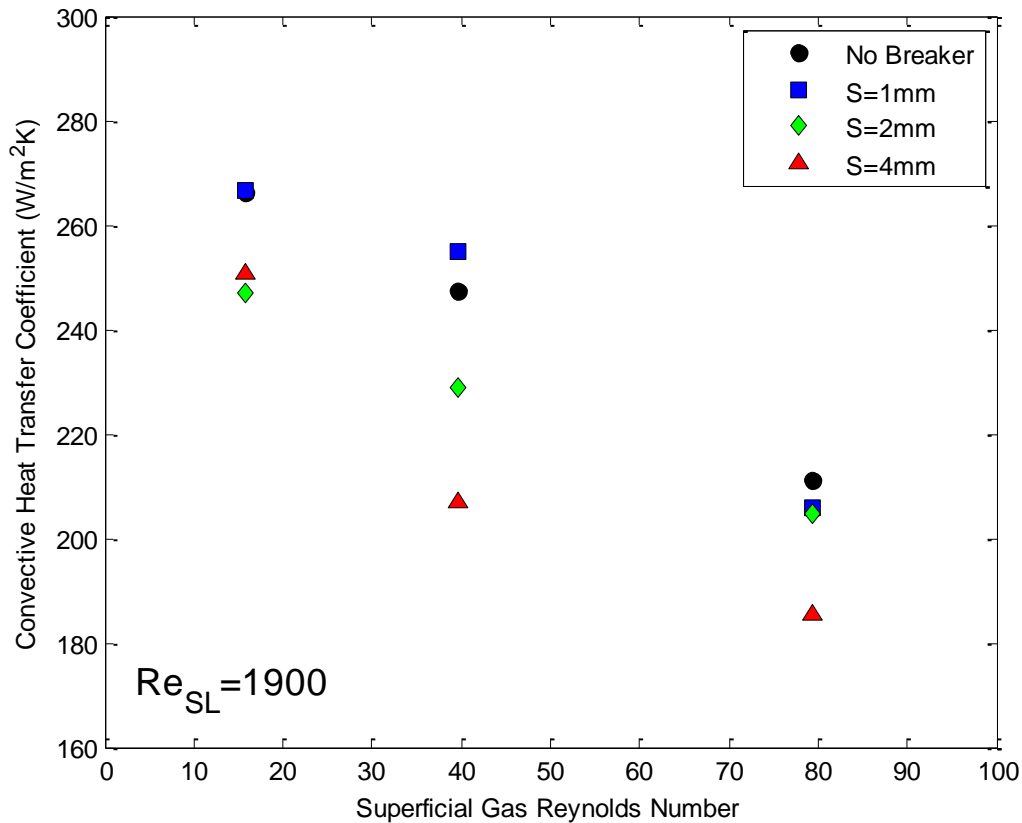


Figure 3.11: Convective heat transfer coefficients for two-phase vertical pipe flow with and without bubble breakers at a superficial liquid Reynolds number of $Re_{SL}=1900$ and different superficial gas Reynolds numbers.

The results in Figures 3.9, 3.10 and 3.11 show that contribution of a bubble breaker to enhance heat transfer coefficient is evident only at the small pore size, higher gas Reynolds number and low to moderate liquid Reynolds number. It is found that in the presence of 1 mm pore-size bubble breaker, the heat transfer coefficient on-average increased by 3% relative to the heat transfer coefficient in the absence of a bubble breaker over the given range of gas and liquid Reynolds numbers. The maximum enhancement of the heat transfer coefficient for 1 mm pore-size breaker relative to the no breaker case is found to be 12% at $Re_{SG}=79$ and $Re_{SL}=1150$.

The use of the flow characterization results from the apparatus in the previous chapter is used in an attempt to get a better understanding of how the change in flow regime due to

the bubble breaker affects the convective heat transfer coefficient. The regime characterization results for the bubble breakers used in this study are shown in Table 2.

Table 3.2: Two-Phase Flow Regime Characterization with Bubble Breakers of Varying Pore Sizes

Re_{SL}	Re_{SG}	No Breaker	S=1mm	S=2mm	S=4mm
380	16	bubbly	bubbly	bubbly	bubbly
	40	slug	bubbly	slug	slug
	79	churn	slug	slug	slug
1150	16	bubbly	bubbly	bubbly	bubbly
	40	slug	bubbly	bubbly	bubbly
	79	churn	bubbly	slug	slug
1900	16	bubbly	bubbly	bubbly	bubbly
	40	slug	bubbly	bubbly	bubbly
	79	slug	bubbly	bubbly	slug

Table 2 shows that all three bubble breakers were effective in delaying the transition from bubbly to slug or churn flow. The bubble breaker with the smallest pore size, $S=1\text{mm}$, was the most effective in delaying the transition as it eliminated slug and churn flows for all of the flow combinations at a superficial liquid Reynolds numbers of $Re_{SL}=1150$ and $Re_{SL}=1900$. The bubble breaker with the largest pore size, $S=4\text{mm}$, was still effective as it eliminated churn flow at all three liquid flowrates.

When the flow regime results in Table 2 are compared to the heat transfer results in Figures 3.9, 3.10 and 3.11, there is no clear relationship between the flow regimes, and the heat transfer trends. In many cases, for example at $Re_{SG}=40$ and $Re_{SL}=1900$, all three bubble breakers were able to produce the same flow type; however the heat transfer results varied between the bubble breakers. A more thorough analysis through observations of the flow made from the high-speed camera images is used to get a better

understanding of the effect of the flow generated by the bubble breakers on the two-phase convective heat transfer coefficient.

At the lowest liquid flowrate, $Re_{SL}=380$, where the liquid inertia was relatively weak, the breakup of the bubbles in the bubble breaker was primarily caused by the buoyancy force of the rising gas phase. The force required by the bubble to detach from the nozzle and travel through the pores of the bubble breaker increases with decreasing pore size. For the 1mm pore size bubble breaker, it was observed that a large amount of gas-holdup occurred immediately upstream of the bubble breaker. The gas phase builds up underneath the bubble breaker until the buoyancy force of the accumulated gas phase is enough to overcome the surface tension. The gas phase then travels through multiple pores of the bubble breaker and leaves as smaller daughter bubbles. As the pore sizes increase, the buoyancy force needed for the gas phase to pass through the bubble breaker is decreased, reducing the gas-holdup before the breaker. Images of the flow generated by the three bubble breakers at $Re_{SL}=380$ and $Re_{SG}=40$ respectively are shown in Figure 3.12. The higher gas-holdup by the 1mm pore size bubble breaker is clearly evident in the image, which causes the gas phase to travel through the bubble breaker intermittently. Although smaller bubbles were created, they would travel in clusters allowing wakes to form behind the clusters similar to the wakes formed in slug flow [39]. The 2mm pores allowed the gas-phase to pass through the bubble breaker with less intermittency while still producing a bubbly flow or slug flow with dispersed small bubbles. The more continuous passage of the gas-phase caused a flow with fewer liquid breaks in-between the clustered gas phases. The 4mm pore size bubble breaker produced the least amount of gas-holdup among three pore sizes; however, the bubbles generated by the pores were large and quickly coalesced to form bubbly or slug flow that resembled the flow in the absence of the bubble breaker.

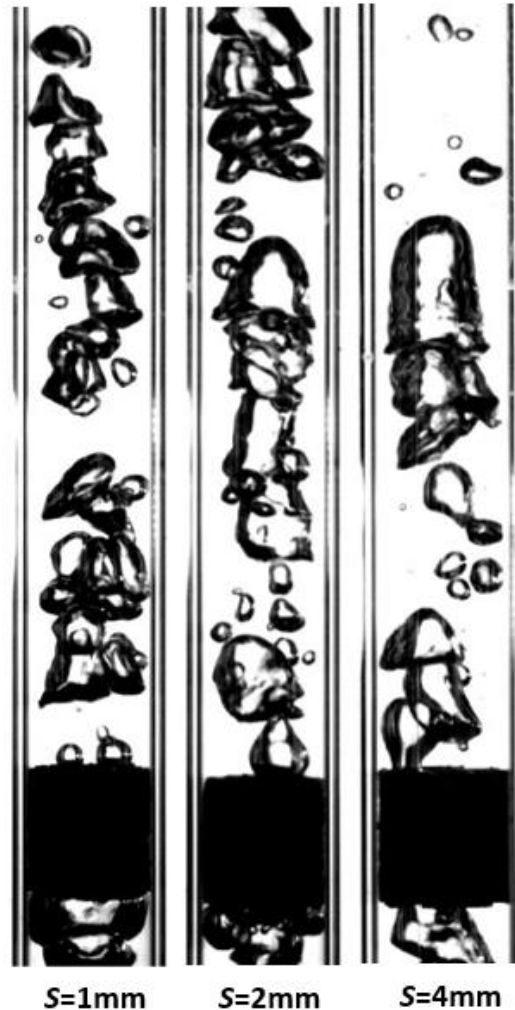


Figure 3.12: Highspeed camera images of the flow generated by three bubble breakers at the same flow conditions ($Re_{SG}=40$ and $Re_{SL}=380$).

For the 1mm pore size bubble breaker, the combination of bubbly flow causing liquid mixing at the pipe wall along with wakes forming behind the clustered bubbles resulted in increased convective heat transfer rates, relative to the flow with no bubble breaker (see Figure 3.9). By reducing the spacing between the gas-phase, thus reducing the wake mixing of the liquid phase, the 2mm pore size bubble breaker reduced the convective heat transfer rate (see Figure 3.9). The large gas slug regions generated by the 4mm pore size bubble breaker allowed more liquid mixing in the wake region compared to the 2mm pore size bubble breaker. The flow generated by the 4mm pore size bubble breaker did not have the added benefit of mixing at the wall surface, due to numerous small bubbles like the flow

generated by the 1mm pore size bubble breaker. The few small bubbles in the wake region of the slugs generated by the 4 mm pore size bubble breaker reduced the mixing effect of the wake when compared to the flow in the absence of a bubble breaker, reducing the heat transfer coefficient slightly, relative to the flow with no bubble breaker present (see Figure 3.9).

At superficial liquid and gas Reynolds of $Re_{SL}=380$ and $Re_{SG}=79$, both the 1mm and the 2mm pore size bubble breakers were able to increase the heat transfer coefficient when compared to the case with no bubble breaker (see Figure 3.9). This is due to the delay of the transition to churn flow (see Table 2). Churn flow is described as an oscillatory flow regime with long chaotic columns of gas travelling in the centre of the vertical pipe [19]. The churn flow regime causes the liquid phase to form a thin layer at the pipe wall. This layer will quickly approach the temperature of the pipe surface, and if not removed, will decrease the heat transfer rate from the two-phase flow to the surrounding air. By changing the flow regime to slug or bubbly flow, the bubble breakers allows wakes to form in the liquid regions between the separated gas slugs or clustered bubbles. The flows generated by all three bubble breakers at this flow condition can be seen in Figure 3.13. All three bubble breakers were able to delay the transition to churn flow. The 1mm and 2mm bubble breakers produced slug flow consisting of multiple small gas slug regions whereas the 4mm bubble breaker produced a slug flow with much larger gas slug regions.

The slug flows generated by the 1mm and 2mm pore size bubble breakers seen in Figure 3.13 allowed for liquid mixing at the pipe wall due to the chaotic gas-liquid interfaced generated by the numerous small slug regions. The flow also created liquid breaks between the clustered gas phases allowing wakes to be formed that generated more liquid mixing, thus enhancing the convective heat transfer coefficient (see Figure 3.9). The slug flow consisting of single large slugs generated by the 4mm pore size bubble breaker restricted the liquid closer to the pipe wall due to the presence of elongated smooth gas-liquid interface. The flow generated by the 4 mm pore size bubble breaker reduced the occurrence of liquid breaks between the gas phases causing a further

reduction in liquid mixing, thus reducing the convective heat transfer coefficient relative to the other bubble breaker configurations (see Figure 3.9).

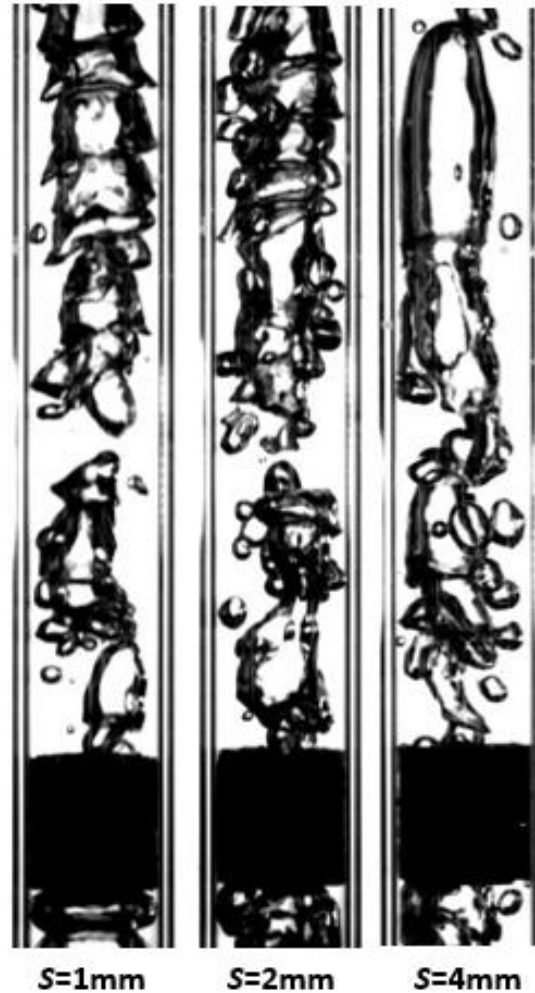


Figure 3.13: High-speed camera images of the flow generated by three bubble breakers at the same flow conditions ($Re_{SG}=79$ and $Re_{SL}=380$).

As the liquid flowrate increased ($Re_{SL}=1150$), the liquid inertia became a more dominant force in the role of bubble breakup and advection. This allowed for less intermittency of the gas phase passing through the bubble breakers and more evenly dispersed gas regions to form. At the lowest gas flowrate $Re_{SG}=16$, intermittency still existed for the 1 mm pore size. The size of the bubbles generated by the nozzle decreases in size as the liquid flow rate increases [37]. Although the liquid inertia was increased, the buoyancy force was

lowered due to the decrease in bubble size. The combined effect of liquid inertia and buoyancy force was not enough to fully overcome the surface tension of the single bubble. Coalescence of the nozzle-generated bubbles occurred upstream of the bubble breaker which resulted in a higher buoyancy force that reduced the surface tension effects to allow the bubble to break pass through the pores. The resulting flow was similar to the flow of the 1 mm pore size bubble breaker shown in Figure 3.12. The intermittency of gas flow allowed wakes to form that increase liquid mixing, thus enhancing the convective heat transfer (see Figure 3.10). The bubble breakers with larger pore size allowed for continuous flow of the gas phase, thus reducing liquid mixing between the gas phases and reducing the convective heat transfer (see Figure 3.10). At a higher gas flowrate ($Re_{SG}=40$), the buoyancy force of the nozzle-generated gas phase combined with the liquid inertia force was large enough to overcome the surface tension and reduce gas-holdup when the 1mm pore size bubble breaker was used. As seen in Figure 3.14, this causes a flow that is similar to the flow generated by the 2mm pore size bubble breaker. The flow consists of some large coalesced bubbles dispersed among small bubbles. At the same flow condition, the 4mm pore size bubble breaker was able to produce bubble flow; however, the number of small bubbles dispersed amongst the larger bubbles was reduced.

The generation of a dispersed bubbly flow with few liquid breaks between gas phase clusters by the 1mm and 2mm pore size bubble breakers slightly reduced the convective heat transfer coefficient when compared to a flow with no bubble breaker at $Re_{SG}=40$ and $Re_{SL}=1150$. The reduced number of small bubbles in the flow produced by the 4mm bubble breaker reduced the mixing of the liquid at the pipe wall. This effect, combined with the reduced number of liquid breaks between the gas phases caused a large reduction in the heat transfer coefficient as seen in Figure 3.10.

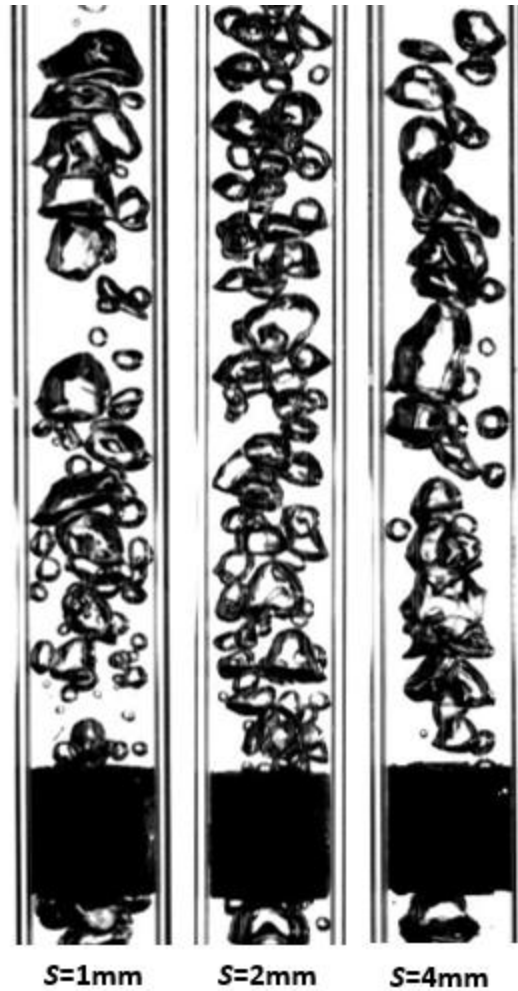


Figure 3.14: High-speed camera images of the flow generated by three bubble breakers at the same flow conditions ($Re_{SG}=40$ and $Re_{SL}=1150$).

At the flow conditions of $Re_{SL}=1150$ and $Re_{SG}=79$, all three bubble breakers were able to increase the heat transfer coefficient when compared to the flow with no bubble breaker. Like the flow condition of $Re_{SL}=380$ and $Re_{SG}=79$, the bubble breakers were able to delay the transition to churn flow. As seen in Figure 3.15, all three bubble breakers were able to produce a dispersed bubbly flow or a slug flow with smaller bubbles dispersed among the slug regions.

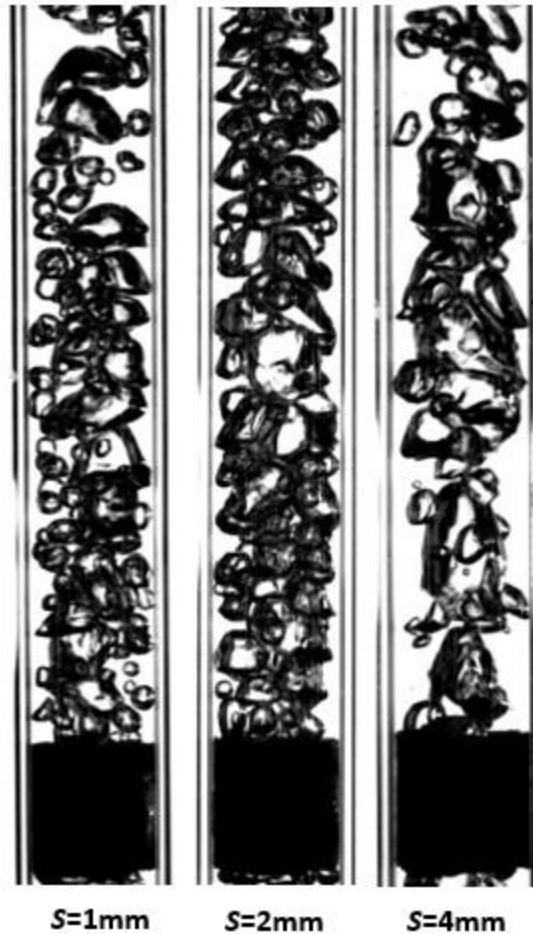


Figure 3.15: High-speed camera images of the flow generated by three bubble breakers at the same flow conditions ($Re_{SG}=79$ and $Re_{SL}=1150$).

Although no liquid breaks are formed in between gas phase clusters in the flows shown in Figure 3.15, the generation of small, dispersed bubbles increases the mixing of the liquid phase at the pipe wall compared to a churn flow generated by a single nozzle. This allowed for the heat transfer enhancement seen in Figure 3.10 for all three bubble breakers at the flow conditions of $Re_{SL}=1150$ and $Re_{SG}=79$.

At the highest liquid flowrate, $Re_{SL}=1900$, the bubble breakers tended to decrease the heat transfer coefficient relative to the flow with no bubble breaker, over the entire range of gas flowrates. At this liquid flowrate, the bubbles or slug regions detached from the single nozzle at a higher frequency when compared to the lower liquid flowrates. The

high liquid flowrate caused the gas regions to stay separated allowing more numerous wakes to form that increases the liquid mixing compared to the flows with lower liquid flowrates. By adding bubble breakers to the pipe at the highest liquid flowrate, bubbly flows or slug flows with small bubbles dispersed between the slug regions were generated. Although the small bubbles can increase the liquid mixing at the pipe surface, in most cases it is not enough to overcome the reduction in the heat transfer coefficient caused by the reduction of wakes behind the gas regions. The 1mm pore size bubble breaker was able to slightly increase the heat transfer coefficient at $Re_{SL}=1900$ and $Re_{SG}=40$ and equal the value relative to the no bubble breaker case at $Re_{SL}=1900$ and $Re_{SG}=16$. For these cases, the added liquid mixing at the pipe wall caused by numerous small bubbles was able to overcome the decrease in liquid caused by the reduction of liquid wakes.

It should be noted that different flow regimes listed in Table 2 at various gas and liquid Reynolds numbers were identified in the region immediately downstream of the bubble breaker or nozzle. It is known that the flow regime of a two-phase flow can change as it travels through a pipe and as coalescence occurs between the gas phases [38, 39]. That is, a flow may start as slug flow in the entrance region but as the gas slugs begin to coalesce, a churn flow may form. Using the local heat transfer coefficient values, the effect of the developing flow regime on the two-phase flow heat transfer can be seen. The local heat transfer coefficients for all three bubble breakers and the flow without a bubble breaker is shown in Figure 3.16 for the flow conditions of $Re_{SL}=1150$ and $Re_{SG}=79$. At this flow condition, flow regime generated in the absence of the bubble breaker was observed to be a churn flow. This flow was transitioned to bubbly flow by the 1mm and 2mm pore size bubble breakers and to slug flow by the 4mm pore size bubble breaker (see Table 2).

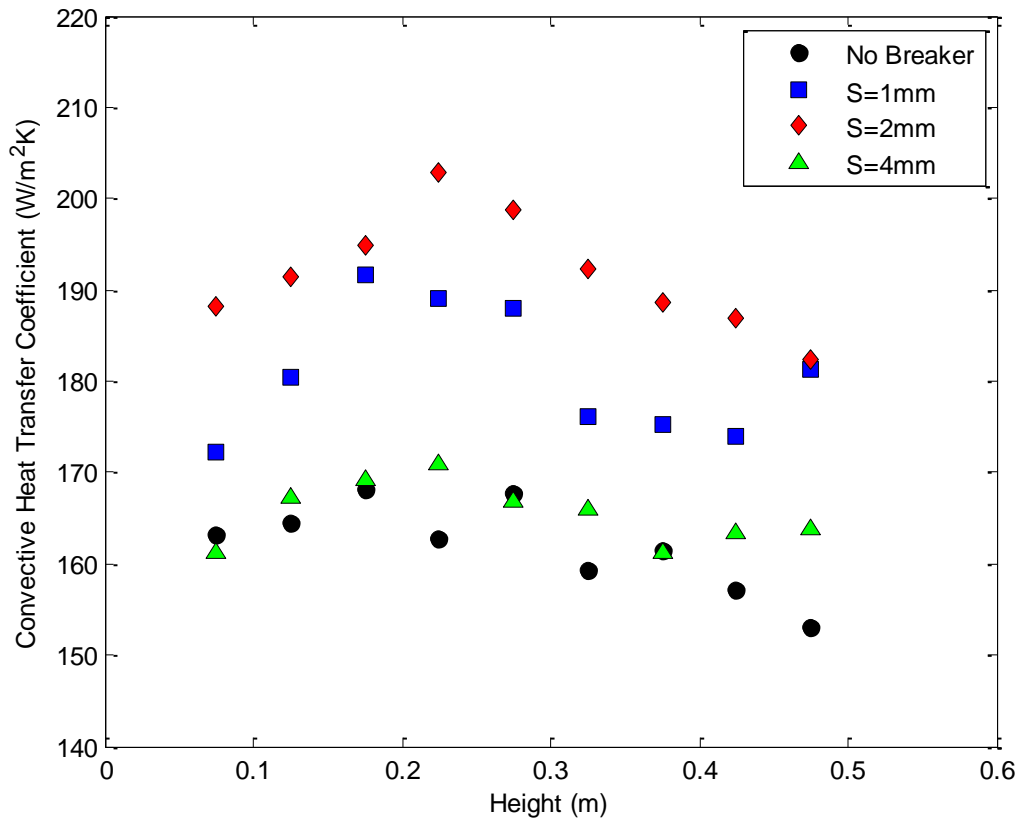


Figure 3.16: Local convective heat transfer coefficients along the length of the pipe for all three bubble breakers and in the absence of a bubble breaker for a two-phase flow with superficial liquid and gas Reynolds numbers of $Re_{SL}=1150$ and $Re_{SG}=79$ respectively.

From Figure 3.16 it can be seen that the bubble breaker geometry has a large effect on the change in the local heat transfer coefficients along the length of the vertical pipe. When no bubble breaker is present, there is little variation in the local heat transfer coefficients indicating that the flow regime observed immediately downstream of the nozzle is consistent throughout the length of the pipe. The 4mm pore size bubble breaker also had little variance in the local heat transfer coefficient. Since the larger pore size generates larger gas regions, less instances of coalescence need to occur before the fully developed flow regime is reached. As the bubble breaker pore size decreases, more variance in the local heat transfer coefficients can be seen. The local heat transfer coefficients for the

1mm pore-size bubble breaker varied by 12%. For this particular flow condition, both the 1mm and 2mm pore size bubble breakers were observed to produce bubble flow in the region just downstream of the bubble breaker. As the flow continued through the pipe, coalescence can occur changing the regime to slug flow and eventually to churn flow. As the flow changes from a dispersed bubbly flow to a slug flow, the heat transfer coefficient may increase as liquid wakes can form behind the gas regions. As coalescence continues and the slug flow transitions to churn flow, the heat transfer coefficient will decrease. This indicates a strong dependency of the convective heat transfer coefficient on the flow regime.

The results from the current study provided further evidence that the complex nature of the two-phase vertical pipe flow makes the prediction of the convective heat transfer coefficient difficult. By adding a bubble breaker downstream of the gas nozzle, the flow structure can be changed, which in turn may influence the rate of heat transfer from the pipe flow to the surroundings. The delay in the transition of the flow regime by the bubble breaker in the region immediately downstream of the bubble breaker and the occurrence of coalescence further downstream, makes the wake formation process throughout the pipe length unsteady and complex. Hence, the development of a generalized correlation to predict heat transfer in the presence of a bubble breaker is a challenging task. Even the use of correlations like the one proposed earlier in the present study or by Vaze and Banerjee [27] that accounts for the change in flow regime could produce greater than expected errors when predicting the heat transfer coefficient or Nusselt number for a flow altered by a bubble breakup device. While the results from the current study do not provide a generalized trend of the influence of a bubble breaker on the heat transfer coefficient due to the flow complexity, they indicate that under certain flow conditions, the bubble breaker could enhance the heat transfer coefficient in two-phase vertical cocurrent flow. This trend is most evident when the bubble breaker suppressed the transition of the flow regime to the churn flow. Further studies are certainly needed to properly characterize the two-phase flow behavior in near and far regions from the bubble breaker, which will further help in the better understanding of the overall heat transfer process.

3.5 Conclusion

An experimental study was conducted to characterize the influence of mesh-type bubble breakers on the convective heat transfer in a two-phase vertical co-flow over a range of superficial liquid and gas Reynolds numbers, $Re_{SL} < 2000$ and $Re_{SG} < 100$, respectively. The local convective heat transfer coefficient for two-phase flow was measured at various locations along the pipe length for flow generated by three mesh-type bubble breakers of pore sizes 1, 2, and 4 mm as well as flow in the absence of a bubble breaker.

The results show that the average convective heat transfer coefficient increased with increasing liquid flowrate and decrease with increasing gas flowrate for all cases (with and without a bubble breaker). Increasing the gas flowrate caused the flow to transition from a bubbly to slug or churn flow regime. This transition reduced the occurrence of wakes in liquid regions following the gas regions, reducing the mixing of the liquid phase and inhibiting the heat transfer. A correlation to predict Nusselt number in vertical two-phase cocurrent flow is proposed.

It is observed that the addition of a mesh-type bubbles breaker downstream of the gas inlet caused the convective heat transfer coefficient to change. The change was dependent on the flow regime and specific flow structure produced by the bubble breaker. In general, it was found that if the bubble breaker was able to produce a flow with a higher occurrence of liquid wakes behind rising gas phases; the bubble breaker was able to enhance the convective heat transfer coefficient relative to the case without a bubble breaker.

3.6 References

- [1] Kantarci, N., Borak, F., and Ulgen, K.O. 2005, "Bubble column reactors." *Process Biochemistry*, **40**(7), pp. 2263-2283.
- [2] Jakobsen, H.A., Lindborg, H., and Dorao, C.A. 2005, "Modeling of Bubble Column Reactors: Progress and Limitations." *Industrial and Engineering Chemistry Research*, **44**(14), pp. 5107-5151.

- [3] Leonard, C., Ferrasse, J., Boutin, O., Lefevre, S., and Viand, A. 2015 “Bubble column reactors for high pressures and high temperatures operation.” *Chemical Engineering Research & Design*, **100**, pp. 391-421.
- [4] Arcuri, E.J., Slaff, G., and Greasham, R. 1986, “Continuous production of thienamycin in immobilized cell systems.” *Biotechnology and Bioengineering*, **28**, pp. 842-849.
- [5] Bordonaro, J.L., and Curtis, W.R. 2000, “Inhibitory role of root hairs on transport within root culture bioreactors.” *Biotechnology and Bioengineering*, **70**, pp. 176-86.
- [6] Son, S.H., Choi, S.M., Lee, Y.H., Choi, K.B., Yun, S.R., and Kim, J.K. 2000, “Largescale growth and taxane production in cell cultures of *Taxus cuspidate* using a novel bioreactor.” *Plant Cell Reports*, **19**(6), pp. 628-633.
- [7] Chang, I.S., Kim, B.H., Lovitt, R.W., and Bang, J.S. 2001, “Effect of partial pressure on cell-recycled continuous co fermentation by *Eubacterium limosium* kist612.” *Process Biochemistry*, **37**, pp. 411-421.
- [8] Shiao, T.I., Ellis, M.H., Dolferus, R., Dennis, E.S., and Doran, P.M. 2002, “Overexpression of alcohol dehydrogenase or pyruvate decarboxylase improves growth of hairy roots at reduced oxygen concentrations.” *Biotechnology and Bioengineering*, **77**, pp. 455-461.
- [9] Nanou, K., Roukas, T., and Papadakis, E. 2012, “Improved production of carotenes from synthetic medium by *Blakeslea trispora* in a bubble column reactor.” *Biochemical Engineering Journal*, **67** pp. 203-207.
- [10] Matheswaran, M., and Moon, I.S. 2009, “Influence parameters in the ozonation of phenol wastewater treatment using bubble column reactor under continuous circulation.” *Journal of Industrial and Engineering Chemistry*, **15**, pp. 287-292.
- [11] Lucas, M.S., Peres, J.A., and Li Puma, G. 2010, “Treatment of winery wastewater by ozone-based advanced oxidation processes (O₃, O₃/UV and O₃/UV/H₂O₂) in a pilot-scale bubble column reactor and process economics.” *Separation and Purification Technology*, **72**(3), pp. 235-241.

- [12] Fernandez-Seara, J., Sieres, J., Rodriguez, C., and Vazquez, M. 2005, "Ammonia-water absorption in vertical tubular absorbers." *International Journal of Thermal Sciences*, **44**(3), pp. 277-288.
- [13] Fernandez-Seara, J., Uhia, F.J. and Sieres, J. 2007, "Analysis of an air cooled ammonia-water vertical tubular absorber." *International Journal of Thermal Sciences*, **46**(1), pp. 93-103.
- [14] Castro, J., Oliet, C., Rodriguez, I., and Oliva, A. 2009, "Comparison of the performance of falling film and bubble absorbers for air-cooled absorption systems." *International Journal of Thermal Sciences*, **48**(7), pp. 1355-1366.
- [15] Jhawar, A.K., and Prakash, A. 2012, "Heat Transfer in a Slurry Bubble Column Reactor: A Critical Overview." *Industrial and Engineering Chemistry Research*, **51** (4), pp. 1464-1473.
- [16] Kantarci, N., Ulgen, K.O., and Borak, F. 2005 "A Study on Hydrodynamics and Heat Transfer in a Bubble Column Reactor with Yeast and Bacterial Cell Suspensions." *Canadian Journal of Chemical Engineering*, **83**(4), pp. 764-773.
- [17] Béliard, P.E., Schweich, D., Clément, P., Gauthier-Maradei, P., and Dromard, N. 2010 "Heat transfer metrology issues in two-phase bubble column reactors." *Canadian Journal of Chemical Engineering*, **88**(4), pp.543-550.
- [18] Aman, J., Ting, D.S.-K., and Henshaw, P. 2014, "Residential solar air conditioning: Energy and exergy analyses of an ammonia-water absorption cooling system." *Applied Thermal Engineering*, **62**, pp. 424-432.
- [19] Butterworth, D., and G. F. Hewitt. *Two-phase Flow and Heat Transfer*. Oxford: Oxford UP, 1977. Print.
- [20] Chu, Y.C., and Jones, B.G. 1980, "Convective Heat Transfer Coefficient Studies in Upward and Downward, Vertical, Two-Phase, Non-Boiling Flows." *American Institute of Chemical Engineers Symposium Series*, **76**, pp. 79-90.
- [21] Sieder, E.N., and Tate, G.E. 1936, "Heat Transfer and Pressure Drop of Liquids in Tubes." *Journal of Industrial and Engineering Chemistry*, **28**(12), pp. 1429-1435.

- [22] Kim, D., Gahjar, A.J., Doughery, R.L., and Ryali, V.K. 1999, "Comparison of Twenty Two-Phase Heat Transfer Correlations with Seven Sets of Experimental Data, Including Flow Pattern and Tube Orientation Effects." *Heat Transfer Engineering*, **20**(10), pp. 15-40.
- [23] Kim, D., Gahjar, A.J., and Doughery, R.L. 2000, "Robust Heat Transfer Correlation for Turbulent Gas-Liquid Flow in Vertical Pipes." *Journal of Thermophysics and Heat Transfer*, **14**(4), pp. 574-578.
- [24] Kaminsky, R.D. 1999, "Estimation of Two-Phase Flow Heat Transfer in Pipes." *Journal of Energy Resources Technology*, **121**(2), pp. 75-80.
- [25] Kim, J.Y. and Ghajar, A.J. 2006, "A general heat transfer correlation for non-boiling gas-liquid flow with different flow patterns in horizontal pipes." *International Journal of Multiphase Flow*, **32**(4), pp. 447-465.
- [26] Kim, D., Ghajar, A.J. 2002, "Heat transfer measurements and correlations for air-water flow of different flow patterns in a horizontal pipe." *Experimental Thermal and Fluid Science*, **25**, pp. 659-676.
- [27] Vaze, M.J., and Banerjee, J. 2011, "A modified heat transfer correlation for two-phase flow." *Heat Mass Transfer*, **47**, pp. 1159-1170.
- [28] Sobrino, C., Acosta-Iborra, A., Santana, D., and de Vega, M. 2009, "Bubble characteristics in a bubbling fluidized bed with a rotating distributor." *International Journal of Multiphase Flow*, **35**(10), pp. 970-976.
- [29] Fadavi, A., Chisti, Y., and Christel, L. 2008, "Bubble size in a forced loop circulation reactor." *Journal of Chemical Technology and Biotechnology*, **83**, pp. 105-108.
- [30] Miyahara, T., Hashimoto, S., Matsunaga, H., and Akagi, Y. 1999, "Bubble splitting by turbulent jet emitted from orifice." *Journal of Chemical Engineering of Japan*, **32**(1), pp. 91-96.
- [31] Miyahara, T., Matsunaga, H., and Akagi, Y. 1999, "Bubble splitting by turbulent jet emitted from nozzle." *Journal of Chemical Engineering of Japan*, **32**(5), pp. 704-707.

- [32] Yang, J.H., Hur, Y.G., Lee, H.T., Yang, J.I., Kim, H.J., Chun, D.H., Park, J.C., Jung, H., and Park, S.B. 2012, "Interaction between partitioning porous plate and rising bubbles in a trayed bubble column." *Chemical Engineering Research and Design*, **90**(10), pp. 1457–1466.
- [33] Prasser, H.M, D. Scholz, D., Zippe, C. 2001, "Bubble size measurement using wire mesh sensors." *Flow Measurement and Instrumentation*, **12**(4), pp. 299-312.
- [34] Gadallah, A.H., and Siddiqui, K. 2015, "Bubble breakup in co-current upward flowing liquid using honeycomb monolith breaker." *Chemical Engineering Science*, **131**, pp, 22-40.
- [35] Incropera, F. P., 2007, *Fundamentals of heat and mass transfer*, Hoboken, NJ: John Wiley.
- [36] Shaoping, Q. 2011, "Co-current flow effects on a rising Taylor bubble." *International Journal of Multiphase Flow*, **37**, pp.888-897.
- [37] Sada, E., Yasunishi, A., Katoh, S., and Nishioka, M. 1978, "Bubble formation in flowing liquid." *The Canadian Journal of Chemical Engineering*, **56**, pp. 669-672.
- [38] Ujang, P.M., Lawrence, C.J., Hale, C.P., and Hewitt, G.F. 2006, "Slug initiation and evolution in two-phase horizontal flow." *International Journal of Multiphase Flow*, **32**, pp. 527-552.
- [39] Waltrich, P.J., Falcone, G., and Barbosa, J.R. 2013, "Axial development of annular, churn and slug flows in a long vertical tube." *International Journal of Multiphase Flow*, **57**, pp. 38-48.

Chapter 4

4 Conclusion

4.1 Overview

This research work comprised of two experimental studies focused on the investigations of the effect of mesh-type bubble breakers with square-shaped pores on two-phase cocurrent flow in vertical pipes. The research was motivated by the need for compact vertical tubular absorbers for use in small-scale heat absorption refrigeration systems. The performance of the absorber units are often limited by the required high rates of heat and mass transfer. It is proposed that mesh-type bubble breakers can be used in vertical tubular absorbers and other bubble column reactors to enhance the heat and mass transfer rates of the system allowing for the development of more compact and efficient units.

The first study investigated the bubble breakers' effect on the flow characteristics of two-phase flow consisting of air and water in a circular glass pipe. The range of the volumetric gas-liquid flow ratio (GLR) used in the experiments was 0.05 to 39.6 to study the effect of bubble breakers on bubbly, slug and churn flow regimes. Various bubble breaker parameters including the length, pore size and position relative to the pipe entrance were varied and their effects on the flow behavior relative to the flow with no bubble breaker present were investigated. A high-speed camera was used to allow flow visualization and characterization. For a bubbly flow regime, it was found that the mean bubble size generated by the bubble breakers increased with increasing GLR and increasing pore size. A Froude number correlation proposed in a previous study to predict the size of bubbles generated by a nozzle was modified and improved to allow for the prediction of the size of bubbles generated by the bubble breakers with varying parameters. The effect of the flow regime transition was also investigated. All bubble breakers were found to increase the GLR at which the flow transitioned from bubbly to slug or churn flow compared to the transition GLRs when no bubble breaker was present. Flow regime maps for all of the bubble breakers were produced from observations of the high-speed camera images. The maps revealed that the GLR at which the flow transitioned from a bubbly to slug or churn flow regime increased with increasing bubble

breaker length and decreasing bubble breaker pore size. A deviation from this trend occurred at higher liquid flow rates with a bubble breaker with a pore size of 1 mm (the smallest pore size tested in this study). Due to a change in the bubble shape caused by the increased liquid inertia, the small pore size was unable to increase the GLR at which the flow transitioned from bubbly to slug.

The second study investigated the effect of bubble breakers with different pore sizes on the convective heat transfer coefficient for two-phase vertical cocurrent flow. A second experimental setup was made to mimic the flow characterization setup; instead of using a glass pipe to allow for flow visualization, a stainless steel tube was used to allow for temperature measurements. Two-phase flow consisting of heated water and air was used in the apparatus over a range of superficial Reynolds numbers, $Re_{SL} < 2000$ and $Re_{SG} < 100$. Local convective heat transfer coefficients along the length of the steel pipe were measured using a combination of measurements from inflow thermocouples for the bulk fluid temperature and a thermal camera for the pipe surface temperature. First, the convective heat transfer coefficient for a two-phase flow without a bubble breaker was measured. It was found that the convective heat transfer coefficient increased with increasing liquid flowrate and decreasing gas flowrate. Observations from the flow characterization study showed the two-phase flow with more frequent liquid breaks between gas phases allowed for increased heat transfer due to mixing of the liquid in the wake of the gas phase. A correlation was proposed to predict the heat transfer coefficient for two-phase flow using the gas and liquid superficial Reynolds numbers. Three bubble breakers with different pore sizes were tested over the same range of gas and liquid flowrates. The general trend of increasing heat transfer rate with increasing liquid flowrate and decreasing gas flowrate remained when the bubble breakers were present, however the heat transfer coefficients for the flows in the presence of bubble breakers varied with respect to the no bubble breaker cases. For most flow conditions, the bubble breakers decreased the heat transfer coefficient due to the generation of more dispersed gas regions with less frequent and smaller liquid wakes behind the gas regions. When the bubble breakers were able to delay the transition to a churn flow regime, the heat transfer rate was enhanced relative to the flow with no bubble breaker as more liquid mixing occurred. The addition of the bubble breakers caused complex flow regimes with flow

behaviour that varied from case to case. A bubbly flow type produced by one bubble breaker may have different flow behaviour when compared to a bubbly flow produced by a different bubble breaker. This makes the prediction of heat transfer coefficients for flows in the presence of a bubble breaker very challenging.

The results of this research can be useful to designers of vertical tubular absorbers. The bubble size correlation proposed in the first study can be used to help predict the absorption rate of the gas phase into the liquid phase. This can allow designers to select the length of pipe needed to ensure the gas phase is fully absorbed into the liquid phase. The flow regime maps can also be used to help estimate the absorption rate for flows that result in slug or churn flow. When selecting a bubble breaker to use in a vertical tubular absorber, the flow regime maps can also be used as a way to optimize the selection. Although it was found that generally, bubble breakers with increased length and decreased pore sizes are more effective at generating flows with high surface area-volume ratios of the gas-liquid interface, both of the features are predicted to increase the pressure loss of the system. The flow regime maps can be used to determine if a desired flow can be achieved with a bubble breaker with a decreased length or increased pore size to reduce the pressure loss. Deviations from the trend of increased effectiveness with decreased pore size shown in the flow regime analysis can be used by absorber designers to avoid the generation of an undesirable flow regime that may decrease the performance of the vertical tubular absorber.

The correlation proposed in the heat transfer investigation to predict the Nusselt number for two-phase flow can be used to predict the heat transfer rate of a vertical tubular absorber that do not use bubble breakers. The investigation into the effect of bubble breakers on two-phase heat transfer did not result in a predictive coefficient. It also revealed that in many cases the use of bubble breakers can decrease the heat transfer rate. When the bubble breakers were able to increase the liquid mixing in the two-phase flow, the heat transfer coefficient increased relative to the flow with no bubble breaker present. The highest increase in heat transfer was found to be when a bubble breaker was able to delay the transition from slug to churn flow. Using this knowledge, along with the flow

regime maps presented in the first study, designers can determine if the bubble breaker will increase or decrease the heat transfer rate.

Bubble breakers are shown to be effective devices for mass transfer enhancement for vertical tubular absorbers by increasing the surface area to volume ratio of the gas-liquid interface in a two-phase flow. For use as heat transfer enhancement devices, bubble breakers were not as effective. In some cases, where the bubble breakers allowed for increased liquid mixing, the bubble breakers were able to increase the heat transfer rate of a two phase flow. However, in many cases the increased gas dispersion generated by the bubble breaker led to decreased heat transfer rates. If the design and performance of a vertical tubular absorber is limited by the mass transfer rate, they can be great tools to allow for more compact and efficient designs. By allowing compact vertical tubular absorbers to be made, small-scale heat absorption refrigeration systems can be developed.

4.2 Contribution

- Improvement on an existing correlation for bubble size prediction in two-phase vertical cocurrent flow in the presence of mesh-type bubble breakers with varying pore size
- Generation of flow regime maps to allow for the prediction of flow regimes of two-phase vertical cocurrent flow in the presence of mesh-type bubble breaker with varying pore size, length and position relative to the gas nozzle
- Proposed a correlation for Nusselt number prediction of two-phase vertical cocurrent flow at low liquid and gas flowrates ($Re_{SL} < 2000$, $Re_{SG} < 100$)
- Analysis of the effect of mesh-type bubble breakers with varying pore size on the heat transfer rate of two-phase vertical cocurrent flow

4.3 Future Recommendations

Future studies are recommended to improve the understanding of the effects of mesh-type bubble breakers on two-phase flow to allow for improved design of vertical tubular absorbers. A limitation of the current study is that only air and water were used as the fluids for the two-phase flows preventing the effect on mass transfer to be studied. Although the current work showed that mesh-type bubble breakers can be used to reduce the bubble size in two-phase flow, which will allow for higher mass transfer rates to occur, air is not absorbed into water and mass transfer measurements could not be made. Tests are needed to investigate bubble breakers' effect on two-phase flows with fluids such as ammonia and water to allow for the measurement of mass transfer rates. Testing two-phase flow with varying fluids will also help to improve the proposed correlations from the current work that are limited to predicting the flow characteristics for air-water two-phase flow only.

For two-phase flow heat transfer, future studies are needed to investigate the effect on flow development. Through analysis of the local heat transfer coefficients along the length of the pipe, it was observed that the bubble breaker pore size had a large effect on the variance of the local heat transfer coefficients. Since the high-speed camera images only captured the entrance region of the flow, proper analysis of the flow behaviour throughout the developing region could not be made. The use of fluids that allow for mass transfer will also have an effect on the two-phase flow development as the volume of the gas regions will decrease preventing some instances of coalescence. Observations of the flow in the entire length of the pipe is needed to gain a better understanding of the heat transfer rates for vertical tubular absorbers.

It is also recommended that the effect of the mesh-type bubble breaker pore shape on two-phase flow be investigated. While the current studies varied the pore size of the bubble breaker, the pore shape always remained a square. Alternative shapes should be tested to allow for more optimization in the design of mesh-type bubble breakers.

Lastly, an investigation on mesh-type bubble breakers' effect on pressure loss in a two-phase flow is recommended. For both the flow characterization study and the heat

transfer study, bubble breakers with smaller pore sizes were found to be more effective for use as mass and heat transfer enhancement devices. Decreasing the bubble breaker pore size increases the total surface area of the bubble breaker which can lead to an increased pressure drop across the bubble breaker. The pressure loss in a system like a heat absorption refrigeration cycle is a critical parameter to be known by the designers to allow for appropriate selection of components like pumps.

Curriculum Vitae

Name: Alan Kalbfleisch

Post-secondary Education and Degrees: Queen's University
Kingston, Ontario, Canada
2009-2014 B.Sc.Eng

The University of Western Ontario
London, Ontario, Canada
2014-2016 M.E.Sc

Honours and Awards: NSERC Undergraduate Student Research Award
2013

Province of Ontario Graduate Scholarship
2015-2016

Related Work Experience Research Assistant
Royal Military College of Canada
2013

Teaching Assistant
The University of Western Ontario
2014-2016

Publications Kalbfleisch, A. and Siddiqui, K. 2015, "The Effect of a Mesh-Type Bubble Breaker on Two Phase Vertical Co-Flow." CANCEM 2015, London, Canada.

Kalbfleisch, A. and Siddiqui, K. 2015, "Bubble Size Reduction Using Mesh Bubble Breakers in Two-Phase Vertical Co-Flow." AJK 2015, Seoul, Korea.